Behaviour of anisotropy and magnetic moment in disordered iron-platinum nanoparticles determined by static and dynamic magnetization measurements

Dissertation
zur Erlangung des Doktorgrades
des Department Physik
der Universität Hamburg

vorgelegt von
Frank Wiekhorst
aus Wilster

Hamburg 2015

Gutachter der Dissertation: Prof. Dr. Kornelius Nielsch
Prof. Dr. Hans Peter Oepen

Gutachter der Disputation: Prof. Dr. Kornelius Nielsch
Prof. Dr. Ralf Röhlsberger

Datum der Disputation: 27.02.2015

Vorsitzender des Prüfungsausschusses: Prof. Dr. Michael Alexander Rübhausen

Vorsitzende des Promotionsausschusses: Prof. Dr. Daniela Pfannkuche

Dekan des Department Physik: Prof. Dr. Heinrich Graener

Abstract

This work presents the structural and magnetic characterization of platinum-rich $\mathrm{Fe}_x\mathrm{Pt}_{1-x}$ nanoparticles, which were prepared following a wet-chemical organometalic nanoparticle synthesis by thermal decomposition in the presence of stabilizing oleic acid. The behaviour of anisotropy and magnetic moment of $\mathrm{Fe}_x\mathrm{Pt}_{1-x}$ nanoparticles is investigated combining (quasi-)static magnetic magnetization measurements with dynamic susceptibility measurements at gigahertz frequencies.

The structural characterization by TEM and XRD yield the presence of chemically disordered spherical $\mathrm{Fe}_x\mathrm{Pt}_{1-x}$ nanocrystals with a mean core diameter d_p of about 4 nm and having a rather narrow log-normal size distribution. A platinum-rich composition of the nanoparticles with x in the range $0.1 \ldots 0.25$ is indicated by the lattice constant a_0. The composition of the particles could be verified by relating the Curie temperature determined from ZFC magnetization measurements to the composition. By annealing of the as synthesized particles at temperatures up to 800 K, no chemical ordering could be achieved.

A log-normal distribution with mean anisotropy barrier energies E_A about 300 K to 600 K is revealed from temperature dependent ZFC- and AC magnetization measurements, from which an effective anisotropy constants K_eff of about 10^5 J/m^3 follows. High field ($H = 10$ kOe) magnetization measurements $M(T)$ of $\mathrm{Fe}_x\mathrm{Pt}_{1-x}$ nanoparticles reveal Bloch type temperature dependent magnetic moments $\mu_\mathrm{p}(T)$ with much smaller Bloch coefficients than observed in bulk systems. Mean particle moments $\mu_\mathrm{p}(T = 0\text{ K})$ in the range $500\,\mu_\mathrm{B}$ to $1000\,\mu_\mathrm{B}$ extrapolated to $T = 0$ K have been determined from magnetization isotherms $M(H)$ incorporating the Bloch type temperature dependence.

The isotropic g-factor determined by magnetic resonance spectroscopy (MRS) is linearly dependent on the composition x of the $\mathrm{Fe}_x\mathrm{Pt}_{1-x}$ nanoparticles. The dominating contribution to the g-factor is given by the spin moment. To describe the strong shift of the resonance field H_res towards zero field and the marked increase of the line-width ΔH_pp observed in the MRS-spectra at lower temperatures, different models based on the phenomenological Landau-Lifshitz and Gilbert line shape models have been implemented and analysed.

The mean anisotropy field H_A could be determined from the shift of the resonance field H_res using an analytical expression describing $H_\mathrm{res}(H_\mathrm{A})$ obtained from energy minimization of the free energy including field and anisotropy energy. A more convincing description describing the full measured line shapes could be achieved introducing a complex damping into the basic Landau-Lifshitz model.

magnetic nanoparticles, iron-platinum aloys, magnetic resonance spectroscopy, magnetization dynamics, magnetocrystalline anisotropy, line-shape analysis

Zusammenfassung

Im Schwerpunkt dieser Arbeit stand die Untersuchung der statischen und dynamischen magnetischen Eigenschaften nass-chemisch hergestellter $\mathrm{Fe}_x\mathrm{Pt}_{1-x}$ Nanopartikel mit organischer Umhüllung. Das magnetische Verhalten von Anisotropie und magnetischem Moment in $\mathrm{Fe}_x\mathrm{Pt}_{1-x}$ -Nanopartikeln wurde anhand von (quasi-)statischen Magnetisierungsmessungen und Messungen der transversalen dynamischen magnetischen Suszeptibilität im Bereich von Mikrowellenfrequenzen ermittelt.

Die strukturelle Charakterisierung mittels TEM und XRD ergab das Vorliegen von chemisch ungeordneten sphärischen $\mathrm{Fe}_x\mathrm{Pt}_{1-x}$ Nanokristallen mit einem mittleren Durchmesser von 4 nm und schmaler Log-Normal Größenverteilung. Die Gitterkonstanten a_0 deuten auf eine Platin-reiche Zusammensetzung der $\mathrm{Fe}_x\mathrm{Pt}_{1-x}$ Nanopartikel mit x im Bereich $0.1 \ldots 0.25$ hin. Diese wurde über die Curie Temperatur, die aus magnetischen ZFC-Messungen an den vorhandenen $\mathrm{Fe}_x\mathrm{Pt}_{1-x}$ Nanopartikeln abgeleitet wurde, präzise ermittelt. Mit dem Heizen der Proben bis hoch zu Temperaturen von 800 K konnte keine chemisches Ordnen der $\mathrm{Fe}_x\mathrm{Pt}_{1-x}$ Partikel erzielt werden.

Aus ZFC- und AC-Messungen ergab sich eine Log-Normal Verteilung der Anisotropieenergiebarrieren mit mittleren Energien von 300 K bis zu 600 K, aus der eine effektive Anisotropiekonstante $K_{\mathrm{eff}} \approx 10^5$ J/m^3 folgt für die 4 nm $\mathrm{Fe}_x\mathrm{Pt}_{1-x}$ Nanopartikel. Hochfeld-Magnetisierungsmessungen $M(T, H = 10\mathrm{kOe})$ der $\mathrm{Fe}_x\mathrm{Pt}_{1-x}$ Nanopartikel zeigen Blochsches Temperaturverhalten der magnetischen Momente, allerdings mit deutlich geringeren Blochkoefizienten als in bulk Systemen beobachtet wird. Aus den Magnetisierungsisothermen wurden mittlere Partikelmomente $\mu_{\mathrm{p}}(T = 0)$ im Bereich 500 μ_{B} bis 1000 μ_{B} ermittelt.

Mit der Magnetischer Resonanzspektroskopie bei Raumtemperatur wurde der isotrope g-Faktor bestimmt, der linear mit der Komposition x der $\mathrm{Fe}_x\mathrm{Pt}_{1-x}$ Nanopartikel abnimmt. Dabei trägt das Spinmoment den größten Anteil am g-Faktor. Die Temperatur-abhängigen Resonanzspektren zeigen mit abnehmender Mess-Temperatur eine starke Abnahme der Resonanzfeldstärke H_{res} bei gleichzeitig deutlicher Zunahme der Linienbreite ΔH_{pp}. Um dieses Verhalten zu beschreiben, wurden die phänomelogischen Landau-Lifshitz und Gilbert Modelle zur Beschreibung der Linienform erweitert und analysiert. Dabei konnte ein analytischer Ausdruck aus einer Energieminimierung unter Berücksichtigung von Feld- und Anisotropiebeiträgen gefunden werde, um das mittlere Anisotropiefeld H_{A} aus der Verschiebung von H_{res} zu berechnen. Darüber hinaus wurde ein Landau-Lifshitz Ansatz mit komplexer Dämpfung vorgestellt, der eine überzeugende Beschreibung der Linienform der $\mathrm{Fe}_x\mathrm{Pt}_{1-x}$ Nanopartikel erlaubt.

Magnetische Nanopartikel, Eisen-Platin Verbindungen, Magnetische Resonanz Spektroskopie, Magnetisierungsdynamik, magnetokristalline Anisotropie, Linienformanalyse

Contents

Chapter 1

Introduction

Since the 1980s nanotechnology has come to be one of the most exciting and propelling interdisciplinary research areas [1]. Originally intended to build machines on the scale of molecules, the meaning of nanotechnology shifted more and more in the following years to the development of systems smaller than 100 nanometers with novel physical, chemical or biological properties [2]. Out of these systems, magnetic nanoparticles emerged from 2000 onwards as a class with continuously growing research effort, see Fig. 1.1.

Currently, magnetic nanoparticles are of intense interest for a variety of applications, not only for the general miniaturization of devices, but because their physical properties may dramatically deviate from their bulk counterparts, which can be ascribed to two characteristic features of magnetic nanoparticles, namely single domain ferromagnetism and superparamagnetism. For this, not only the nanometre size is responsible, but especially the magnetic anisotropy of the material constituting the magnetic nanoparticles.

Therefore, much research has been related to binary transition-metal systems like FePt, CoPt and FePd with their huge magnetocrystalline anisotropy energy, which is in the order of 10^6 J/m^3. While first research was focused on the magnetism of these systems in thin-films, it was with the presentation of a novel wet-chemical preparation route by Sun *et. al.* [4] in 2000, that especially magnetic nanoparticles of FePt became promising candidates for ultrahigh-density magnetic recording media. Even today this interest is still going on to improve the understanding of the complex magnetism in $\mathrm{Fe}_x\mathrm{Pt}_{1-x}$ magnetic nanoparticles, as is documented by the number of publications coping with

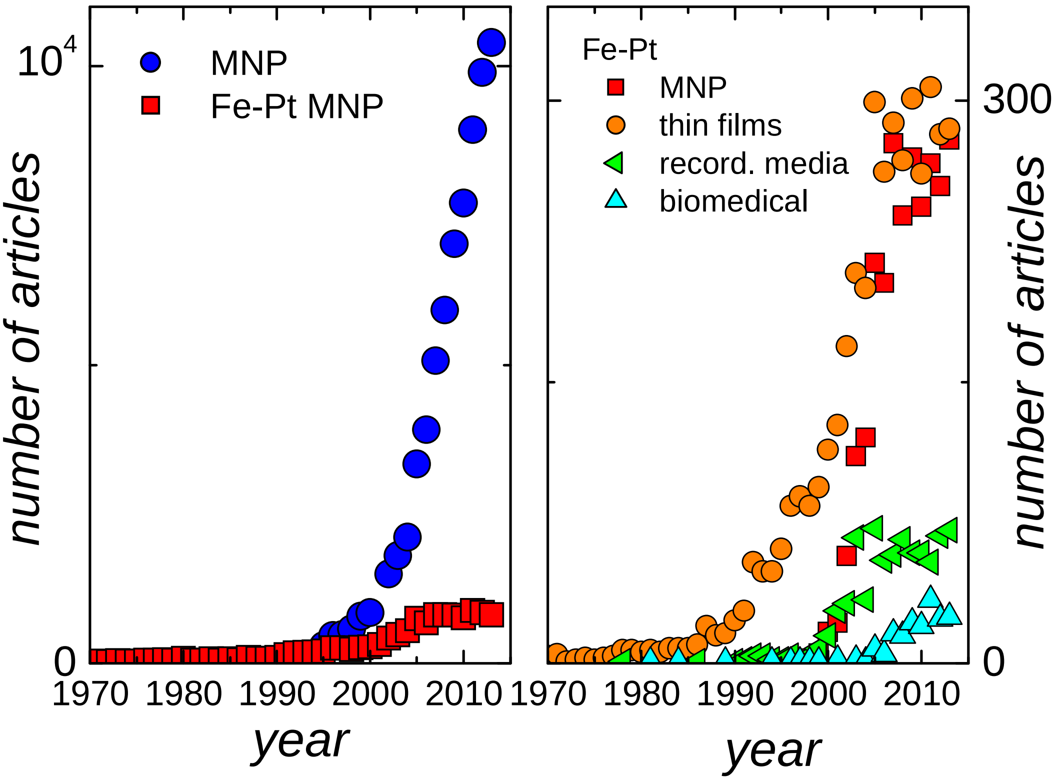

Figure 1.1: Yearly number of citations containing (left) combinations of the keywords *magnetic nanoparticles* and *iron-platinum* and (right) *iron-platinum* with either *magnetic nanoparticles*, *thin films*, *recording media*, or *biomedical applications*. The counts were determined by Web of Science online queries [3] using the keywords as search items.

this topic, as displayed in Fig. 1.1.

Fe_xPt_{1-x} can be prepared over the continuous range of solid solutions, and both stoichiometric and non-stoichiometric alloys with various degrees of chemical order exist. Of the three ordered stoichiometric phases – Fe_3Pt, FePt, $FePt_3$ – the equiatomic FePt shows the largest anisotropy energy with values up to $6 \cdot 10^6$ J/m^3. This extremely large value is almost two orders of magnitude larger than the one found for the disordered fcc phase, $1 \cdot 10^5$ J/m^3 [5].

The confinement of the geometrical extension entails a complicated interaction of the magnetic and electronic structures in Fe_xPt_{1-x} nanoparticles with tremendous consequences for the magnetic properties compared to those measured and calculated in bulk systems. Of particular interest is the interplay between effective magnetic anisotropy generated by the crystal structure and shape of the nanoparticles and magnetic moment μ_{p} related to the internal magnetic structure of the particle. But not only internal structure and parameters are of importance. The nanoparticle physics depends strongly on external parameters such as temperature and external magnetic field. Furthermore, the time scale of an experiment has a great impact on the observed behaviour of magnetic nanoparticles. On the other hand, the appropriate choice of these external parameters allows one to isolate an effect of interest without being disturbed by other properties. So is the influence of magnetic anisotropy in nanoparticles strongly reduced by thermal fluctuations at high temperatures.

This work presents a comprehensive study of the magnetic behaviour of chemically disordered platinum-rich$\mathrm{Fe}_x\mathrm{Pt}_{1-x}$ nanoparticles. The aim is to combine magnetic susceptibility measurements, which reflect an integral (quasi-) static magnetic fingerprint with microwave resonance spectroscopy probing the dynamic magnetic properties of the local magnetic and electronic environment of $\mathrm{Fe}_x\mathrm{Pt}_{1-x}$ nanoparticles. To this end the influence of anisotropy and magnetic moment on the static and dynamic properties in $\mathrm{Fe}_x\mathrm{Pt}_{1-x}$ nano-particles is determined.

The structure of this work is organized as follows. In chapter 2, the theoretical groundwork comprising the magnetism of nanoparticles and fundamentals of magnetic resonance spectroscopy are presented. In chapter 3, the structural and magnetic properties of the binary transition-metal compound Fe-Pt together with experimental details of the utilized measurement techniques are collected. Chapter 4 first presents the results of the structural characterization of the $\mathrm{Fe}_x\mathrm{Pt}_{1-x}$ nanoparticles. Then, the quasi-static magnetic behaviour of $\mathrm{Fe}_x\mathrm{Pt}_{1-x}$ nanoparticles is analysed, especially the distribution of anisotropy energy barriers and the determination of the mean magnetic moment μ_{p}. In chapter 5 the dynamics of the magnetization at microwave frequencies is investigated, for which a description of the observed temperature dependent magnetic resonance spectra is presented. Summary and conclusions are given in chapter 6.

Chapter 2

Fundamentals

In this chapter, some fundamentals of the magnetism of magnetic nanoparticles will be presented. First, the main interactions and energies responsible for the magnetic behaviour observed in interaction-free magnetic nanoparticles are introduced. After this, the general magnetic properties of magnetic nanoparticles merged under the notion superparamagnetism are described. Hereby, (quasi-)static and dynamic aspects of the magnetism are considered separately. Furthermore, the basic theory of magnetic resonance absorption of magnetic nanoparticles is depicted since it is the main experimental technique used in this work. Finally, several structural and magnetic properties of the binary iron-platinum system are described for bulk and nanoparticular $\mathrm{Fe}_x\mathrm{Pt}_{1-x}$.

2.1 Magnetism of magnetic nanoparticles

2.1.1 Magnetic interactions and energies

The magnetism in a magnetic nanoparticle is a collective phenomenon of the electronic spins; there are different ways for the magnetic moments to communicate with each other. Some relevant mechanisms for possible interactions are summarized in this section.

Exchange interaction In a magnetic nanoparticle, the exchange interaction is responsible for the coupling of typically 10^2 to 10^4 atomic magnetic moments to form one giant magnetic moment μ_p. The exchange energy of two electrons with spin operators $\hat{S}_1$ and $\hat{S}_2$ is given by

$$E_{\mathrm{ex}} = -2J_{12}\hat{S}_1 \cdot \hat{S}_2, \tag{2.1}$$

where J_{12} is the exchange integral, which for $J_{12} > 0$ leads to parallel alignment of the spins, e. g. to ferromagnetic ordering. Since J_{12} is vanishing except for neighbouring electrons, the exchange interaction is very short ranged. However, its magnitude in the order of 10^{-2} (≈ 100 K) eV leads to magnetic long range ordering of magnetic moments below a critical temperature. In a continuum approximation of the crystal the exchange energy can be expressed as

$$E_{\mathrm{ex}} = A \int \mathrm{d}V(\vec{\nabla} \cdot \vec{\mu})^2, \tag{2.2}$$

with the exchange constant $A = 2JS^2p/a$, where J is the exchange integral (now with contributions from mainly next-neighbour moments), a the distance between next neighbours and p the number of sites in the unit cell.

Spin-orbit interaction The spin-orbit interaction is the origin of anisotropy in magnetic nanoparticles. Generally, electrons possess both an orbital magnetic moment m_l (caused by their angular momentum due to the precession around the nucleus) and an spin magnetic moment m_s (due to their intrinsic spin momentum). The spin-orbit interaction denotes the coupling of the spin magnetic moment with their own orbital magnetic moment, and can be written for hydrogen-like atoms with spin $\hbar\vec{S}$ and angular moment $\hbar\vec{L}$ as

$$E_{\mathrm{SO}} = \beta \frac{\langle \vec{L} \cdot \vec{S} \rangle}{n^3 l(l+1/2)(l+1)}, \tag{2.3}$$

where n and l denote the principle and angular quantum numbers. The prefactor $\beta = Z^4 e^2 \hbar^2/(4\pi\epsilon_0 a_0^3)$ contains the atomic number Z and the Bohr radius a_0. The crystal structure symmetry is mediated by the spin-orbit interaction to the spin system, and is one origin of magnetocrystalline anisotropy. This anisotropy energy is larger for crystal lattices of low symmetry and smaller in lattices of high symmetry, and depends on the state of chemical order. Hence, the two orders of magnitude higher anisotropy constant $K \approx 10^7$ J/m^3 appearing in the ordered $L1_0$ FePt phase when compared to the unordered phase (10^5 J/m^3) [6] are due to tetragonal distortion and atomic arrangement.

Furthermore, the spin-orbit coupling is accountable for intrinsic magnetic damping. For atoms in a crystal lattice, the spin-orbit interaction energy is of the order 10^{-3} eV ($\approx$ 10 K).

Magnetic dipolar interaction Two magnetic nanoparticles with moment $\vec{\mu}_1$ and $\vec{\mu}_2$ at a distance $\vec{r}$ from each other give rise to the magnetic dipolar interaction energy

$$E_{\mathrm{dip}} = \frac{\mu_0}{4\pi r^3}\left[\vec{\mu}_1 \cdot \vec{\mu}_2 - \frac{3}{r^2}(\vec{\mu}_1 \cdot \vec{r})(\vec{\mu}_2 \cdot \vec{r})\right]. \tag{2.4}$$

While the dipolar interaction in the order of 10^{-6} eV ($\approx$ 12 mK) is not sufficient to cause long range order of magnetic moments, it is accountable for demagnetizing field effects and spin waves in the long wave length regime. Furthermore, at low temperatures it may cause particle-particle interactions (spin glass behaviour) when a coupling of moments between individual nanoparticles is energetically favourable compared to the thermal energy $\mathrm{k_B}T$.

Magnetocrystalline and surface anisotropy energy As mentioned before, the anisotropy is caused by the spin-orbit interaction, which projects the crystal symmetry of the nanoparticles onto the magnetic spin and orients the electron spin moments along an easy axis. In bulk materials, magnetocrystalline and magnetostatic energies are the main source of anisotropy, whereas in magnetic nanoparticles particles additional contributions from shape and surface anisotropy may become relevant.

Due to the magnetocrystalline anisotropy energy, a nanoparticle will, in the absence of an external magnetic field, align its magnetic moment with one of the easy axes, an energetically favourable direction usually related to a principal axes of the crystal lattice of the particle.

The simplest form of anisotropy is uniaxial anisotropy, where a nanoparticle has only one easy axis

$$E_{\mathrm{uni}} = K_1 V \sin^2\theta + K_2 V \sin^4\theta + \cdots \tag{2.5}$$

where K_1 and K_2 are the anisotropy constants, V is the particle volume, and θ is the angle between magnetization and easy axis direction. The anisotropy constants possess a temperature dependency [7], but at temperatures much lower than the Curie temperature of the material they are considered as temperature independent constants. Usually, K_2 and all higher order coefficients are negligible compared to K_1, so often only the first term with $K_1 = K$ is included in calculations. According to Eq. 2.5 a positive value of K implies an easy axis.

Thus, to flip the magnetic moment direction from one easy direction, $\theta = 0$, to the other, $\theta = \pi$, an energy barrier KV at $\theta = \pi/2$ has to be surmounted.

In a crystal structure with cubic symmetry the anisotropy is given by

$$E_{\text{cub}} = K_1 V(\alpha_1^2\alpha_2^2 + \alpha_2^2\alpha_3^2 + \alpha_3^2\alpha_1^2) + K_2 V \alpha_1^2\alpha_2^2\alpha_3^2 + \cdots \tag{2.6}$$

Here, the direction cosines are defined as $\alpha_1 = \sin\theta\cos\phi$, $\alpha_1 = \sin\theta\sin\phi$, $\alpha_3 = \cos\theta$, with θ being the angle between magnetization and z-direction and ϕ the azimuthal angle.

Especially in confined nanoparticles systems, the (distorted) lattice structure and symmetry at surfaces and interfaces may lead via the spin-orbit coupling to substantial anisotropy contributions in addition to the magnetocrystalline anisotropy. It is often convenient to combine surface, interface, and magnetocrystalline anisotropies into one effective anisotropy K_{eff}. Furthermore, it turned out that for many magnetic nanoparticle systems – even with cubic crystal structure – the (simple) uniaxial anisotropy Eq. 2.5 is sufficient to describe magnetocrystalline, surface, or shape anisotropy effects observed in experiment.

Shape anisotropy Shape anisotropy occurs for magnetic nanoparticles which are not perfectly spherical, so that the demagnetizing field will not be equal for all directions creating one or more easy directions. The demagnetizing energy is formally given by

$$E_{\text{dem}} = -\frac{1}{2}\int \vec{\mu}\cdot\vec{B}_{\text{dem}} = \frac{1}{2}\widehat{N}\,\vec{m}(\vec{B}). \tag{2.7}$$

Here, the integral is very complex to calculate even for simple homogeneously magnetized sample geometries, where $\vec{B}_{\text{dem}}$ is the internal demagnetizing field caused by uncompensated magnetic charges due to the nanoparticle surface. Only for homogeneously magnetized ellipsoids Eq. 2.7 simplifies as given in the second term with the dimensionless demagnetizing tensor $\widehat{N}$ [8]. With the magnetic moment pointing along one of the principal axes it can be diagonalized with $N_x + N_y + N_z = 1$.

Zeeman energy The Zeeman energy results from the interaction of a magnetic nanoparticle with an external magnetic field. It depends on the orientation of magnetic moment $\vec{\mu}$ with the magnetic field $\vec{B} = \mu_0 \vec{H}$,

$$E_{\mathrm{mag}} = -(\vec{\mu} \cdot \vec{B}), \tag{2.8}$$

favouring a parallel alignment between moment and field direction.

2.1.2 The effective field within a magnetic nanoparticle

From the functional derivative of the total energy E_{tot} the effective magnetic field $\vec{B}_{\mathrm{eff}}$ is found to be

$$\vec{B}_{\mathrm{eff}} = -M_{\mathrm{S}} \frac{\partial E_{\mathrm{tot}}}{\partial \vec{\mu}}. \tag{2.9}$$

For non-interacting nanoparticles, the individual contributions to E_{tot} are given by the Zeeman energy E_{mag}, magnetocrystalline and shape anisotropy energy E_{ani}, demagnetization energy E_{dem} and exchange energy E_{ex}

$$E_{\mathrm{tot}} = E_{\mathrm{mag}} + E_{\mathrm{ani}} + E_{\mathrm{dem}} + E_{\mathrm{ex}}. \tag{2.10}$$

2.1.3 Superparamagnetism of magnetic nanoparticles

Phenomenology of superparamagnetism

The definition of superparamagnetism is based on two characteristic observations. First, in thermodynamical equilibrium or at infinite time scales, the magnetization curve shows no hysteresis, no coercivity, and no remanence. Second, the magnetization curves $M(H, T = \mathrm{const})$ of an isotropic (without any or with negligible anisotropy) magnetic nanoparticle ensemble taken at different temperatures T superimpose when plotted against H/T (see isotropic superparamagnetism in sec 2.1.5). Often, a correction for a temperature variation of the spontaneous magnetization or the magnetic moment of the magnetic nanoparticle is required.

There are various models for the magnetization reversal of single-domain particles. The most prominent is the model of coherent rotation of magnetization as developed by Stoner and Wohlfarth [9]. This model, which, strictly speaking, is valid only at $T = 0$ K, assumes non-interacting particles with uniaxial anisotropy, in which the magnetic moments are parallel and rotate in unison. In another model, valid at any finite temperatures also, the moments can overcome the anisotropy energy barrier by thermal activation, thus leading to a switching of the particle magnetization. Thus, the observed net magnetization of an nanoparticle ensemble shows a time dependent relaxation. This relaxation process was first proposed by Néel [10], and further developed by Brown [11; 12].

The time scales on which a magnetic nanoparticle system is disturbed and on which its response is observed constitute the main difference between dynamic and static magnetization phenomena. When applying a quasi static field, the magnetic moments appear to be always in equilibrium since the dynamics of the moments are in a much faster time scale (typically nanoseconds to milliseconds). When applying an alternating magnetic field at a frequency close to the resonance frequency of the nanoparticle system, the magnetic moments are resonantly disturbed from their equilibrium orientation.

Magnetic moment μ_p and saturation magnetization M_S of single domain nanoparticles

Below a critical diameter d_c, the formation of magnetic domains separated by domain walls which is observed in bulk ferromagnets becomes unfavourable, so the magnetic nanoparticle is said to be in a single domain state. This diameter is approximately given by [13]

$$d_c \approx \frac{72\sqrt{AK_u}}{\mu_0 M_\mathrm{S}^2}, \tag{2.11}$$

with the exchange constant A, the uniaxial anisotropy constant K_u and the saturation magnetization M_S. For $L1_0$-FePt particles, critical diameters d_c ranging from 50 nm up to 600 nm were reported [14; 15]. Depending on the size and material, magnetic single domain nanoparticles consist of $10^2 - 10^5$ individual magnetic moments coupled by the exchange interaction to act as one giant moment μ_p. The a particle with diameter d has a saturation magnetization $M_\mathrm{S} = \mu_\mathrm{p}/V = 6\mu_\mathrm{p}/(\pi d^3)$.

The magnetization behaviour of single domain magnetic nanoparticles in thermodynamic equilibrium is identical to that of an atomic paramagnetic material, except that much larger magnetic moments, and thus larger susceptibilities, are involved. These similarities coined the term *superparamagnetism* for the thermal equilibrium behaviour.

Temperature dependent magnetic nanoparticle moment $\mu_\mathrm{p}(T)$ and Curie temperature T_C

At temperatures well below T_C, the temperature dependence of the magnetic moment μ_p is ascribed to spin-wave fluctuations (propagating collective excitations of the coupling between the spin moments within one nanoparticle) as first described by Bloch [16], who found that

$$\mu_\mathrm{p}(T) = \mu_\mathrm{p}(0)(1 - BT_\mathrm{C}^{\beta}), \tag{2.12}$$

where B is the Bloch constant and β the Bloch exponent, which has the value $\beta = 3/2$ for bulk systems, but is found to decrease with particle size [17]. Furthermore, from mean-field theory, the temperature dependent magnetic moment is given by

$$\mu_\mathrm{p}(T) = \mu_\mathrm{p}(0)(1 - T/T_\mathrm{C})^{\alpha}). \tag{2.13}$$

Here, $\alpha = 0.5$ is taken for $T < T_\mathrm{C}$, which can only approximate the temperature dependence of the magnetic moment, in particular for T/$T_\mathrm{C} \to 0$. An interesting function capable of describing $\mu_\mathrm{p}(T)$ over the full temperature range was proposed to be [18]

$$\mu_\mathrm{p}(T) = \mu_\mathrm{p}(0)\left[1 - \gamma\,(T/T_\mathrm{C})^{3/2} - (1-\gamma)\,(T/T_\mathrm{C})^{5/2}\right]^{1/3}, \tag{2.14}$$

where γ denotes the shape factor and is determined by the intensity of the exchange interaction. For T/$T_\mathrm{C} \to 0$ Eq. 2.14 merges into the Bloch law Eq. 2.12.

For nanoparticles a reduction of T_C with decreasing diameter has been reported for ferromagnetic Fe, Co and Ni nanofilms [19; 20] and $\mathrm{Fe_3O_4}$ nanoparticles [21].

2.1.4 Influence of the anisotropy on the magnetic behaviour of magnetic nanoparticles

Blocking temperature

The (effective) anisotropy of a magnetic nanoparticle generates an energy barrier $\Delta E = K_{\mathrm{eff}} V$ (Eq.2.5 with $\theta = \pi/2$) which has to be overcome by thermal energy $\mathrm{k_B} T$ to change the magnetization direction and thus to lead to fluctuations which are of Neel-Arrhenius type[1]

$$\tau = \tau_0 \exp\left(\frac{\Delta E}{\mathrm{k_B} T}\right) = \tau_0 \exp\left(\frac{K_{\mathrm{eff}} V}{\mathrm{k_B} T}\right), \tag{2.15}$$

with the characteristic time τ_0 – the attempt time – in the range 10^{-12} s to 10^{-9} s [10; 11]. For τ_0 an analytical expression can be given that is valid in the absence of a magnetic field and in the high barrier limit [12]

$$\tau_0 = \frac{1+\alpha^2}{\alpha\gamma} \sqrt{\frac{\pi \mathrm{k_B} T M_{\mathrm{S}}^2}{4 K_{\mathrm{eff}}^3 V}} = \frac{1+\alpha^2}{\alpha\gamma} \sqrt{\frac{\pi \mathrm{k_B} T \mu_{\mathrm{p}}^2}{4 E_{\mathrm{A}}^3}}. \tag{2.16}$$

Here, α denotes the dimensionless Gilbert damping constant and γ the electron gyromagnetic ratio (see section 2.2). The relation $M_{\mathrm{S}} = \mu_{\mathrm{p}}/V$ has been used to introduce $E_{\mathrm{A}} = K_{\mathrm{eff}} V$ in the second term. Though a variation of τ_0 with temperature and particle size is present in Eq. 2.16, it usually is taken to be constant.

For a given energy barrier and temperature, the time of measurement t_{m} determines the observed magnetic behaviour of a magnetic nanoparticle ensemble. For $t_{\mathrm{m}} > \tau$, the individual magnetic moments of a particle will flip several times during the measurement, so that the measured magnetization will average to zero without any magnetic field applied. Once a magnetic field is present the nanoparticle ensemble will approach a reversible magnetization described by the Langevin function (see Eq.2.34 below). Due to the large number of magnetic moments coupled within one particle, this behaviour is called superparamagnetism.

If $t_{\mathrm{m}} < \tau$, the individual moments will not flip during the measurement, so that the measured magnetization will be the same as in the beginning of

---

[1] Since in this work only dried samples have been investigated, effects of Brownian relaxation, e.g. fluctuations of the measured magnetic moments due to rotation of complete particle, are not considered here.

the measurement. As the particle moments are in a blocked state, hysteresis effects with coercivity and remanence become visible.

Therefore, the behaviour of magnetic nanoparticles (superparamagnetic or blocked) always depends on the measurement time t_m. The transition from superparamagnetic to blocked state occurs at the so-called blocking temperature T_b, which logarithmically depends on the measurement time

$$T_\mathrm{b} = \frac{K_\mathrm{eff} V}{\mathrm{k_B} \ln\left(\frac{t_\mathrm{m}}{\tau_0}\right)} \approx \frac{K_\mathrm{eff} V}{25\mathrm{k_B}}, \tag{2.17}$$

for magnetic measurements with typical $t_\mathrm{m} \approx 100$ s duration.

Zero-field cooled and field cooled susceptibility

By zero-field cooled (ZFC) and field cooled (FC) magnetization curves, the transition from blocked to superparamagnetic behaviour of a magnetic nanoparticle ensemble according to their moment distribution and anisotropy can be visualized. Typically, a ZFC magnetization curve is obtained by first cooling in zero field from a high (room) temperature, where all particles show superparamagnetic behaviour, down to a low temperature. Then the magnetization is measured in a small applied magnetic field with stepwise increasing temperatures up to room temperature. Subsequently, the FC magnetization curve is obtained by measuring the magnetization in the same small applied magnetic field, now stepwise decreasing temperatures again. It is assumed that each magnetization measurement is taken after a pause time $t_\mathrm{m} \approx 100$ s to settle the temperature and to acquire the magnetization.

Following the pioneering work of Wohlfarth [22], the initial susceptibility for a single nanoparticle in the superparamagnetic state is given as $\chi_\mathrm{sp} = \mu_0 M_\mathrm{S}^2 V/(3\mathrm{k_B}T)$ and in the blocked state $\chi_\mathrm{bl} = \mu_0 M_\mathrm{S}^2/(3K_\mathrm{eff})$. The transition occurs at the so-called blocking temperature $T_\mathrm{b}(E_\mathrm{b})$, which depends on the energy barrier $E_\mathrm{b} = K_\mathrm{eff}V = K_\mathrm{eff}\,\mu_\mathrm{p}/M_\mathrm{S}$ given by the effective anisotropy K_eff and moment μ_p of the particle. Furthermore, it depends on the time scale of the measurement so that $T_B(E_\mathrm{b}) = E_\mathrm{b}/(\mathrm{k_B}\ln(t_\mathrm{m}/\tau_0)) = K_\mathrm{eff}\,\mu_\mathrm{p}/(M_\mathrm{S}\mathrm{k_B}\ln(t_\mathrm{m}/\tau_0))$.

Here, the small contribution of blocked particles, $(T_\mathrm{b} > T)$, to χ_ZFC is ignored, while for superparamgnetic particles, $(T_\mathrm{b} < T)$, $T\chi_\mathrm{ZFC}$ follows a Curie law. At a given temperature T, only particles with $T_\mathrm{b} \sim T$ significantly contribute to $\mathrm{d}(T\chi_\mathrm{ZFC})$. Thus, from a ZFC magnetization curve the distribution of energy barriers $f(E_A)$ can be obtained

$$f(E_A) = \mathrm{k_B} \ln(t_\mathrm{m}/\tau_0) \frac{\mathrm{d}(T\chi_\mathrm{ZFC})}{\mathrm{d}T}, \tag{2.18}$$

where the observation time t_m is in the order of 100 s.

The ZFC and FC magnetization curves of a random-oriented, non-interacting nanoparticle system may be calculated numerically, as proposed by Hansen and Morup [23]

$$M_{ZFC}(T) = \frac{\mu_0 H M_\mathrm{S}^2}{3K_\mathrm{eff}} \left[\frac{E_\mathrm{bm}}{\mathrm{k_B}} \int_0^{T/T_\mathrm{bm}} \frac{y}{T} f(y) \mathrm{d}y + \int_{T/T_\mathrm{bm}}^{\infty} f(y) \mathrm{d}y \right]; \tag{2.19}$$

and

$$M_{FC}(T) = \frac{\mu_0 H M_\mathrm{S}^2}{3K_\mathrm{eff}} \frac{E_\mathrm{bm}}{\mathrm{k_B}} \left[\int_0^{T/T_\mathrm{bm}} \frac{y}{T} f(y) \mathrm{d}y + \int_{T/T_\mathrm{bm}}^{\infty} \frac{y f(y)}{T_\mathrm{b}(y E_\mathrm{bm})} \mathrm{d}y \right]. \tag{2.20}$$

They use the reduced energy variable $y \equiv E_\mathrm{b}/E_\mathrm{bm}$, where E_bm is the median energy barrier and introduce the volume weighted log-normal distribution of energy barriers $f(y) = (2\pi)^{-1/2}(\sigma y)^{-1} \exp[-\ln^2 y/(2\sigma^2)]$ with median at one. Here, $T_\mathrm{b}(E_\mathrm{b}) \equiv E_\mathrm{b}/(\mathrm{k_B} \ln(t_\mathrm{m}/\tau_0))$, so that $y \equiv T_\mathrm{b}/T_\mathrm{bm}$. Different other approaches exist [24; 25], a collection of which may be found in the appendix.

AC-susceptibility

Measuring the temperature dependence of the complex AC susceptibility is another common procedure to probe the dynamic answer of magnetic nanoparticles to a small magnetic field harmonically varying in time.

Arrhenius analysis of AC-data Based on the classical Debye theory, the real and imaginary parts of the complex dynamic susceptibility at a frequency ω are given by

$$\chi'(\omega) = \chi_0 \frac{1}{1 + (\omega\tau)^2}; \tag{2.21}$$

$$\chi''(\omega) = \chi_0 \frac{\omega\tau}{1 + (\omega\tau)^2}. \tag{2.22}$$

where χ_0 is the linear static zero-field susceptibility (in the limit $\omega \to 0$) of N_p particles with moment μ_p. The relaxation time τ is given by the Arrhenius-Néel relaxation Eq. 2.15. In Eq. 2.22 the loss component $\chi''(\omega)$

has a maximum at $\omega\tau = 1$. By means of Eq. 2.15, this can be written $\omega = \tau^{-1} = \tau_0^{-1}\exp(-E_\mathrm{A}/(\mathrm{k_B}T_\omega)$ and cast into the form [26]

$$\log(\omega) = -\frac{E_\mathrm{A}}{\mathrm{k_B}\ln(10)}\frac{1}{T_\omega} - \log(\tau_0), \tag{2.23}$$

where T_ω is the temperature at the maximum of $\chi''(\omega)$. According to Eq. 2.23, plotting the (logarithm of the) excitation frequencies ω as a function of the inverse maximum temperature T_ω of $\chi''(\omega)$ allows one to extract the energy barrier E_A and the pre-factor τ_0. Generally, an ensemble of magnetic nanoparticles exhibits a size distribution, while by Eq. 2.23 only one mean energy barrier is obtained in the case of a narrow size distribution. A more sophisticated analysis resolving the complete energy barrier distribution is presented in the following paragraph.

Distribution of anisotropy energy barriers

For non-interacting nanoparticles with random distribution of easy axes the temperature dependent complex AC-susceptibility $\chi(\omega, T)$ may be written as [27; 28]

$$\chi(\omega, T) = \frac{C}{T}\int_0^\infty \mathrm{d}\epsilon P(\epsilon)\epsilon\left\{\frac{R'/R}{1 + i\omega\tau(\epsilon)} + \frac{1 - R'/R}{1 + i\omega\tau_\perp}\right\}, \tag{2.24}$$

where C is the Curie constant, and $\omega = 2\pi f = 2\pi/t_\mathrm{m}$ is the frequency of the AC-field. The complex susceptibility is divided into longitudinal and transversal contributions. The longitudinal relaxation time contant $\tau(\epsilon)$ in the first term in the brackets of Eq. 2.24 describes just as in Eq. 2.22 the thermally activated coherent flipping of the magnetic moment between two energy minima, for which the Néel-Arrhenius ansatz Eq. 2.15 with the reduced anisotropy energy $\epsilon = E_A/E_{A,m}$ and the abbreviation $\sigma = E_A/(k_BT)$ is utilized

$$\tau(\epsilon) = \tau_0 \exp\left(\frac{\epsilon E_{A,m}}{k_BT}\right) \equiv \tau_0 \exp(\sigma). \tag{2.25}$$

The transversal relaxation time constant $\tau_\perp$ in the second term of Eq. 2.24 reflects the dynamics of the magnetic moment within one of the energy minima. The transversal susceptibility is probed by magnetic resonance spectroscopy, see Sec. 2.2.2. The ratio σ between anisotropy energy and thermal energy at a given temperature determines the relative weights of both mechanisms and is given by the statistical factors

$$\begin{aligned} R(\sigma) &= \int_0^1 \mathrm{d}z \exp(\sigma z^2); & (2.26)\\ R'(\sigma) &= \frac{\mathrm{d}R}{\mathrm{d}\sigma} = \int_0^1 \mathrm{d}z\ z^2 \exp(\sigma z^2). & (2.27)\end{aligned}$$

Furthermore, a log-normal distribution $P(\epsilon)$ of the (reduced) anisotropy energy is included.

By decomposing Eq. (2.24) into real and imaginary parts, individual expressions for the dissipation and absorption are obtained

$$\begin{aligned} \chi'(\omega,T) &= \mathrm{Re}\,[\chi(\omega,T)] = \\ &= \frac{C}{T}\int_0^\infty \mathrm{d}\epsilon P(\epsilon)\epsilon\left\{\frac{R'/R}{1+(\omega\tau(\epsilon))^2}+\frac{1-R'/R}{1+(\omega\tau_\perp)^2}\right\}; & (2.28)\\ \chi''(\omega,T) &= \mathrm{Im}\,[\chi(\omega,T)] = \\ &= \frac{C}{T}\int_0^\infty \mathrm{d}\epsilon P(\epsilon)\epsilon\left\{\frac{\omega\tau(\epsilon)R'/R}{1+(\omega\tau(\epsilon))^2}+\frac{\omega\tau_\perp 1-R'/R}{1+(\omega\tau_\perp)^2}\right\}. & (2.29)\end{aligned}$$

Generally, the transversal relaxation time is assumed to be much shorter than the longitudinal $\tau_\perp \approx \tau_0 \ll \tau(\epsilon)$. Thus, for low measurement frequencies ω the second term in Eq. 2.24 can be neglected. Furthermore, $\tau(\epsilon)$ varies rapidly as compared to $\epsilon P(\epsilon)$, so that under the integral of the imaginary part $\chi''(\omega)$ the substitution can be employed [29]

$$\frac{\omega\tau(\epsilon)}{1+(\omega\tau(\epsilon))^2} \approx \frac{\pi}{2}k_B T\cdot\delta(\epsilon-\epsilon_\omega). \tag{2.30}$$

Here, $\epsilon_\omega \equiv T/T_\omega = k_B T(-\ln(\omega\tau_0))/E_{A,m}$ is the largest relative energy barrier that can be surmounted by thermally activation within the given observation time $2\pi/\omega$. With this the integration of Eq. 2.29 is carried out to yield

$$\chi''(\omega,T) = \frac{\pi}{2}\frac{k_B C(T)}{E_B}\frac{R'(\epsilon_\omega)}{R(\epsilon_\omega)}P(\epsilon_\omega)\epsilon_\omega. \tag{2.31}$$

This means in the absorption χ'' the dynamic contribution $P(\epsilon_\omega)d\epsilon$ of the anisotropy distribution is picked up. Except for $P(\epsilon_\omega)$, the other factors in Eq. 2.31 vary little as compared to the distribution function. This includes the ratio $R'(\epsilon_\omega)/R(\epsilon_\omega)$, which for $E_{A,m}/(\mathrm{k_B}T_\omega) \approx -\ln(\omega\tau_0) \gg 1$ is always close to one

$$\frac{R'}{R} = 1 - \frac{k_B T_\omega}{E_{A,m}}. \tag{2.32}$$

Therefore, in a plot of $\chi''(\omega, T)$ (measured for individual excitation frequencies ω) as a function of the renormalized temperature $-T\ln(\omega\tau_0) = \epsilon_\omega E_{A,m}/k_B$ all data should collapse on a single curve, directly providing the distribution of anisotropy energy barriers

$$P(\epsilon_\omega) = \chi''(\omega, -T\ln(\omega\tau_0)). \tag{2.33}$$

2.1.5 Influence of the external magnetic field on the magnetic behaviour of magnetic nanoparticles

Isotropic superparamagnetism in a magnetic field: Langevin-function

Well above the blocking temperature T_b, the magnetization of the nanoparticles is reversible within the time of measurement, thus no hysteresis effects are observed. Neglecting the influence of any anisotropy the resulting orientation of a magnetic moment $\vec{\mu}$ of a nanoparticle in an external applied magnetic field $\vec{H}$ is determined by the ratio of Zeeman energy (see Eq. 2.8) tending to align the moments with the field direction and thermal energy $\mathrm{k_B}T$ aiming the equipartition of moment orientations at temperature T. The resulting magnetization of an ensemble of magnetic nanoparticles follows Boltzmann statistics and is expressed by the Langevin function $\mathcal{L}(x) = \coth(x) - 1/x$. Its argument is $x \equiv \mu\,\mu_0 H/(\mathrm{k_B}T)$. Thus, the field dependent magnetization curve of an ensemble of N_p nanoparticles per kilogram measured at a constant temperature T, also known as magnetization isotherm, is given by

$$M(H) = N_\mathrm{p}\,\mu\left(\coth\left(\frac{\mu\,\mu_0 H}{\mathrm{k_B}T}\right) - \frac{\mathrm{k_B}T}{\mu\,\mu_0 H}\right). \tag{2.34}$$

Real nanoparticle systems are never found to consist of identical particles, but show variations in sizes and structure leading to a distribution of magnetic moments μ. This is accounted for by incorporating a log-normal distribution $P(\mu)$ of the moments μ in Eq. (2.34)

$$P(\mu) = \frac{1}{\sqrt{2\pi}\sigma\mu}\exp\left(-\frac{(\ln\mu - \ln\tilde{\mu})^2}{2\sigma^2}\right), \tag{2.35}$$

with two characteristic parameters, the median $\tilde{\mu}$ and the width σ of the distribution[2]. Thus we obtain

$$M(H,T) = N_{\mathrm{p}} \int_0^\infty \mu\, P(\mu) \left(\coth\left(\frac{\mu\, \mu_0 H}{\mathrm{k_B} T} \right) - \frac{\mathrm{k_B} T}{\mu\, \mu_0 H} \right) \mathrm{d}\mu + \chi_{\mathrm{bgd}} H, \qquad (2.36)$$

where a linear susceptibility χ_{bgd} has been introduced to account for any dia- and paramagnetic contributions mainly from the inorganic shell of the nanoparticle. Equation 2.36 provides a common basis for the description and analysis of measured magnetization curves.

For $\mu\, \mu_0 H \gg \mathrm{k_B} T$ the Langevin function becomes 1 and the saturation value is approached:

$$M_S = N_{\mathrm{p}} \bar{\mu}, \qquad (2.37)$$

where the mean particle moment $\bar{\mu} = \tilde{\mu} \exp(\sigma^2/2)$ is related by the width σ to the median $\tilde{\mu}$ of the log-normal distribution, Eq. 2.35. In the linear regime, for $\mu\, \mu_0 H \ll \mathrm{k_B} T$ the Langevin function $\mathcal{L}$ is approximated by $x/3$ so that

$$M(H,T) = \frac{N_{\mathrm{p}} \mu_0 H}{3 \mathrm{k_B} T} \int_0^\infty \mu^2\, P(\mu) \mathrm{d}\mu = \frac{N_{\mathrm{p}} \tilde{\mu}^2 \mu_0 H}{3 \mathrm{k_B} T} \exp(\sigma^2). \qquad (2.38)$$

2.1.6 Behaviour of magnetic nanoparticles in the presence of anisotropy and external magnetic field

Anisotropic superparamagnetism

Upon decreasing the temperature, but still keeping it above T_B, the influence of the anisotropy on the magnetization curve $M(H)$ can no longer be disregarded. In order to facilitate numerics, non-interacting magnetic nanoparticles with an uniaxial anisotropy E_{A} and randomly distributed easy axes are assumed. Thus, the energy of a magnetic nanoparticle with a moment $\vec{\mu}$ in a magnetic field $\vec{H}$ taking an uniaxial anisotropy of the particle into account is given by

$$\begin{aligned} E(\theta, \alpha, \phi, v) &= -KV \cos^2\theta - \mu(H_{\|} \cos\theta + H_{\perp} \sin\theta \cos\phi) \\ &= -Kv\tilde{V} \cos^2\theta - \mu H(\cos\alpha \cos\theta + \sin\alpha \sin\theta \cos\phi). (2.39) \end{aligned}$$

Here, θ denotes the angle between easy axis and magnetic moment direction, as defined in the spherical coordinate system displayed in Fig. 2.1. The volume V

---

[2] The median of the log-normal distribution is not to be confused with the mean diameter, see appendix (B) for more details on this distribution B

of the particle is expressed relative to the median volume $v = V/\tilde{V}$. In Eq. 2.39, the field has been divided into a component parallel and perpendicular with respect to the easy axis direction. The field $\vec{H}$ is assumed to lie in the xz-plane where $\cos\phi = 1$.

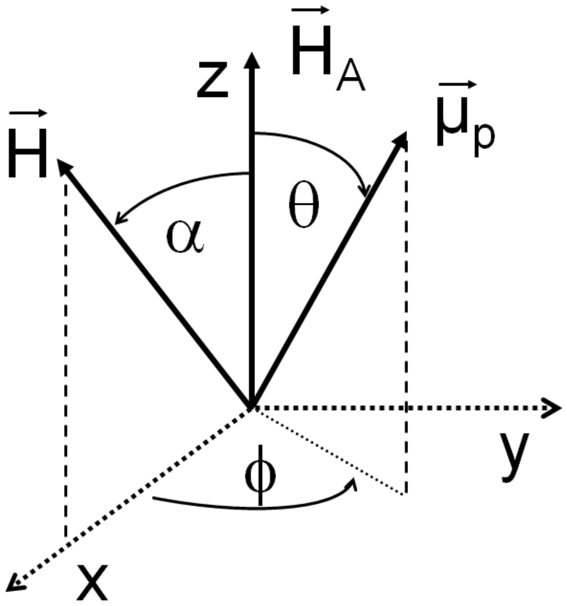

Figure 2.1: Definitions of the angles used in the calculation of the magnetization in the anisotropic superparamagnetic regime.

Following Garcia-Palacios [29], the partition function $\mathcal{Z}$ of a particle at an individual angle α between external field and easy axis can be defined as

$$\mathcal{Z}(H, T, \alpha, v) \;=\; \frac{1}{2\pi}\int_0^\pi \mathrm{d}\theta \sin\theta \int_0^{2\pi} \mathrm{d}\phi \exp\left(-\frac{E(\alpha, \theta, \phi, v)}{\mathrm{k_B}T}\right), \quad (2.40)$$

while the associated free energy is given by $\mathcal{F} = -\mathrm{k_B}T \ln \mathcal{Z}$. At equilibrium, the probability distribution of magnetic moment orientations is given by the Boltzmann distribution $P(\alpha, \cos\theta, \phi, v) = \mathcal{Z}^{-1} \exp(-E(\alpha, \theta, \phi, v)/(\mathrm{k_B}T))$.

From the partition function, the (equilibrium) magnetization $M = N_\mathrm{p}\langle\vec{\mu}\cdot\vec{H}\rangle_{eq}$ of an ensemble of N_p nanoparticles can be derived by the logarithmic derivative

$$M = \frac{N_p \mu^2}{\mathrm{k_B}T} \frac{\partial \ln \mathcal{Z}}{\partial H}. \quad (2.41)$$

The integration over ϕ can be performed by introducing the modified Bessel-function of order zero $I_0(y) = \pi^{-1}\int_0^\pi \mathrm{d}t \exp(y \cos t)$ [30] to obtain

$$\mathcal{Z}(H, T, \alpha) \;=\; \int_0^\pi \mathrm{d}\theta \sin\theta \exp\left(v(\frac{K\tilde{V}\cos^2\theta + \tilde{\mu}H\cos\alpha\cos\theta)}{\mathrm{k_B}T}\right)$$

$$\times I_0 \left(\frac{v\tilde{\mu} H \sin\alpha \sin\theta}{\mathrm{k_B} T} \right). \tag{2.42}$$

Substituting the variable $z = \cos\theta$ and thus $\mathrm{d}z = \sin\theta\,\mathrm{d}\theta$, the integration over θ may be written more compactly as

$$\begin{aligned} \mathcal{Z}(H, T, \alpha, v) &= \int_{-1}^{1} \mathrm{d}z \exp\left(\frac{vK\tilde{V}z^2 + v\tilde{\mu}H\cos\alpha\ z}{\mathrm{k_B}T} \right) \\ &\quad \times I_0 \left(\frac{v\tilde{\mu}H \sin\alpha \sqrt{1 - z^2}}{\mathrm{k_B}T} \right). \end{aligned} \tag{2.43}$$

Then, the integration over α is executed

$$M(H, T, v) = \frac{1}{2} N_\mathrm{p} \mathrm{k_B} T \int_0^\pi \mathrm{d}\alpha \sin\alpha \frac{\partial \ln \mathcal{Z}(H, T, \alpha, v)}{\partial H}, \tag{2.44}$$

where the integration over α for symmetry reasons can be reduced to the interval $[0, \pi]$, leading to the factor 1/2.

Finally, a log-normal distribution for the particle volumes is used to calculate the magnetization of an ensemble of magnetic nanoparticles

$$M(H, T) = \int_0^\infty \mathrm{d}v P(v) M(H, T, v). \tag{2.45}$$

In Fig. 2.1.6, magnetization curves $M(H, T)$ (for the fixed volume $v = 1$) according to Eq. 2.44 for individual angles α are displayed together with the averaged curve (red curve) and the Langevin function without anisotropy (blue). This shows that the influence of the anisotropy leads to a decrease of magnetization in the mid-field range compared with the isotropic Langevin curve. Furthermore, with increasing magnetic field the anisotropic magnetization Eq. 2.44 approaches more and more the Langevin curve and finally its saturation value.

The limit $E_A = 0$: Isotropic superparamagnetism In case of vanishing anisotropy $E_A = 0$, which can be assumed if $E_A \ll \mathrm{k_B}T$, the partition function $\mathcal{Z}$ does not depend on α, so $\alpha = 0$ can be chosen (meaning that $H_\| = H$ and $H_\perp = 0$), so that the Bessel function becomes $I_0(0) = 1$. Using $\int_{-1}^{1} \mathrm{d}z\ \exp(az) = a^{-1}(\exp(a) - \exp(-a)) = a^{-1}\, 2\sinh a$ the partition function Eq. 2.43 becomes $\mathcal{Z} = \int_{-1}^{1} \mathrm{d}z\ \exp\left(z\frac{\mu H}{\mathrm{k_B}T}\right) = \frac{2\mathrm{k_B}T}{\mu H} \sinh\left(\frac{\mu H}{\mathrm{k_B}T}\right)$. Therefore, for an ensemble of N_p particles the Langevin expression Eq. 2.34 is reproduced

$$M(H, T) = N_p \mathrm{k_B} T \frac{\partial \ln \mathcal{Z}}{\partial H} = N_p \mu \left(\coth\left(\frac{\mu H}{\mathrm{k_B}T} \right) - \frac{k_B T}{\mu H} \right). \tag{2.46}$$

Thus, the isotropic Langevin magnetization is obtained from the partition function in the limiting case of vanishing anisotropy.

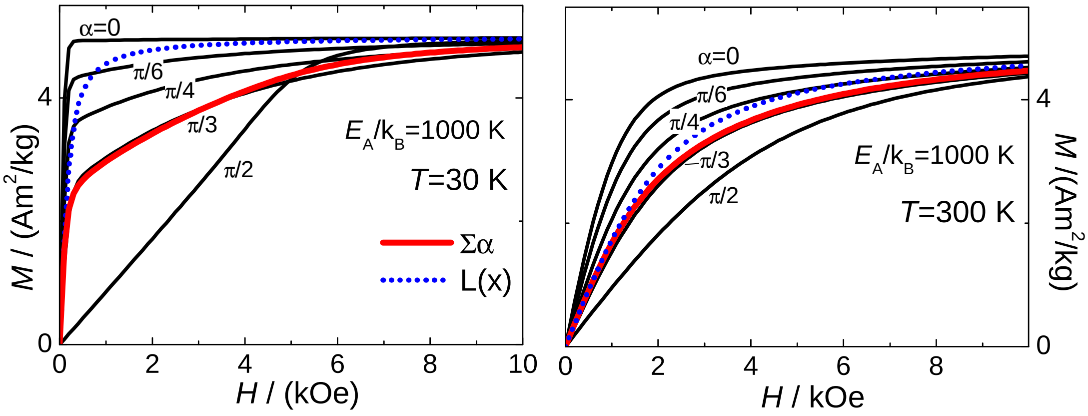

Figure 2.2: Magnetization curves according to Eq. 2.43 for individual values of the angle α and fixed $v = 1$ (no size distribution) for $T = 30$ K (left panel) and $T = 300$ K (right panel) assuming an anisotropy energy of $K\tilde{V}/\mathrm{k_B} = 1000$ K. Additionally, $M(H,T)$ after integration over α (straight red line) and isotropic Langevin-magnetization (dotted blue line) are plotted.

2.2 Magnetic resonance spectroscopy (MRS)

Magnetic resonance spectroscopy (MRS) is a powerful spectroscopic technique for probing the magnetization of magnetic materials. It is similar to nuclear magnetic resonance except that the sample magnetization resulting from the magnetic moments of unpaired electrons are probed ,rather than the atomic nuclear magnetic moments. Due to the much lower electron mass, the resonance frequency is shifted towards microwave frequencies (gigahertz). Paramagnetic resonance and ferromagnetic resonance are the most prominent resonance absorption techniques classifying the type of magnetic material under investigation.

Paramagnetic resonance An atom or molecule with unpaired electrons possesses a non-vanishing magnetic dipole moment μ, which is generated by the angular momentum $\vec{L}$ and spin $\vec{S}$

$$\vec{\mu} = -\mu_{\mathrm{B}}(g_S\vec{S} + g_L\vec{L})/\hbar, \tag{2.47}$$

where $g_S \approx 2.0023$ and $g_L = 1$ are the Landé-factors of spin and orbital moment of an electron. In a homogeneous magnetic field $\vec{H}_{\mathrm{res}}$, the field will exert a torque $\vec{\tau} = \vec{\mu} \times \vec{H}_{\mathrm{res}}$ on the moment, leading to a precession of $\vec{\mu}$ about the field direction at the Larmor frequency ω

$$\omega = \frac{g\mu_{\mathrm{B}} H_{\mathrm{res}}}{\hbar} = \gamma H_{\mathrm{res}}, \tag{2.48}$$

with the gyromagnetic ratio $\gamma \equiv g\mu_{\mathrm{B}}/\hbar$ containing the effective g-factor, which reflects the coupling of angular with spin moment. Quantum-mechanically, this is equivalent to the effect of splitting $\Delta E = g\mu_{\mathrm{B}} B_{\mathrm{res}}$ of the two degenerated energy levels of the unpaired electron moment $\pm\frac{1}{2}m_S$ by the static magnetic field (Zeeman effect).

In a basic setup for an MRS-experiment a microwave resonant cavity and an electromagnet are utilized. The resonant cavity has a main eigenresonance at a microwave frequency ω_{cav}. A microwave detector is placed at the end of the cavity. A magnetic sample positioned in the cavity placed between the poles of an electromagnet providing a homogeneous quasi-static magnetic field. This field is slowly swept while the resonant absorption intensity of the microwaves is detected. When the Larmor precession frequency of the magnetic moment and the resonant cavity (eigenresonance) frequency are the same $\omega = \omega_{\mathrm{cav}}$, absorption of microwave energy P by the sample takes place, which is indicated by a decrease in the intensity at the detector.

Ferromagnetic resonance Unlike in paramagnetic materials, strong exchange interactions between individual spins are present in ferromagnet. This results in a coherent precession of the spins, and thus of the total particle moment μ, if a magnetic field is applied. The coupling of the (spin) moments due to exchange interaction, as well as magnetocrystalline and shape anisotropies caused by spin-orbit interaction within a nanoparticle, involve large internal magnetic fields which can be probed by MRS of a magnetic material.

2.2.1 Phenomenological equations of motion

The microscopic origin of the damping is not completely understood in detail and constitues an active area of research. Possible relaxation mechanisms are divided into intrinsic (spin-orbit interaction) and extrinsic (magnon-magnon scattering due to crystal imperfections) processes, but are hard to separate by experiment. Hence, these are commonly taken into account by one effective damping constant α_{eff}.

In an MRS experiment, the precession of a particle moment $\vec{\mu_p}$ in an effective magnetic field is described by the classical equation of motion [31; 32]

$$\frac{\mathrm{d}}{\mathrm{d}t}\vec{\mu_p} = \gamma \vec{B}_{\text{eff}} \times \vec{\mu}_p + \vec{R}, \tag{2.49}$$

which represents an undamped precession with the left hand side describing the temporal development of the magnetic moment driven by the torque acting on the moment on the right hand side. To account for energy losses due to interactions of the moments with each other (magnons) and the environment (phonons) a damping term $\vec{R}$ is added to the right hand side of Eq. 2.49.

One approach for this damping is the Landau-Lifshitz damping given by [33]

$$\vec{R}_L = \frac{\lambda_L}{M_S}\left(\vec{B}_{\text{eff}} \times \vec{\mu}_p\right) \times \frac{\vec{\mu}_p}{\mu_p}, \tag{2.50}$$

with damping frequency $\lambda_L = 1/\tau$, which corresponds to an inverse relaxation time. But this damping approach leads to the non-physical behaviour that very large damping causes very fast precession of the moment. This problem was circumvented by introducing a viscous damping term [34]

$$\vec{R}_G = \alpha \frac{\mathrm{d}\vec{\mu}_p}{\mathrm{d}t} \times \frac{\vec{\mu}_p}{\mu_p}, \tag{2.51}$$

with $\alpha = \lambda/(\gamma M_S)$ being a dimensionless damping parameter. This approach is referred to as the Landau-Lifshitz-Gilbert (LLG) equation.

2.2.2 Dynamic susceptibility in MRS

The magnetic resonance absorption signal is proportional to the imaginary part of the transverse[3] dynamic susceptibility χ. A coordinate system is chosen where the static magnetic field component of $\vec{H}$ is along the z-axis, the microwave magnetic field $\vec{h} = (h_x, h_y)$ lies in the perpendicular plane. Using the Polder tensor method [35] the phenomenological equations may be solved. The magnetization response $\vec{m} = (m_x, m_y)$ to the microwave field $\vec{h}$ may be expressed as

$$\vec{m} = \begin{pmatrix} \chi & -i\kappa \\ i\kappa & \chi \end{pmatrix} \vec{h}, \tag{2.52}$$

---

[3] See the second term of Eq. 2.24. In the following the index $\perp$ for the transversal susceptibility $\chi_\perp$ will be omitted.

where χ and κ describe the response to the x- and y- components of $\vec{h}$. For a circularly polarized microwave field $h^{\pm} = h_0 e^{\pm i\omega t}$, the dynamic susceptibility is given by $\chi_{\pm} = \chi \mp \kappa = \chi'_{\pm} - i\chi''_{\pm}$. The ± signs stand for the two polarization directions and are usually referred to as resonant (or Larmor) and non-resonant (anti-Larmor) polarization. For a linear polarized microwave field $h = h_0 \cos\omega t$ applied along the x-axis, the complex susceptibility is

$$\chi = \chi' - i\chi'' = \frac{1}{2}\left(\chi_+ + \chi_-\right) = \frac{1}{2}\left[\chi'_+ + \chi'_- - i(\chi''_+ + \chi''_-)\right], \tag{2.53}$$

so the absorption for linear and circular polarization are related by $\chi''(H) = \frac{1}{2}\left[\chi''_+(H) + \chi''_-(H)\right]$.

2.2.3 Landau-Lifshitz and Gilbert line shape

Associated with the two phenomenlogical equations of motions Eq.2.49 - 2.51 are two individual complex MRS-susceptibilities. So, for Landau-Lifshitz damping $\vec{R} = \vec{R}_L$ the two normal, circularly polarized modes for N_p independent nanoparticles per gram take the form

$$\chi^L_{\pm}(H) = N_p\mu_p\gamma\frac{1 \mp i\alpha}{\gamma H(1 \mp i\alpha) \mp \omega}. \tag{2.54}$$

Accordingly, for Gilbert damping $\vec{R} = \vec{R}_G$ the normal susceptibility follows as

$$\chi^G_{\pm}(H) = N_p\mu_p\gamma\frac{1}{\gamma H \mp \omega(1 + i\alpha_G)}. \tag{2.55}$$

Using Eq. 2.53 the experimental, transverse susceptibility $\chi_{xx} = \frac{1}{2}(\chi_+ + \chi_-)$ takes the form for Landau-Lifshitz damping

$$\chi^L_{xx}(H) = N_p\mu_p\gamma\frac{\gamma H(1+\alpha^2) - i\alpha\omega}{(\gamma H)^2(1+\alpha^2) - \omega^2 - 2i\alpha\omega\gamma H}, \tag{2.56}$$

and

$$\chi^G_{xx}(H) = N_p\mu_p\gamma\frac{\gamma H - i\alpha\omega}{(\gamma H)^2 - \omega^2(1+\alpha^2) - 2i\alpha\omega\gamma H}, \tag{2.57}$$

for Gilbert damping[4]

---

[4] Alternatively, introducing the resonance field $H_\omega = \omega/\gamma$ eq. 2.56 and eq. 2.57 can be written more compactly

$$\chi^L_{xx}(H) = N_p\mu_p\frac{H(1+\alpha^2) - i\alpha H_\omega}{H^2(1+\alpha^2) - H^2_\omega - 2i\alpha H H_\omega}, \tag{2.58}$$

and

$$\chi^G_{xx}(H) = N_p\mu_p\frac{\gamma H - i\alpha H_\omega}{H^2 - H^2_\omega(1+\alpha^2) - 2i\alpha H H_\omega}. \tag{2.59}$$

Taking the imaginary part the experimentally observed Landau-Lifshitz line shape becomes

$$\begin{aligned} \chi''^{L}(H) &= \mathrm{Im}[\chi^{L}(H)] \\ &= N_p\mu_p\omega\gamma\alpha\frac{(\gamma H)^2(1+\alpha^2)+\omega^2}{(\gamma H)^4(1+\alpha^2)^2+2(\omega\gamma H)^2(\alpha^2-1)+\omega^4}, \end{aligned} \tag{2.60}$$

and accordingly,

$$\begin{aligned} \chi''^{G}(H) &= \mathrm{Im}[\chi^{G}(H)] \\ &= N_p\mu_p\omega\gamma\alpha\frac{(\gamma H)^2+\omega^2(1+\alpha^2)}{(\gamma H)^4+2(\omega\gamma H)^2(\alpha^2-1)+\omega^4(1+\alpha^2)^2}, \end{aligned} \tag{2.61}$$

for the Gilbert damping[5]

As can be seen in Eq. 2.60 - Eq. 2.61 both line shapes are very similar in their mathematical structure, one main difference is that the factor $1+\alpha^2$ is placed at the external field H in the Landau-Lifshitz model, while it stands with $H_\omega = \omega/\gamma$ in the Gilbert model. Formally, the Gilbert line shape eq. 2.57 can be obtained from the Landau-Lifshitz line shape eq. 2.56 by replacing the gyromagnetic ratio γ by $\gamma/(1+\alpha^2)$. For $\alpha \ll 1$ both line shapes conincide.

In Sec. 5 the behaviour of resonance field H_{res} and line-width ΔH_{pp} of both line shape models are investigated in detail to describe the temperature-dependent behaviour of $\mathrm{Fe}_x\mathrm{Pt}_{1-x}$ nanoparticles found in the MRS-spectra.

2.2.4 Resonance conditions

Alternatively, the equation of motion can be expressed in terms of the free energy F. The general resonance condition (without damping) is then obtained from the derivatives of the free energy density $F(\theta,\phi)$ in spherical coordinates with polar angle θ and azimuthal ϕ of the equilibrium magnetic moment [36]

$$\omega = \frac{\gamma}{M_{\mathrm{S}}\sin\theta}\sqrt{F_{\theta\theta}F_{\phi\phi}-F_{\theta\phi}^2} \tag{2.64}$$

---

[5] Again, using $H_\omega = \omega/\gamma$ eq. 2.56 and eq. 2.61 can be written more compactly

$$\chi''^{L}(H) = N_p\mu_p\gamma^2\alpha H_\omega\frac{H^2(1+\alpha^2)+H_\omega^2}{H^4(1+\alpha^2)^2+2H^2H_\omega^2(\alpha^2-1)+H_\omega^4}, \tag{2.62}$$

and

$$\chi''^{G}(H) = N_p\mu_p\gamma^2\alpha H_\omega\frac{H^2+H_\omega^2(1+\alpha^2)}{H^4(1+\alpha^2)^2+2H^2H_\omega^2(\alpha^2-1)+H_\omega^4}. \tag{2.63}$$

$$= \frac{\gamma}{M_\mathrm{S}}\sqrt{F_{\theta\theta}\left(\frac{F_{\phi\phi}}{\sin^2\theta} + F_\theta\frac{\cos\theta}{\sin\theta}\right) - \left(\frac{F_{\theta\phi}}{\sin\theta} - F_\phi\frac{\cos\theta}{\sin^2\theta}\right)}, \qquad (2.65)$$

using the short notation $F_{xy} \equiv \partial(\partial F/\partial x)/\partial y$ for the partial derivatives. The resonance condition Eq. 2.65 is an extension of Eq. 2.64 [37] also including the case $\theta = 0$ [38]. Together with the resonance conditions requires the minimization of the free energy $F_\theta \overset{!}{=} 0$ and $F_\phi \overset{!}{=} 0$ to obtain the equilibrium of the magnetic moment orientation.

The intrinsic resonance line width is given by [36]

$$\Delta\omega = \frac{\gamma}{M_\mathrm{S}}\left(F_{\theta\theta} + \frac{1}{\sin^2\theta}F_{\phi\phi}\right); \qquad (2.66)$$

$$\Delta B_i = \frac{\partial B}{\partial\omega}\Delta\omega, \qquad (2.67)$$

where the intrinsic resonance line width ΔB is obtained from the frequency line width $\Delta\omega$.

2.2.5 Damping and linewidth

The spin-orbit interaction is the main microscopic origin of damping effects observed in resonance absorption. In a simple picture it is assumed that the orbital magnetic moment which is coupled to the precession of the spin moment is distorted by phonons leading to a phase shift, and thus damping of the resonance. It has been shown that the damping α is proportional to the spin-orbit coupling constant [39] $\alpha \propto \gamma^2(\Delta g)^2\xi^2$, where Δg is the difference of the g-factor of the nanoparticles with the g-value of the free electron $g \approx 2.0023$.

In magnetic systems with small spin-orbit interaction the ratio between angular μ_L and spin moments μ_S can be determined from the g-factor [40; 41; 42]

$$\mu_L/\mu_S = (g-2)/2. \qquad (2.68)$$

Chapter 3

Materials and Methods

3.1 Iron-platinum alloys Fe_xPt_{1-x}

Since many years the Fe-Pt system has been intensely investigated for its interesting magnetic properties and the variety of crystallographic structures. At the beginning of 1900 studies were focussing on bulk Fe_xPt_{1-x} compositions used as material for permanent magnets [43; 44; 45; 46]. From 2000 onwards, the Fe-Pt system experienced a revival when magnetic nanoparticles became interesting as potential materials for high density recording media [4; 47]. Here, most attention was drawn to Fe_xPt_{1-x} systems near the equiatomic state $x = 0.5$, since these alloys show a huge uniaxial magnetocrystalline anisotropy of $K_1 \approx 10^6 J/m^3$ in the ordered state [48]. The resulting high coercivity is essential for the thermal stability of such a material used in a storage medium.

But besides the technical application, Fe_xPt_{1-x} is interesting for the investigation of fundamental effects in magnetism. Platinum-rich alloys with $x < 0.45$ exhibit interesting magnetic properties [49], with a competition between antiferromagnetism and ferromagnetism depending on composition x and structural order. Relatively little focus has been put onto Fe_xPt_{1-x} with $x < 0.3$ [50] or highly diluted compositions with $x < 0.1$ [51]. Additionally, iron-rich Fe_xPt_{1-x} alloys were intensely investigated to study the thermodynamics of the Invar effect [52], which denotes the uniquely low coefficient of thermal expansion observed at $x \approx 0.65 \ldots 0.75$ analogous to fcc Ni-Fe alloys with the same Fe content.

3.1.1 Structural properties

Binary intermetallic $\mathrm{Fe}_x\mathrm{Pt}_{1-x}$ sytems form stable alloys over the whole concentration range x, as shown in the phase diagram of Fig. 3.1. At high temperatures Fe and Pt are miscible at any ratio resulting in a disordered fcc solid solution ($A1$)[45; 53]. The transition from a chemically disordered to an ordered phase by annealing is driven by volume diffusion and kinetically suppressed, so it becomes infinitely slow at temperatures below 600°C in conventional bulk alloys. The fraction of the ordered phase increases with the annealing time. A correlation between lattice constant a_0 and iron concentration x has been found experimentally [54] for disordered $\mathrm{Fe}_x\mathrm{Pt}_{1-x}$.

In thermodynamic equilibrium, three stable chemically ordered phases are observed [45]. At low iron concentration, $\mathrm{Fe}_x\mathrm{Pt}_{1-x}$ alloys with x in the range $0.18 \leq x \leq 0.45$ order in a stable fcc $\mathrm{Cu_3Au}$ type superstructure ($L1_2$) below 1350°C. The platinum-rich $\mathrm{FePt_3}$ alloys show antiferromagnetic ordering.

$\mathrm{Fe}_x\mathrm{Pt}_{1-x}$ alloys close to the equiatomic composition ($0.45 \leq x \leq 0.65$) exhibit a disorder-order transformation from the $A1$ state to an ordered fct CuAu-type superstructure ($L1_0$) by annealing at temperatures between 600°C and 1300°C [55; 56; 57]. The $L1_0$ phase of ordered FePt consists of alternating layers of Fe and Pt along a (100)-direction, where the different atomic radii of Fe $\mathrm{r_{Fe}} = 1.24$ Å and Pt $\mathrm{r_{Pt}} = 1.39$ Å [58] induce a tetragonal distortion (contraction) of the otherwise cubic lattice. The bulk lattice parameter are a=3.838 Å and c=3.715 Å in the ordered state [59] and a=3.804 Å in the disordered $A1$-state.

At high iron concentrations $\mathrm{Fe}_x\mathrm{Pt}_{1-x}$ alloys with x in the range $0.65 \leq x \leq 0.85$ order in a $L1_2$ superstructure below 750°C. A lattice constant of 3.72 Å has been reported [60]. The iron-rich $\mathrm{Fe_3Pt}$ alloys show ferromagnetic behaviour.

Finally, iron-rich compositions with $x > 0.85$ form a bcc structure (α-Fe) below 900°C, which also is ferromagnetic.

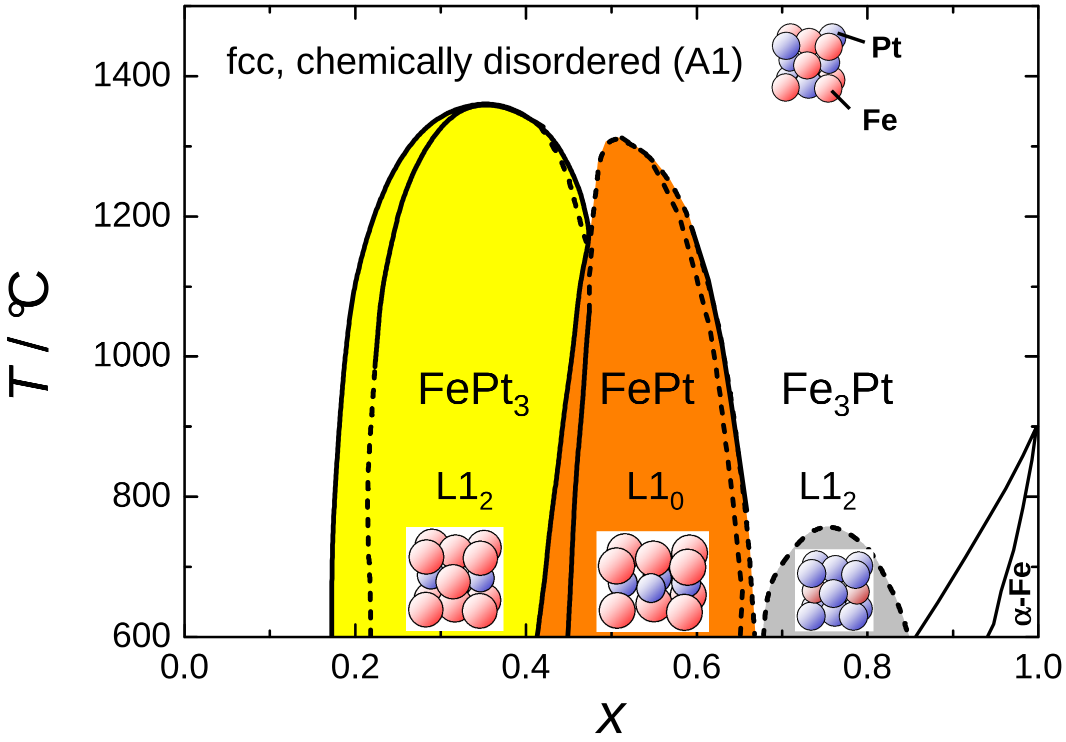

Figure 3.1: Phase diagram of Fe_xPt_{1-x} alloys (adapted from [61]).

3.1.2 Ferromagnetism and Antiferromagnetism in Fe_xPt_{1-x} -alloys

The magnetocrystalline anisotropy energy of Fe_xPt_{1-x} As introduced in section 2.1.1, the magnetocrystalline anisotropy is related to magnitude and anisotropy $\Delta\mu_L$ of the orbital magnetic moment μ_L. In the binary itinerant Fe_xPt_{1-x} system consisting of a $3d$ (Fe) and a $5d$ (Pt) element, the total moment cannot be attributed to the Fe moment alone. Hybridization and Polarization effects have to be taken into account. Therefore, an influence of composition and order in Fe_xPt_{1-x} nanoparticles on the magnetocrystalline anisotropy is expected. From the corresponding g-factor, the effective ratio $\mu_L^{\text{eff}}/\mu_S^{\text{eff}}$ is obtained. Fe_xPt_{1-x} follows the Slater-Pauling rule describing the dependence of the magnetic moment μ on the iron concentration $\mu(x)$[54]. Furthermore, saturation magnetization M_S and Curie temperature T_C crucially depend on the composition x and chemical order in Fe_xPt_{1-x} nanoparticles [62] as depicted in Fig. 3.2. The saturation magnetization M_S is linearly increasing with increasing iron content x of the Fe_xPt_{1-x} nanoparticles (omitting the compostion range $x = 0.25 \ldots 0.33$ where antiferromagnetic behaviour of the chemically ordered structure has been observed[50].

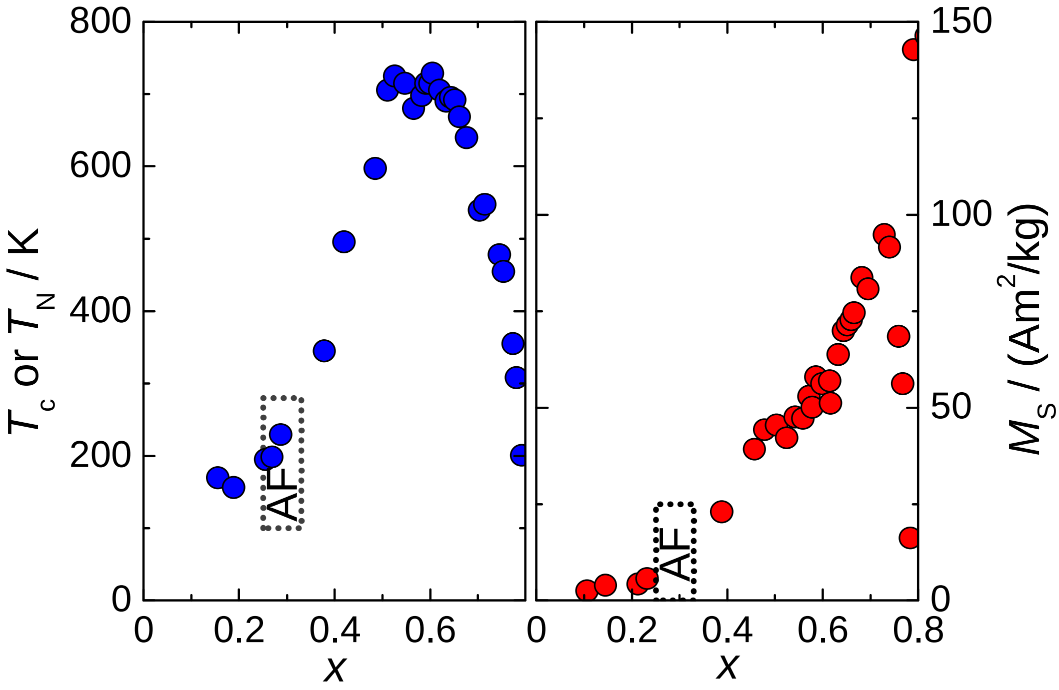

Figure 3.2: Curie temperature T_C or Néel temperature T_N (left panel) and room temperature saturation magnetization M_S (right panel) as a function of composition x in ordered $\mathrm{Fe}_x\mathrm{Pt}_{1-x}$ nanoparticles. The dotted area mark the composition range x where antiferomagnetic order has been observed in $\mathrm{Fe}_x\mathrm{Pt}_{1-x}$ alloys. Adapted from [62].

FePt$_3$

Completely disordered FePt$_3$ ($A1$-phase) has an fcc structure in which each lattice site is occupied with 25% probability by an Fe and 75% by a Pt atom. FePt$_3$ is ferromagnetic in the chemically disordered state with Fe moments of 2 μ_B and a Curie temperature in the range of $T_\mathrm{C} = 360 \ldots 400$ K.

In the chemically ordered $L1_2$-phase FePt$_3$ exhibits antiferromagnetism with two different magnetic phases, as observed by neutron scattering [50; 63; 64]. In the $Q1$-phase with Néel temperature $T_{\mathrm{N}1} = 160$ K, the Fe moments are located in alternating ferromagnetic layers along the (110) plane, and the antiferromagnetic unit cell is given by doubling of the $L1_2$ unit cell along the (001)- and

(010)-axis [49]. In this configuration, the Fe atoms carry a magnetic moment of about 3.3 μ_B. In slightly iron-enriched $FePt_3$ the $Q1$-phase changes into a second antiferromagnetic $Q2$-phase below $T < T_{N2}$ =100 K. The Fe moments are now located in alternating ferromagnetic layers along the (100)-plane with a magnetic moment of about 2.0 μ_B. The unit cell in this phase is here given only by doubling of the $L1_2$ unit cell along the (001)-axis. It is important to note that only the Fe atoms carry a magnetic moment in both antiferromagnetic phases without inducing any moment at the Pt sites. Antiferromagnetism was also reported for ordered $FePt_3$ nanoparticles [65]. The appearance of antiferromagnetism in ordered $FePt_3$ with x in the range $0.22 \ldots 0.34$ is strongly dependent on the composition [66; 67]. As displayed in Fig 3.3 (adapted from [50]), the antiferromagnetic ordering occurs at $T \approx 110$ K emerging as a cusp in the magnetization data.

Additionally, by plastic deformation, which can be obtained by cold working of the chemically ordered alloy, chemical disorder is introduced [68] with consequential increased dislocation densities, e. g. Fe atoms occupying face centered positions rather than corner positions in the fcc ordered lattice. By this, positive exchange between next neighbour Fe atoms introduces a tendency to ferromagnetic order.

FePt

In the disordered state ($A1$-phase), the equiatomic FePt alloy shows ferromagnetic behaviour with a vanishingly small cubic magnetocrystalline anisotropy (observed in thin films) of $K_1 \approx 6 \cdot 10^3$ J/m^3 [69], and therefore only a low thermal stability. In the ordered state ($L1_0$-phase), the regular arrangement of Fe- and Pt-layers leads to a tetragonal distortion of the crystal structure (along the c-axis), which induces by large spin-orbit coupling (mediated by Pt atoms) the high uniaxial anisotropy with $K \approx 6 \cdot 10^6$ J/m^3 [4; 70; 71]. This leads to a transition from a magnetic soft material without significant coercivity for disordered FePt to a hard magnet with a tremendous increase of coercivity up to 9 kOe in thin films [72]. For these high anisotropy and coervicity values FePt storage devices with recording densities up to 1 Tbit/in^2 have been predicted [73].

In the ferromagnetic phase of the ordered FePt alloys, the Fe-atoms as well

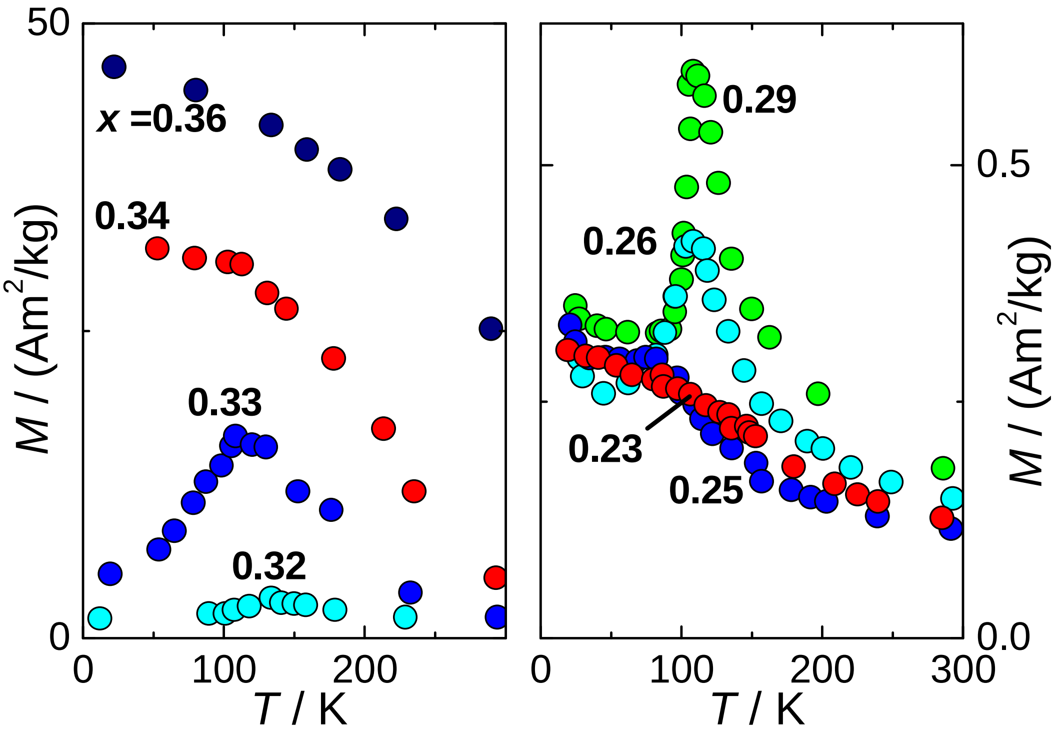

Figure 3.3: Competition between ferromagnetism and antiferromagnetism in ordered platinum-rich Fe_xPt_{1-x} bulk alloys revealed by the variation of magnetization M with temperature T measured in a magnetic field $H = 8.2$ kOe. Note, the different scales of the magnetization M. Adapted from [50].

as the Pt-atoms show a magnetic moment of 2.83 μ_B and 0.41 μ_B, respectively. The induced magnetic moment at the Pt atom is resulting from its eight nearest Fe neighbours.

For bulk FePt [74] as well as FePt nanoparticles [62], a Curie-temperature of about 670 K has been reported. The room temperature saturation magnetization M_S of about 43 Am^2/kg for disordered bulk FePt is slightly larger than the value of about 40 Am^2/kg for ordered FePt [45; 60]. For 15 nm ordered FePt nanoparticles, a saturation magnetization of about 40 Am^2/kg has been found [62]. A comparatively large critical single domain diameter of 600 nm has been found for FePt-particles [15].

Fe_3Pt

Chemically disordered Fe_3Pt shows ferromagnetic order below $T_C < 297$ K with a magnetic moment per unit cell of 4.5 μ_B/iron atom [75]. Although the Invar effect (negative coefficient of thermal expansion) is more pronounced in the disordered state of Fe_3Pt, the saturation magnetization value of about 100 Am^2/kg [60] and Curie constant seem to be independent of structural order.

3.2 Preparation of Fe-Pt nanocrystals

3.2.1 Organometallic synthesis of Fe_xPt_{1-x} nanocrystals

The preparation of the Fe_xPt_{1-x} nanoparticles which are investigated in this work was carried out at the Institute of Physical Chemistry at Hamburg University. Comprehensive synthesis and chemistry details of sample preparation can be found in the thesis of E. Shevchenko [76]. The approach followed the wet-chemical organometallic route for Fe-Pt nanoparticles presented by Sun [4] in 2000. A general overview of the organometallic nanoparticle synthesis leading to narrow size distributions was given by Murray et al. [77].

As shown schematically in Fig. 3.4, the preparation of crystalline Fe_xPt_{1-x} nanoparticles consists of a short-perioded nucleation phase followed by a prolonged growth and healing period of the seed nuclei. This is achieved under airless conditions by a rapid addition of iron pentacarbonyl ($Fe(CO)_5$) precursor together with a binary stabilizer mixture of oleic acid/oleyl amine into a 100°C hot solution of platinum(II)-acetylacetonate ($Pt(acac)_2$) dissolved in a coordinating mixture of hexadecanediol and dioctylether. The stabilizing agents will reversibly adsorb to the nanoparticle surface thereby mediating the growth rate and hindering the formation of larger (bulk) particles. Thus, each nanoparticle consists of an inorganic and at first disordered crystalline Fe_xPt_{1-x} core surrounded by an organic layer of oleic acid/oleyl amine to stabilize the colloidal suspension against agglomeration and to prevent the cores from oxidizing.

To improve the crystallinity the solution is subsequently boiled under argon atmosphere for 30 min at 300°C to heal crystal defects and afterwards slowly cooled down to room temperature, followed by washing steps to remove the excess of organic materials. To narrow the nanoparticle size distribution, size-selective precipitation steps have been carried out under ambient atmosphere

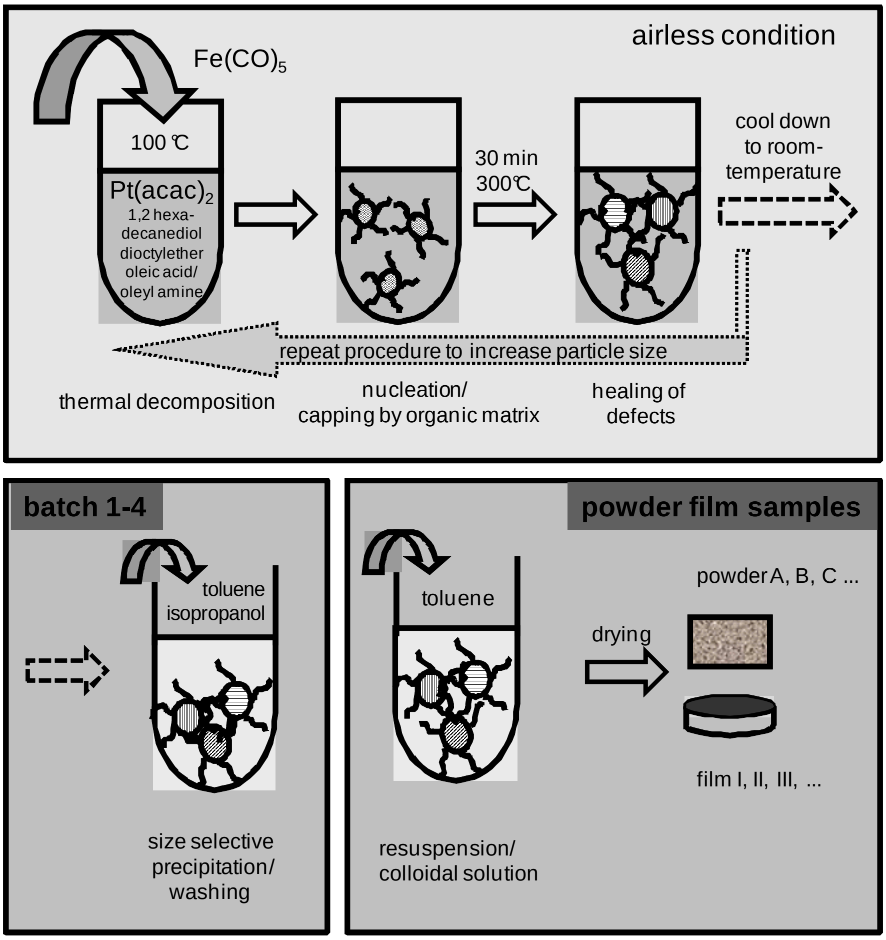

Figure 3.4: Synthesis scheme for Fe_xPt_{1-x} nanoparticles by thermal decomposition following the organometallic route [4].

by slowly titrating non-solvent ethanol into the suspension of nanocrystals. This procedure can be repeated to further narrow the size distribution, as long as the resulting nanoparticle yield is sufficient.

Finally, the nanoparticles are redispersed in a non-polar organic solvent (toluene) for storage making up the individual stable colloidal batches from which particular powder and film Fe_xPt_{1-x} samples[1] were prepared by drying which then were employed in this work for structural (TEM, XRD) and magnetic characterization (magnetometry, magnetic resonance spectroscopy), see Sec. 4.1-5.

---

[1] Several Fe_xPt_{1-x} nanoparticle film samples have been produced by evaporation of the nanoparticle solution on a sapphire substrate, but due to their poor quality and stability they are not considered in this work

3.2.2 $\mathrm{Fe}_x\mathrm{Pt}_{1-x}$ samples prepared for magnetic characterization

For magnetic characterization individual $\mathrm{Fe}_x\mathrm{Pt}_{1-x}$ samples have been produced out of the basic colloidal nanoparticle batches prepared as described in the previous chapter 3.2.1. Theses samples were dried by evaporating the organic solvent under argon atmosphere. This yielded black to grey-brown powder samples of 5 to 30 mg weight, which then were filled into gelatine capsules for the magnetic measurements. Table 3.1 shows a compilation of the samples, which have been investigated in this work.

sample-name	batch	as synth. weight m(mg)	annealing m (mg)/treatment/T_{max} (K)
A	II	18.9	7.8 / MRS-ht / 530
B	II	20.2	5.0 /furnace/820
C	III	25.8	10.0 / MRS-ht / 630
			2.5 /SQUID-oven /640
D	IV	16.4	5.5 / MRS-ht /635
E	IV	7.0	6.5 /MRS-ht / 545

Table 3.1: Overview of $\mathrm{Fe}_x\mathrm{Pt}_{1-x}$ nanoparticle powder samples. Listed are sample name and colloidal batch together with the *as synthesized* sample mass. In the course of magnetic measurements, some samples have been divided into smaller fractions to investigate the influence of annealing on chemical order and magnetic behaviour. Therefore, partial masses, type of annealing, and maximum temperature are quoted.

3.2.3 Annealing of $\mathrm{Fe}_x\mathrm{Pt}_{1-x}$ nanoparticle samples

In the course of magnetic characterization, some samples have been divided into smaller fractions in order to investigate changes in chemical order by annealing of the $\mathrm{Fe}_x\mathrm{Pt}_{1-x}$ samples. This was done for sample B in a furnace under N_2 inert gas atmosphere for 2 hours at 820 K, during the MRS-measurements using the heater up 640 K, or for a fraction of sample C in the SQUID-oven at 640 K. Therefore, the corresponding partial masses, type of annealing, and maximum temperature are quoted in Tab. 3.1.

3.3 Structural characterization techniques

The structural characterization of the nanocrystals was carried out at the Institute of Physical Chemistry using the two well-established techniques Transmission Electron Microscopy (TEM) and X-ray Diffraction (XRD), respectively.

3.3.1 Transmission electron microscopy (TEM)

TEM images were obtained using a Philips CM-300 microscope operated at 300 kV. All samples for TEM-measurements had to be individually prepared by depositing a droplet of the nanocrystal suspension batch onto a 400 mesh carbon-coated copper grid. The excess of solvent was sponged up by filter paper, and the grids were dried in air to evaporate the organic solvent. Therefore, it can not be ruled out that the structure of the sample, especially the surfactant, may be changed during this drying process. Additionally, high resolution imaging (HRTEM) of the crystallographic structure of the nanoparticles at an atomic scale was performed with the same device.

3.3.2 X-ray Diffraction

Crystallinity, mean size, composition, and structural order of the $\mathrm{Fe}_x\mathrm{Pt}_{1-x}$ nanoparticles were investigated by X-ray diffraction. These measurements were performed on a Philips X'Pert diffractometer operated at a wavelength $\lambda = 1.54$ Å (Cu K_α radiation[2]), in a Bragg-Brentano θ-2θ geometry using a secondary monochromator. As for TEM measurements the samples for XRD had to be prepared directly from the $\mathrm{Fe}_x\mathrm{Pt}_{1-x}$ batches by depositing single droplets of the nanoparticle suspension onto standard single crystal Si supports and drying in air by evaporating of the organic solvent. Additionally, some of the powder samples prepared for magnetic measurements were measured by XRD after their magnetic characterization. See table 3.1 for sample assignment details.

---

[2] Cu $\mathrm{K}\alpha_1$=1.54056 Å, Cu $\mathrm{K}\alpha_2$=1.54439 Å, $\mathrm{I}(\alpha_2/\alpha_1)$=0.497

3.4 Magnetic characterization techniques

3.4.1 SQUID-Magnetometry

For the main magnetic characterization of the $\mathrm{Fe}_x\mathrm{Pt}_{1-x}$ nanocrystals a commercial SQUID-magnetometer (MPMS_2, Quantum Design[3], San Diego) was used. The magnetometer allows sensitive detection of magnetic moments down to 10^{-11} Am^2 with high accuracy in the presence of an static external magnetic field to magnetize a sample. The moment detection is based on a rf-SQUID sensor (SQUID=Superconducting Quantum Interference Device) connected to a superconducting flux transformer wound in a second order gradiometer pick-up coil configuration in order to suppress effects of the static magnetic field and external interfering stray fields. Static magnetic fields up to ±1 T (±10 kOe) with a resolution of 0.1 μT (10 mOe) are provided by a superconducting magnet housing the gradiometer coil. The sample temperature can be varied continuously over the range 1.3 K to 350 K, with a stability of better than 0.1 K.

For accurate mounting of samples two thin paper strips folded across are inserted half-way up a plastic drinking straw, providing a robust sample support on which either a powder sample within a gelatine capsule or a sapphire disk with a $\mathrm{Fe}_x\mathrm{Pt}_{1-x}$ film on top was fixed. The straw with a sample inside was then connected with the transport unit of the magnetometer. From background measurements without sample, a parasitic diamagnetic susceptibility of about $-5 \cdot 10^{-8}$ Am^2/T ($=-5 \cdot 10^{-9}$ emu/Oe) arising from the paper sample support was determined.

Additionally, an AC-option was an integral part of the magnetometer, allowing for the detection of the real and imaginary parts of the magnetic response of a sample to a sinusoidal magnetic excitation. To this end, AC-fields in the frequency range up to 1 kHz and at amplitudes up to 2 Oe were provided by a small integrated copper coil wound around the gradiometric pick-up coil.

Optionally, an oven could be inserted into the device, allowing for magnetic measurements at elevated sample temperatures up to 650 K. In this case, the sample had to be transferred from the gelatine capsule into a temperature-resistant glass teflon sample holder.

To reduce interfering external rf-noise entering the pick-up the magnetome-

---

[3] Magnetic Property Measurement System 2

ter was operated within an electrically shielded room. Furthermore, by means of a three-axis Helmholtz coil system located outside the He-Dewar, the earth's magnetic field at the sample position was suppressed.

Further technical details of the MPMS$_2$ magnetometer are found in [78].

Measurement modi

The DOS-based control software of the magnetometer allows automatic measurement sequences in the given field and temperature ranges. The following standard sequences for magnetic measurements of Fe$_x$Pt$_{1-x}$ nanoparticles were used (see table 3.2). From the measured magnetic moment of a sample the corresponding magnetization has been derived by division of the sample mass.

Magnetization isotherms, $M(H)$, at a fixed temperature the magnetic moment of the sample is measured at different field values within the full magnetic field range. At low temperatures a full cycle of magnetic field values ($+1$ T $\rightarrow -1$ T $\rightarrow +1$ T) is performed in order to obtain a full hysteresis loop.

Zero field cooled magnetization, $M_{\mathrm{ZFC}}(T)$. After cooling the sample in zero magnetic field down to 5 K, the magnetic moment in a moderate magnetic field of 100 Oe (10 mT) is measured while step-wise increasing the temperature up to 350 K. Subsequently, the **Field cooled magnetization,** $M_{\mathrm{FC}}(T)$ is recorded, where the magnetic moment of a sample is measured in a magnetic field of 100 Oe sweeping the temperature from 350 K down to 5 K. **Remanence magnetization,** M_{rem}. After cooling of the sample down to 5 K in a magnetic field of 100 Oe, the magnetic field is removed and the magnetic moment is detected while step-wise increasing the temperature. **AC magnetization,** $M_{\mathrm{AC}}(T)$. Here, the real and imaginary parts of the complex dynamic magnetic moment at five different driving frequencies (of 2 Oe amplitude) are detected while stepwise increasing the temperature after cooling the sample down to 5 K in zero magnetic field.

3.4.2 Magnetic Resonance Absorption

For magnetic resonance absorption measurements a microwave spectrometer operating in the GHz frequency range was built within this work. Primarily, the device was designed for investigation of the dynamic magnetic absorption

type	name	range	fixed parameter	sample history
$M(H)$	magnetization isotherms	$H = -1$ T ...1 T	T	-
$M_{\mathrm{ZFC}}(T)$	zero field cooled	$T = 5$ K...350 K	$H = 100$ Oe	cooling to start temperature in zero field
$M_{\mathrm{FC}}(T)$	field cooled	$T = 350$ K...5 K	$H = 100$ Oe	starting at highest temperature
$M_{\mathrm{rem}}(T)$	remanence magnetization	$T = 5$ K...100 K	$H = 0$ Oe	after cooling in 100 Oe magnetizing field
$M_{\mathrm{AC}}(T)$	AC susceptibility	$T = 5$ K...300 K	$H_{\mathrm{AC}} = 2$ Oe $f = 0.1, 1, 10, 93, 928$ Hz	after cooling in zero magnetic field

Table 3.2: Standard sequences used for magnetic measurements of $\mathrm{Fe}_x\mathrm{Pt}_{1-x}$ samples with the MPMS_2 magnetometer.

of $\mathrm{Fe}_x\mathrm{Pt}_{1-x}$ samples at X-band frequencies (8...10 GHz) and different temperatures (15 K...600 K). All magnetic resonance experiments were performed at a fixed frequency by slowly sweeping an external magnetic field, which is common technique nowadays. Therefore, resonant cavities could be used exposing the sample to a defined microwave field pattern, which is aligned perpendicular to the external magnetic field. The geometric field configurations within the cavity are shown in Fig. 3.5.

Characteristic parameters of the main components of the microwave spectrometer setup are summarized in Tab. 3.3. Photographs of the device are shown in Fig. 3.6 and 3.8.

Microwave spectrometer setup

Microwave synthesizer The microwave power was generated by a synthesized swept signal generator (Hewlett Packard HP 83624 A), providing microwave radiation in the frequency range 2 to 20 GHz (L and X-band) in steps of 1 kHz and a power range -20 dBm to 20 dBm[4]. By an additional microwave multiplier the frequency range could be extended up to 60 GHz enabling for cavities operating in the K, Q, U-band. Accuracy and frequency stability of the synthesized microwave radiation was in the range of a few Hz.

---

[4] This corresponds to 0.01 ... 100 mW.

component	device name	specification
microwave generator	HP 83624 frequency range power	3-band synthesizer (10 MHz clock) 2...20 GHz,$\Delta f = 1$ kHz $-20... + 20$ dBm, $\Delta P = 0.02$ dBm
external field magnet	Bruker EPR-Magnet pole shoes	$H_{\max} = \pm 1.2$ T $d = 30$ cm, $b = 6$ cm
power supply	F.u.G. HTN 5000 M-2500 max voltage max current	voltage controlled 2000 V 2.5 A≡5 kW

Table 3.3: Characteristic parameters of the microwave spectrometer components.

Resonant cavities The temperature dependent magnetic resonance measurements were done at X-band frequencies in a gold-plated rectangular resonant cavity (Varian V-4531). Mainly used was the TE_{102} eigenresonance mode, which for the unloaded cavity lay at 9.095 GHz with a high quality factor of about 5000 (Q-factor, proportional to the resonance width). Due to sample material and the glass elements of the cryostat in the resonant cavity the resonance was slightly shifted (≈ 0.1 GHz for the glass Dewar inset) and the Q-factor reduced to about 2000-3000. The optimal coupling of the microwave radiation could be tuned by a small screw in the cavity aperture. A pair of copper coils were integrated in the two cavity walls normal to the external magnetic field, which enabled a field modulation to enhance the sensitivity using lock-in-technique (see paragraph signal detection below). In vertical direction (top and bottom plate) of the cavity a centred 10 mm wide bore was available through which the samples could conveniently be inserted and positioned. Figure 3.5 shows a sketch of the cavity together with the microwave, external sweeping and modulating field configuration.

In addition, several other gold-plated resonance cavities were at disposal, designed for operation at S-band (2-4 GHz) and K-band (12-40 GHz) frequencies, respectively.

For room temperature measurements without the flow cryostat sample holders made of teflon or acrylic glass were used. These holders were tested for

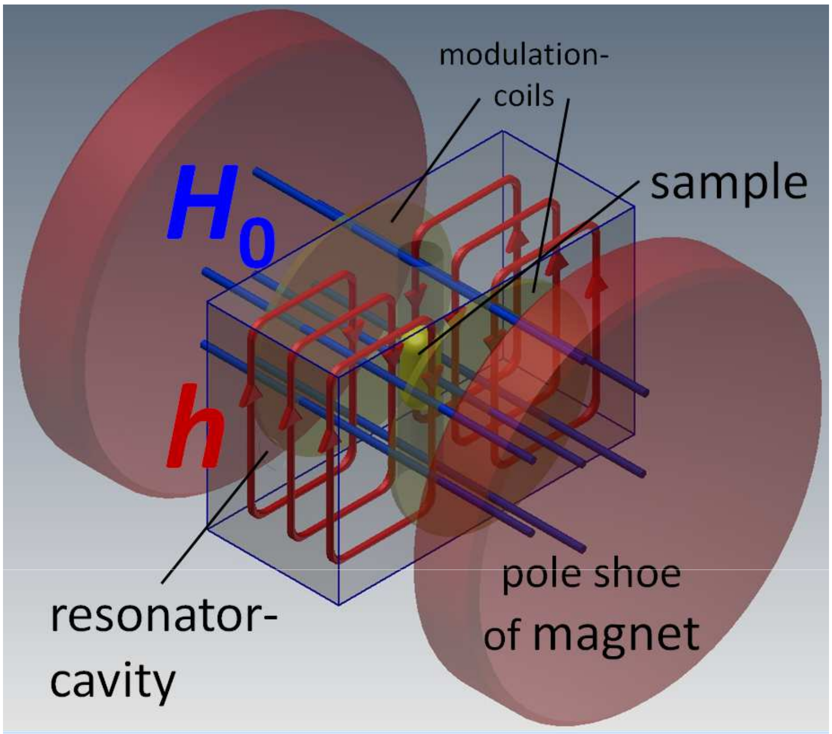

Figure 3.5: Magnetic field configuration of microwave $\vec{h}$, static $\vec{H}_0$ (blue), and modulating fields within the resonator cavity. The sample (yellow) is positioned (mounted in a cuvette or teflon sample holder) through the vertical bore at the cavity center in the maximum of the TE_{102}-mode microwave field b (red lines).

magnetic impurities by measurements without nanoparticle sample.

An automatic frequency control (AFC) was employed to adjust the microwave synthesizer to the resonance frequency of the loaded resonator. This was necessary to account for changes of the cavity eigenresonance while passing through the resonance of a sample or due to temperature changes of the cavity. Therefore, the cw-signal of the microwave synthesizer was frequency modulated and phase sensitive rectified by the internal AFC lock-in amplifier. Sign and amplitude of the AFC were fed back into the synthesizer to track the output microwave frequency.

In a similar way, the fine-tuning of the synthesizer frequency to match the eigenresonance of the cavity was accomplished with aid of the AFC. For this, the synthesizer frequency was gently changed until the AFC output signal was adjusted to zero.

External field magnet For sweeping the external magnetic field a water-cooled Varian 4012A electromagnet with a maximum field amplitude of about 1.2 T was used. An air gap of 6 cm between the pole shoes of the magnet offers sufficient space to house the resonant cavity and the cryostat. Due to the large pole shoe diameter of 30 cm of the magnet, a magnetic field homogeneity $\Delta H/H$ of better than 10^{-6} at the sample position could be achieved. The magnet was connected to a controllable high-voltage 5 kW power supply (HTN 5000 M-2500, F.u.G. Elektronik GmbH, Rosenheim). By aid of a manual switch, the field polarity could be reversed. The control of the power supply output feeding the magnet was carried out by an analogue dc voltage in the range 0..10 V, either connected to an electro-mechanical voltage ramp generator or to a 12 bit I/O card controlled by the measurement program. In the latter case the step size of the magnetic field could be further refined using a voltage divider (1:2), resulting in a step-size of about 1 Oe at cost of a reduced maximum magnetic field of 7 kOe. Much smaller step-sizes could be achieved using the voltage ramp generator.

The strength of the external magnetic field was detected by a hall probe mounted at one of the magnet's pole shoes. The calibration of the hall probe was checked at regular intervals by means of DPPH[5], a substance which is used as a standard g-marker in electron paramagnetic resonance (g_0=2.0036) to calibrate resonance field and intensity. An example is shown in Fig. 3.7, where from the nominal resonance field offset and voltage to field conversion factor of the digital multimeter used for data acquisition are determined.

Signal detection and data acquisition For the detection of the reflected microwave radiation a Ge-crystal diode was used. The sensitivity of the microwave detection was further increased using a lock-in technique modulating the external magnetic field. To this end, a weak magnetic AC-field (provided by a coil pair in the walls of the resonant cavity operated at a frequency of about 130 Hz and a maximum amplitude of 1 Oe) was superimposed to the external magnetic field, leading to a modulation of the resonance absorption signal. The output signal of the detector diode was then demodulated by a reference modulation signal, bandpass filtered and amplified using a single-

---

[5] $C_{18}H_{12}N_5O_6$: 1,1-diphenyl-2-picryl-hydrazyl, stable free radical

channel lock-in amplifier. Due to the lock-in technique, the first derivative $d\chi''/dH$ of the microwave absorption (imaginary part of the dynamic susceptibility $\chi(H)$) is obtained. By this, the signal-to-noise ratio could be improved up to 4 orders of magnitude.

Temperature control For measurements different from room temperature an evacuated double-walled quartz tube containing the sample was inserted into the bore of the resonant cavity. Keeping the cavity at room temperature, the sample could either be cooled by means of a continuous helium flow cryostat (Oxford ESR 900) down to 15 K, or heated up to 600 K by an external Pt-resistance wire wound around a sapphire sample support. A needle valve in the Helium flow was used to control the Helium gas flow of the cryostat, thereby adjusting the temperature manually. The temperature of the sample was recorded using a germanium thermometer in the flow channel. Resonance measurements at higher sample temperatures were achieved by placing the sample on top of a sapphire rod in the cavity. Five turns of a Pt-resistance wire are wound closely around the middle part of the sapphire rod, transferring heat generated in the wire by a dc current. A Pt-100 thermometer placed at the same distance of the wire from the sample, but at the bottom of the sapphire rod was used to control the temperature of the sample.

Measurement control The measurements were controlled by computer using the IEC bus communication standard and the object oriented programming language HPVee. Several programs were written to match particular measurement requirements. Changing the field polarity of the magnet and the temperature control had to be done manually.

Measurement procedures

All resonance absorption measurements were performed at a fixed frequency (main eigenresonance modes of the cavity), slowly (≈ 1 Oe/s) sweeping the external magnetic field. In most cases, a full field cycle was performed to check for hysteretic effect in the resonance absorption.

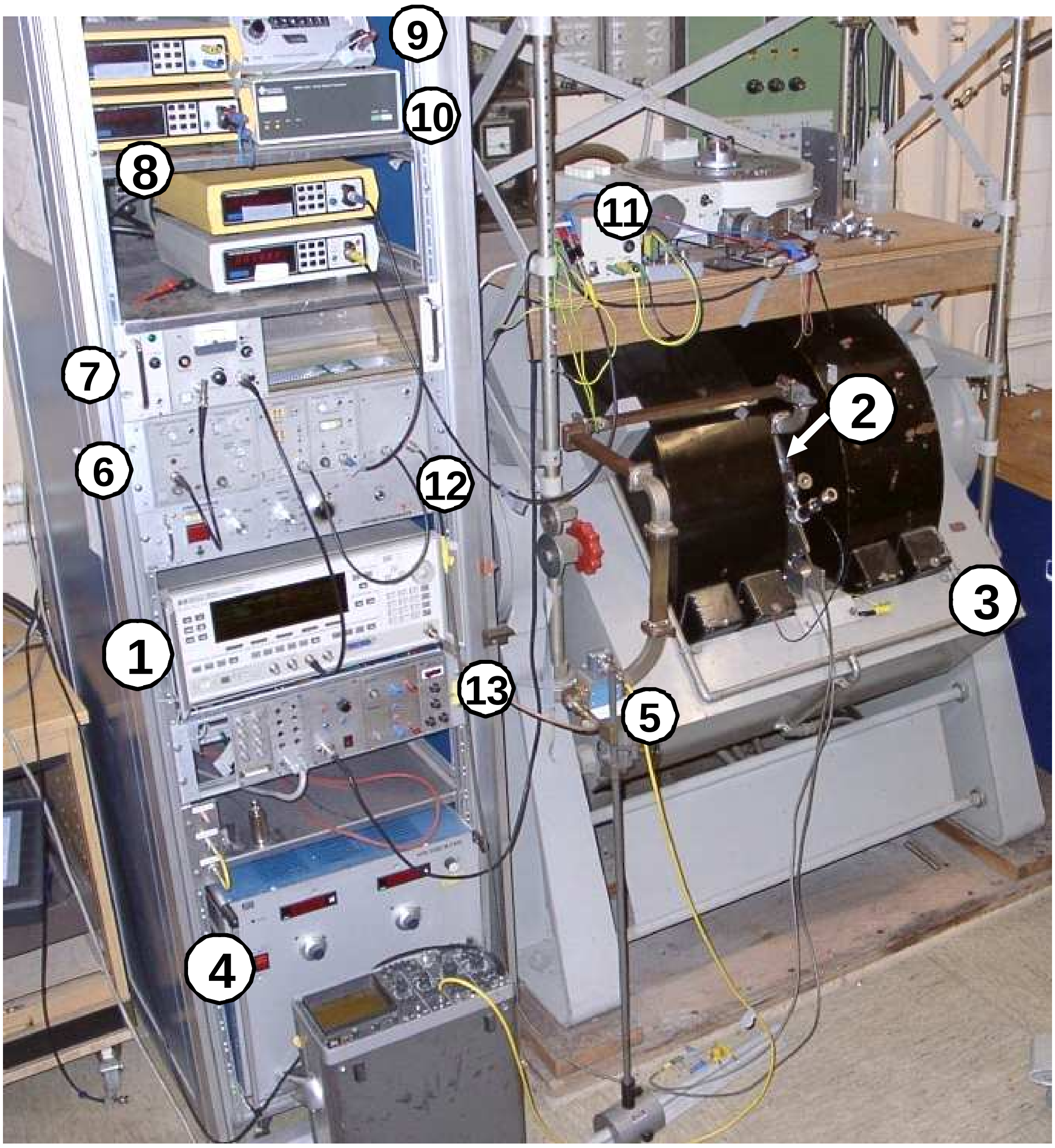

Figure 3.6: Microwave spectrometer: ① microwave synthesizer ② waveguide with resonant cavity (Varian) inside air gap of the magnet ③ Bruker EPR magnet ④ F.u.G. high voltage power supply ⑤ Ge-detector diode mounted to directional coupler ⑥ Lock-in amplifier ⑦ automatic frequency control (AFC) unit ⑧ Digital multimeters for reading absorption derivative $\mathrm{d}\chi''/\mathrm{d}H$, Hall probe voltage, temperatures, etc. ⑨ Hall probe high precision current source ⑩ DA converter for magnet power supply control ⑪ Goniometer table with step motor for angle dependent magnetic absorption measurements ⑫ electromechanical voltage ramp for magnet power supply control ⑬ I/O interface and manual adjustment of goniometer step motor.

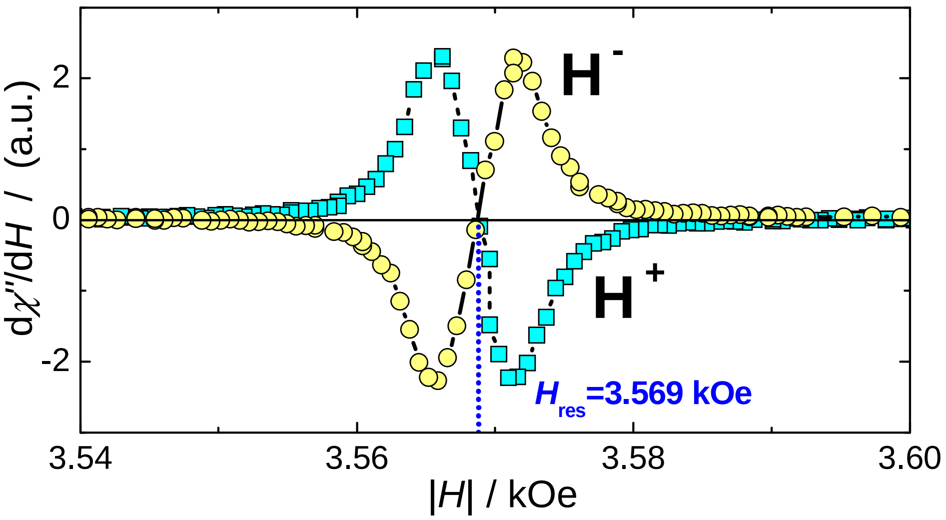

Figure 3.7: Magnetic field calibration of the microwave spectrometer using the resonance absorption of the g-marker DPPH at 9.1 Ghz.

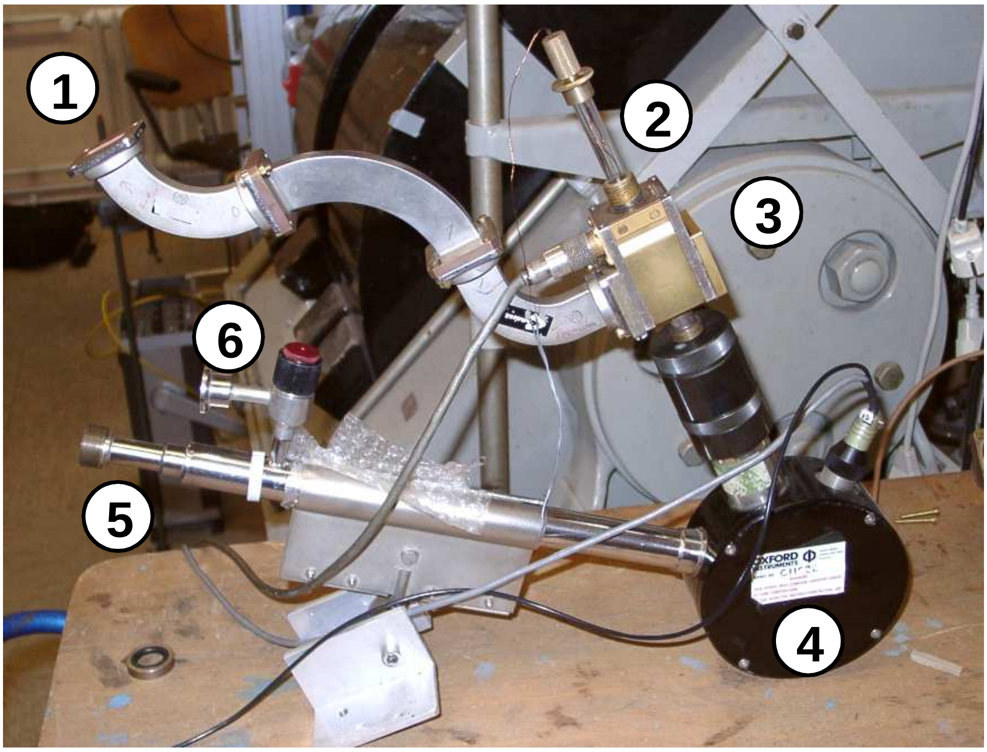

Figure 3.8: Varian resonant cavity with cryostat used for the temperature dependent X-band magnetic absorption experiments: ① waveguide ② evacuated double-walled quartz tube ③ multi-purpose resonant cavity (Varian) ④ cryostat (Oxford) with thermocouple and heating ⑤ He flow support and exhaust connector ⑥ cryostat vacuum valve.

Chapter 4

Structure and magnetism in $\mathrm{Fe}_x\mathrm{Pt}_{1-x}$ nanoparticles

This chapter presents the results of structural and magnetic characterization of $\mathrm{Fe}_x\mathrm{Pt}_{1-x}$ nanoparticles. First the main structural parameters like geometrical size, crystal structure, chemical order and Fe-Pt composition are determined from TEM and XRD measurements. Furthermore, the $\mathrm{Fe}_x\mathrm{Pt}_{1-x}$ composition is validated and refined by a composition-dependent Curie-temperature T_{C} extracted from ZFC magnetization measurements. Then, the two important parameters characterizing the magnetic behaviour of the nanoparticles, the anisotropy energy E_{A} (distribution) and the magnetic moment μ_{p}, are investigated.

4.1 Structural characterization of $\mathrm{Fe}_x\mathrm{Pt}_{1-x}$ nanoparticles

4.1.1 Shape, size distribution and next-neighbour distance of $\mathrm{Fe}_x\mathrm{Pt}_{1-x}$ nanoparticles

The TEM pictures depicted in Fig. 4.1 indicate the existence of spherical nanocrystaline $\mathrm{Fe}_x\mathrm{Pt}_{1-x}$ nanoparticles with rather narrow core size distribution of the particle diameter d. The tendency of the particles to self-organize becomes visible, at least for single layer formation after drying on the TEM grid. From the analysis of these TEM distribution histograms of crystal diame-

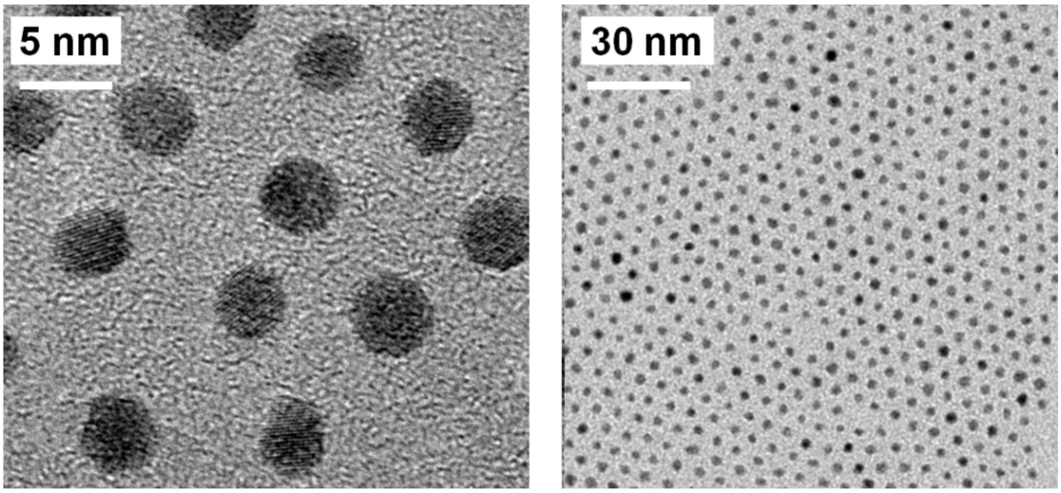

Figure 4.1: Typical TEM-pictures showing (left panel) the nanocrystallinity with visible atomic layers and spherical shape and (right panel) self-assembling of $\mathrm{Fe}_x\mathrm{Pt}_{1-x}$ nanoparticles on the TEM grid.

ters were generated and the mean next-neighbour distance N_{nn} was estimated. The histograms (Fig. 4.2) of diameters could be nicely fitted to a log-normal function $P(d) = (\sqrt{2\pi}\,\sigma d)^{-1}\exp(-\ln^2(d/\tilde{d})/(2\sigma^2))$, similar to Eq. 2.35 (see Sec. B), to obtain the median diameter $\tilde{d}$ and distribution width σ of the log-normal distribution.

The $\mathrm{Fe}_x\mathrm{Pt}_{1-x}$ samples A,C,D exhibit mean diameters $\bar{d}$ in the range $2.4\ldots4$ nm with a narrow distribution width of about $\sigma \approx 0.15$. It should be noted that, for these narrow size distributions, a symmetrical Gaussian distribution function would have been sufficient instead of the log-normal distribution. The mean next-neighbour distance D_{nn} for the $\mathrm{Fe}_x\mathrm{Pt}_{1-x}$ particles dried on the TEM grid was in the range $6\ldots12$ nm. This allows a rough estimation of minimum organic layer thickness of about $3\ldots6$ nm, disregarding the potential shrinking of the organic layer during drying on the TEM grid, or by the vaccuum required for the TEM measurements of the samples.

The parameters of the TEM analysis are summarized in Tab. 4.1 for the different samples investigated.

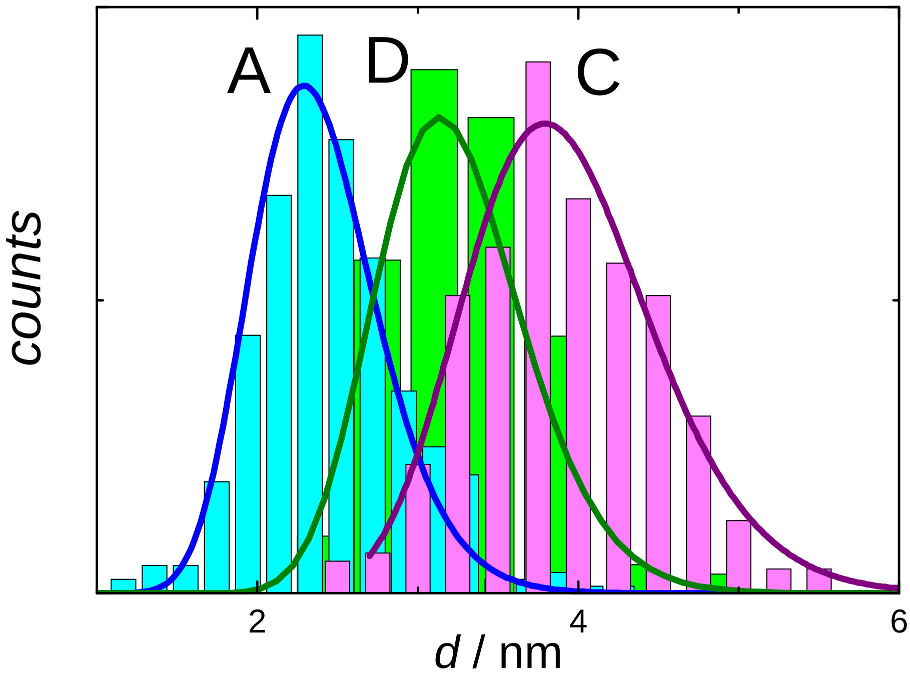

Figure 4.2: Distribution histograms for particle diameters in different Fe_xPt_{1-x} formulations derived from TEM-pictures as shown in Fig. 4.1. Solid curves represent corresponding fitted log-normal size distribution to obtain median diameter $\tilde{d}$ and width σ. The parameters are listed in Tab. 4.1.

4.1.2 Chemical order, size and composition of Fe_xPt_{1-x} nanoparticles

A typical wide range x-ray diffraction scan of sample C, see Tab. 4.1, is shown in Fig. 4.3. All spectra only reveal the presence of a chemically disordered crystalline fcc-phase A_1. No indication of the chemically ordered $L1_2$- or $L1_0$-phase could be detected, as evidenced by the lack of the superstructure peaks $(001), (110), (021), (112)$ marked by red lines in Fig. 4.3. Even after annealing of samples A, B, C no traces of ordered phases became visible in the XRD spectra. Furthermore, no formation of crystalline iron oxide phases, magnetite or maghemite, was observed indicating a good protection against oxidation by the organic oleic acid-oleyl amine capping of the particles. Nevertheless, the presence of a very thin iron oxide layer less than 0.4 nm, as reported for 4 nm ordered FePt nanoparticles [79], could not be excluded.

The position q_i and width Δq_i of the individual peaks have been determined

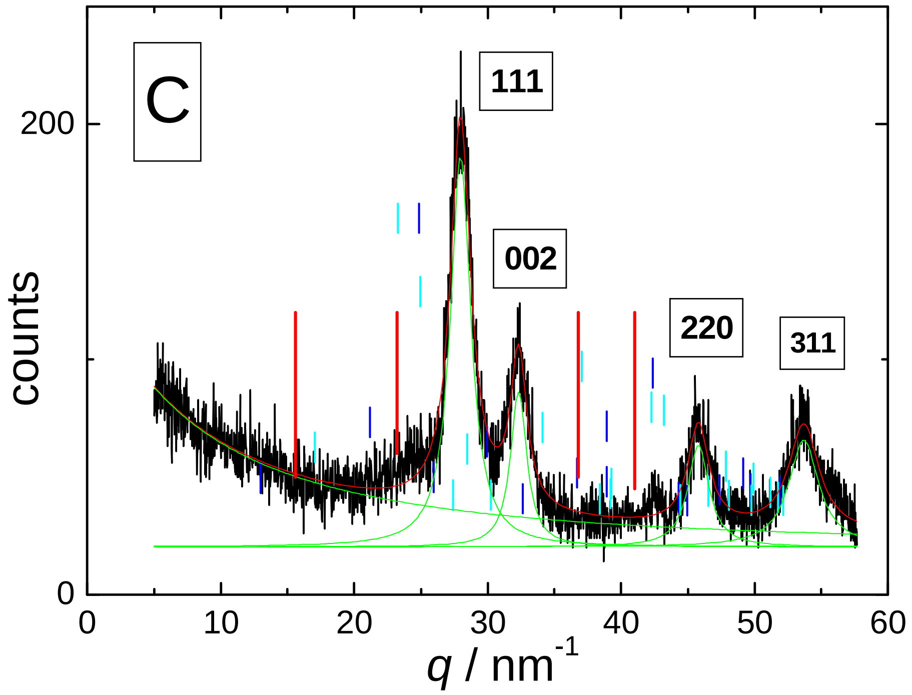

Figure 4.3: Wide-angle XRD scan of Fe_xPt_{1-x} nanoparticles (sample C). The red lines mark the position of super-structure peaks (ordered structure $L1_2$ or $L1_0$), peak positions of iron oxides are denoted by blue (magnetite, Fe_3O_4) and cyan (maghemite, $\gamma\!-\!Fe_2O_3$) lines.

from fitting the XRD scans to a sum of Lorentz-lines $\Sigma_i 2A_i\Delta q_i/(\pi(4(q-q_i)^2+\Delta q_i^2))$. The lattice constant a_0 was determined from the position of the peak with Miller index (hkl) using the Bragg equation[1] $q = 2\pi n/d_{\mathrm{hkl}}$ with $n = 1$, together with the lattice spacing $d_{\mathrm{hkl}} = a_0/(\sqrt{h^2+k^2+l^2})$ for cubic systems resulting in

$$a_0(h,k,l) = \frac{2\pi\sqrt{h^2+k^2+l^2}}{q}. \tag{4.1}$$

As shown in Fig. 4.4, all Fe_xPt_{1-x} samples possess a lattice constant at about 3.90 Å. A slight increase of lattice constant was observed after annealing, see Sec. 3.2.3, of samples A, B, and C.

Comparing a_0 with literature values for bulk, film and nanoparticles [80; 81; 82; 83], the Fe_xPt_{1-x} stoichiometries of the samples investigated have been estimated. They reflect a platinum-rich stoichiometry of the Fe_xPt_{1-x} nanocrys-

---

[1] Combining $n\lambda = 2d_{\mathrm{hkl}}\sin\theta$ with the wave vector definition $q = 4\pi\sin\theta/\lambda$)

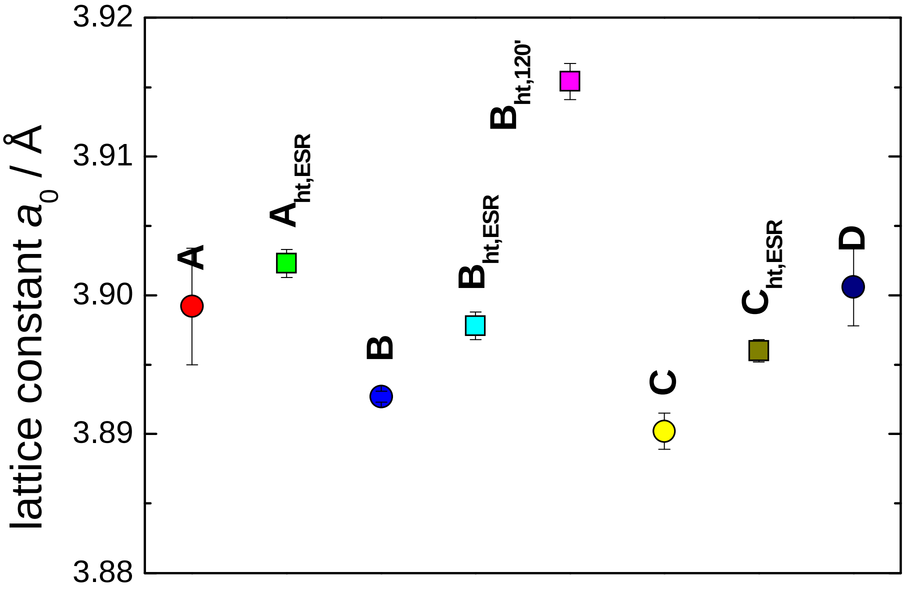

Figure 4.4: Overview of lattice constants a_0 determined from the main (111)-peak of the XRD scans of Fe_xPt_{1-x} samples. The preparation of the samples for XRD has been distinguished, samples dried directly from the batch solution are denoted by circles, while powder samples measured after annealing are depicted as squares.

tals with an iron amount x in the range 0.1 to 0.25 as shown in Fig. 4.5. This is in clear contrast to the intended equiatomic compostion $x = 0.5$ of the Fe_xPt_{1-x} nanoparticles by the chosen molar ratio of the Fe- and Pt-precursors for the preparation of the particles [76]. One reason for this deviation could be changes in the chemistry of the precursors during their storage.

The crystal core diameter was estimated from the width of the main (111)-peak using the Scherrer formula

$$d_{\mathrm{XRD}} = \frac{2\pi K_{\mathrm{hkl}}}{\Delta q_{111}}, \tag{4.2}$$

with shape factor K≈ 0.89 for index (111) and spherical crystallites. Figure 4.6 shows the mean diameter extracted from XRD for several Fe_xPt_{1-x} samples. Additionally, the diameter obtained by the analysis of the TEM pictures has been included. It can be seen that all Fe_xPt_{1-x} crystallites have a mean core diameter ranging from 3 nm to 5 nm. A small reduction of crystal size with annealing of the samples can be seen for sample B and C, which also has been reported for disordered FePt nanoparticles annealed at 970 K [84]. Where

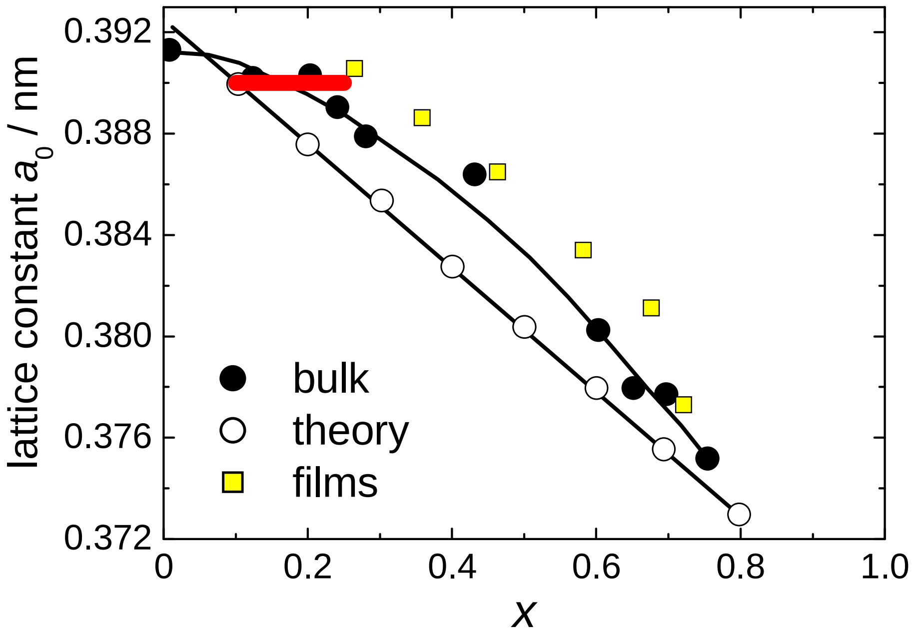

Figure 4.5: Relation between $\mathrm{Fe}_x\mathrm{Pt}_{1-x}$ stoichiometry and lattice constant a_0. Based on literature values for bulk, film and nanoparticle samples [80; 81; 82; 83], an Fe content x in the range $0.1 \ldots 0.25$ (red bar) is estimated for the $\mathrm{Fe}_x\mathrm{Pt}_{1-x}$ samples investigated in this work.

data is available, TEM and XRD reveal diameters in good accordance. No correlation of the core diameter d to the lattice constant a_0 was found.

The structural characterization by TEM and XRD yields the presence of chemically disordered spherical $\mathrm{Fe}_x\mathrm{Pt}_{1-x}$ nanocrystals with a mean core diameter d_p about 4 nm, and having a rather narrow size distribution. The composition of the platinum-rich nanoparticles from the lattice constant a_0 is found to be in the range $x = 0.1 \ldots 0.25$. An approach extracting the $\mathrm{Fe}_x\mathrm{Pt}_{1-x}$ composition based on their magnetic properties is presented in the following section.

4.2 Composition of $\mathrm{Fe}_x\mathrm{Pt}_{1-x}$ nano-particles extracted from ZFC measurements

An additional way to determine the composition of the $\mathrm{Fe}_x\mathrm{Pt}_{1-x}$ nanoparticles can be pursued by analysing the effective superparamagnetic Curie con-

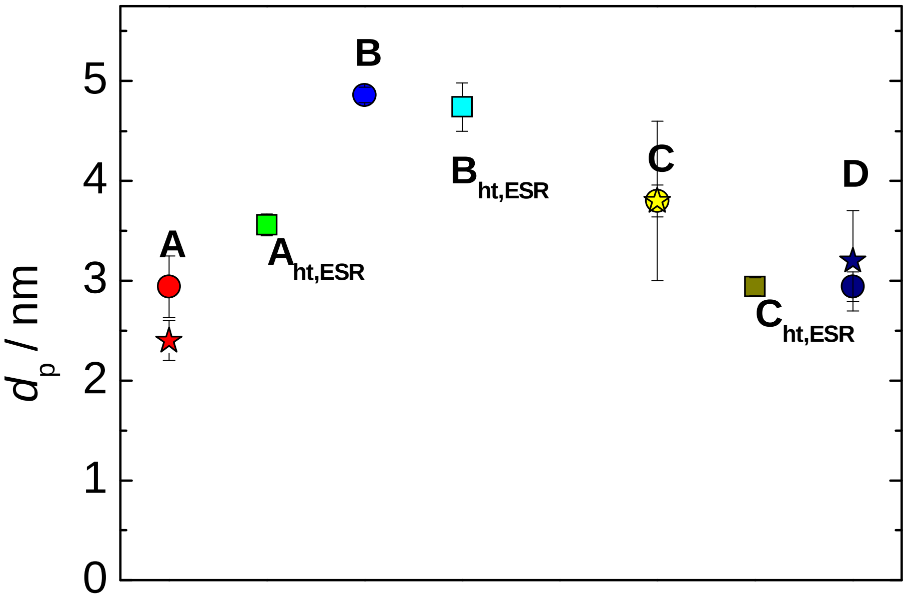

Figure 4.6: Mean core diameters Fe_xPt_{1-x} nanoparticles determined from the line-width of the (111)-peak of the XRD measurements.

stant $C(T)$ determined from ZFC-magnetization measurements. Mainly, a ZFC magnetization curve is a common way to visualize the transition from blocked to superparamagnetic behaviour for an ensemble of magnetic nanoparticles. As shown in Fig. 4.7, the main characteristic of the ZFC curves is the appearance of a maximum in the magnetization at different blocking temperatures T_b within the temperature range 10 K to 60 K for the Fe_xPt_{1-x} samples considered. From T_b a rough estimation of the effective anisotropy energy $E_A \approx 25\,k_BT_b$ is obtained, and an effective anisotropy energy $K_{eff} = 6E_A/(\pi d^3) \approx 10^{-4}$ J/m^3 was estimated, assuming a mean diameter d of 4 nm for all Fe_xPt_{1-x} particles.

The temperature behaviour of the superparamagnetic Curie constant $C = M/H \cdot T$ (above the blocking temperature) is displayed in Fig. 4.7. The observed linear decay of the Curie constant is to first order assigned to a temperature dependent magnetic moment $\mu(T)$ of the nanoparticle, $C(T) = N_p\mu_p^2(T)/(3V\mu_0k_B)$. This linear decay signals a mean-field behaviour of the particle moment, $\mu_p(T) = \mu_p(0)(1 - T/T_C)^{1/2}$, see Eq. 2.13 and by fitting this relation, the corresponding Curie temperatures T_C have been determined, as indicated by dashed lines in Fig. 4.7. As can be seen, the samples exhibit a

sample		XRD		TEM		
ID	batch/ state	a_0 Å	d_{XRD} nm	d_{TEM} nm	σ	D_{nn} nm
A	II/st	3.899(4)	2.9(3)	2.4(0)	0.16(1)	6.0(6)
$\mathrm{A}^{\mathrm{ESRht}}$	II/pwd	3.902(1)	3.6(1)			
B	II/st	3.8927(4)	4.86(8)			
$\mathrm{B}^{\mathrm{ESRht}}$	II/pwd	3.898(2)	4.7(2)			
$\mathrm{B}^{\mathrm{anneal}}$	II/pwd	3.915(2)	16(4)			
C	III/st	3.890(1)	3.8(2)	3.8(8)	0.15(2)	11.4(3)
$\mathrm{C}^{\mathrm{ESRht}}$	III/pwd	3.896(2)	2.9(1)			
D	IV/st	3.900(3)	2.9(2)	0.14(2)		6.9(9)

Table 4.1: Preparational and structural parameter of $\mathrm{Fe}_x\mathrm{Pt}_{1-x}$ nanoparticles obtained by TEM and XRD. Lattice constant a_0 and mean particle sizes d_{XRD}, d_{TEM} determined by XRD and TEM. Note, that only the annealed samples were the same as used in the magnetic investigations while for all other measurements individual samples were drawn from stock suspension.

quite large variation of Curie temperatures T_{C} ranging from about 150 K (E) to 850 K (C). Obviously, in sample C the magnetic phase with $T_{\mathrm{C}} \approx 850$ K obscures a phase with lower T_{C}, which can be identified by the upturning offshoot of $C(T)$ for $T > 325$ K. After subtracting a small temperature independent magnetization of about $M = 0.2$ Am^2/kg, a value $T_{\mathrm{C}} \approx 350$ K can be estimated, see Fig. 4.7 (right panel, grey triangles). This phase might correspond to the superparamgnetic phase with T_{b} at about 20 K.

To estimate the composition, several Curie temperatures have been collected from literature data of disordered $\mathrm{Fe}_x\mathrm{Pt}_{1-x}$ as depicted in Fig. 4.8 (left panel) and approximated by a 4th order polynomial, $T_{\mathrm{C}}(x) = \sum_{n=0}^{4} A_n x^n$ with $A_0 = 16(3), A_1 = 21.1(8), A_2 = -0.41(5), A_3 = 0.010(1), A_4 = 6.86(7) \cdot 10^{-4}$. Using the lower branch of the polynomial (platinum-rich composition), the iron content $x \equiv x$ Fe(at %) of the $\mathrm{Fe}_x\mathrm{Pt}_{1-x}$ samples was calculated from the corresponding T_{C} value.

The values reveal the presence of a platinum-rich $\mathrm{Fe}_x\mathrm{Pt}_{1-x}$ composition with x in the range $0.1 \ldots 0.25$ for the $\mathrm{Fe}_x\mathrm{Pt}_{1-x}$ samples as can be seen in Fig. 4.8 (right panel). For sample C the corrected value for $T_{\mathrm{C}} \approx 350$ K has been used

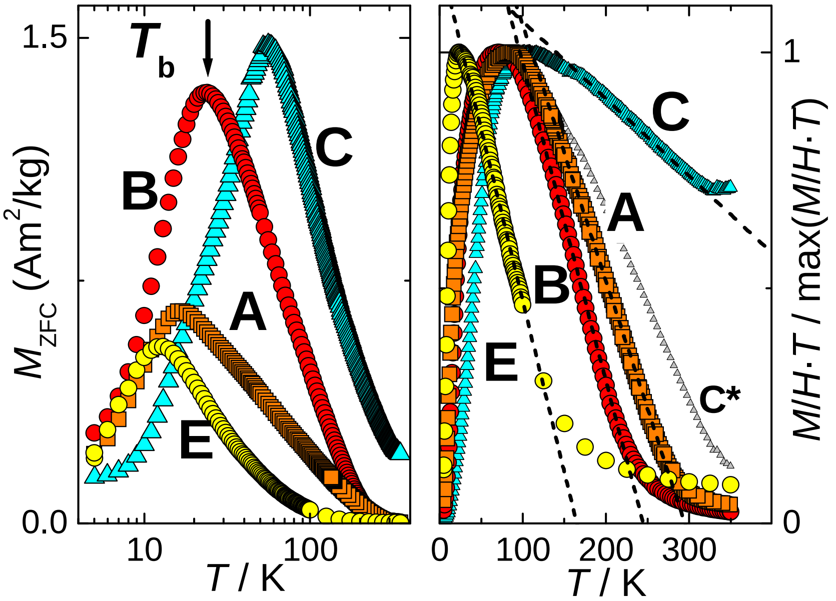

Figure 4.7: Left panel: ZFC-magnetization curves of Fe_xPt_{1-x} nanoparticles measured in $H = 0.1$ kOe. The characteristic temperature marked for sample B by the arrow, where the maximum of the ZFC-magnetization is reached, depicts the main blocking temperature T_b, roughly separating the region of blocked ferromagnetism, $T < T_b$, from superparamagnetism, $T > T_b$. Note the barely visible shoulder in the ZFC curve at about 20 K detected in sample C indicating the occurrence of at least two different magnetic phases. Right panel: Effective Curie constants $C = M/H \cdot T$ following from the ZFC-magnetization curves. For temperatures $T \gg T_b$ the Curie temperature T_C has been determined assuming a mean-field behaviour of the particle moments. Note, that the data have been normalized to $\max(M/H \cdot T)$ for graphical representation.

to determine x. Over this composition range, the relation between T_C and x may be approximated linearly. These results confirm and refine the values already extracted from the lattice constant a_0 in accordance with Sec. 4.1.2. The procedure to determine the composition x from T_C has the advantage that it is independent on the exact Fe_xPt_{1-x} amount in the sample, which was especially for the small sample amounts available in this study difficult to determine with high accuracy. On the other hand, the influence of chemical order on T_C has not been taken into account.

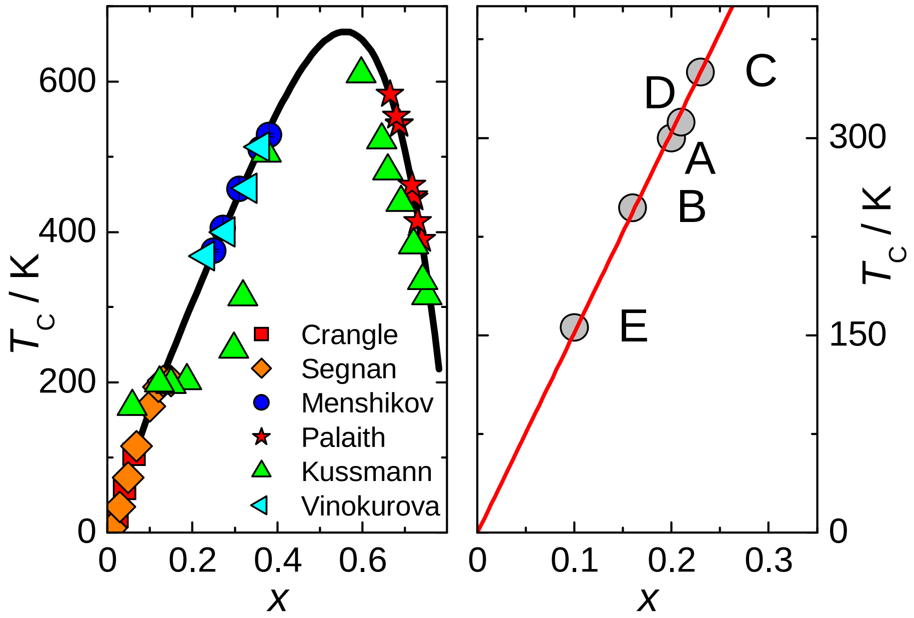

Figure 4.8: Left panel: Relation between Curie temperature T_C and iron content x compiled from literature data of disordered Fe_xPt_{1-x} bulk, thin film and nanoparticle samples: Crangle [51], Segnan [85], Menshikov [86], Palaith [63], Kussmann [46], Vinokurova [87]. Right panel: Composition x of Fe_xPt_{1-x} powder samples estimated from Curie temperature T_C determined by ZFC-magnetization measurements using the $T_C(x)$ relation compiled form literature data, which over this composition range can be linearly approximated by $T_C = 1550 \cdot x$ K as depicted by the red line.

4.3 Anisotropy energy barrier distribution of Fe_xPt_{1-x} nanoparticles

The energy barrier distribution of Fe_xPt_{1-x} nanoparticles is an important characteristics of magnetic nanoparticles to assess the internal magnetic structure. The blocking temperature T_b already allows for a rough estimation of the mean anisotropy energy E_A. In this section, two different ways to extract the underlying effective anisotropy distribution are presented and compared. Most common are the analysis of temperature-dependent ZFC- and AC-measurements in small magnetic fields, where the anisotropy energy E_A is dominating over the magnetic field energy $\mu_p H$.

Energy barrier distribution extracted from ZFC measurements

By taking the derivative of the effective Curie constant $\mathrm{d}(M(T)\cdot T/H)/\mathrm{d}T$, see Eq. 2.18, the anisotropy energy barrier distribution of the $\mathrm{Fe}_x\mathrm{Pt}_{1-x}$ samples may be obtained from a ZFC magnetization curve [22]. Some representative distribution curves of $\mathrm{Fe}_x\mathrm{Pt}_{1-x}$ nanoparticles are displayed in Fig. 4.9, where the relation Eq. 2.17 has been used to convert between measured temperature T and corresponding energy scale $E_{\mathrm{A}}(T) = T\ln(t_{\mathrm{m}}/\tau_0) \approx 27.6$, where typical values for measurement time $t_{\mathrm{m}} = 100$ s and prefactor $\tau_0 = 10^{-10}$ s have been employed.

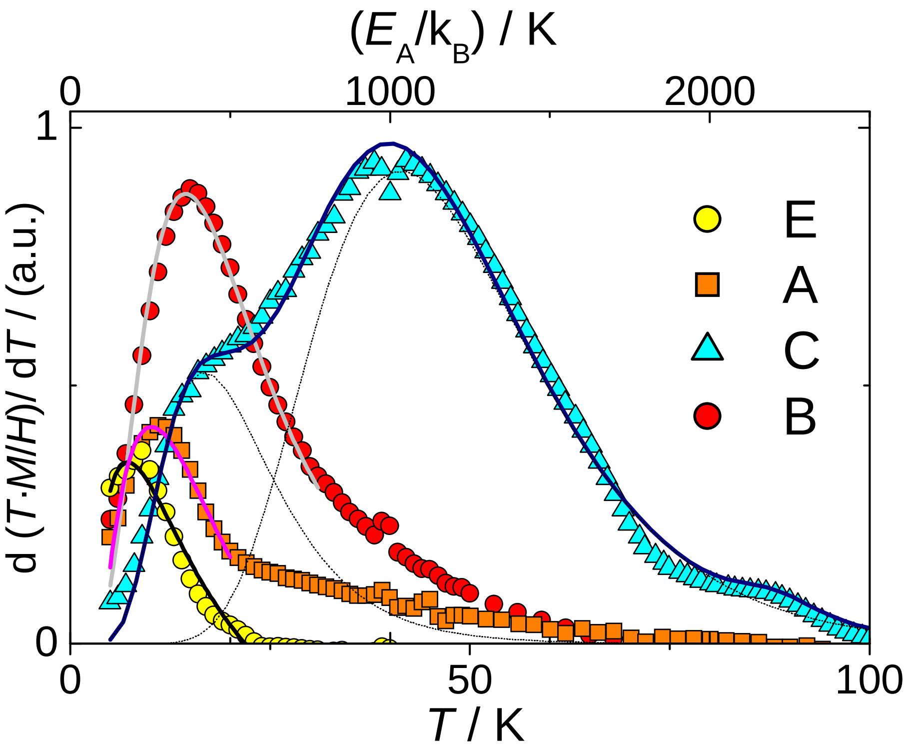

Figure 4.9: Anisotropy energy barrier distribution of $\mathrm{Fe}_x\mathrm{Pt}_{1-x}$ determined from the derivative of the effective Curie constant $\mathrm{d}(M(T)\cdot T/H)/\mathrm{d}T$ as measured in ZFC-measurements, see Fig. 4.7. All curves can be described by a single-peaked log-normal distribution except for sample C where at least three different maxima are visible indicating the presence of different magnetic $\mathrm{Fe}_x\mathrm{Pt}_{1-x}$ phases.

All samples show an asymmetric distribution of energy barriers with one distinct maximum at $E_{\mathrm{A}} \approx 200\ldots400$ K. Only in sample C are two additional maxima observed, the largest in amplitude at $E_\mathrm{A} = 1000$ K, and a rather small maximum at $E_\mathrm{A} = 2200$ K. A log-normal distribution of anisotropy energies could be nicely fitted to the curves to obtain mean anisotropy energy $\bar{E}_\mathrm{A}$ and distribution width σ. For sample C, two individual log-normal distributions have been utilized disregarding the smallest maximum located at $E_\mathrm{A} \approx 2200$ K. The corresponding values for the $\mathrm{Fe}_x\mathrm{Pt}_{1-x}$ nanoparticles are collected in Tab. 4.2.

The existence of two additional anisotropy contributions in sample C with higher energies suggests the presence of a mixture of different phases. The presence of a second phase with high anisotropy is supported by the high Curie temperature $T_\mathrm{C} \approx 850$ K drawn from the effective Curie constant of this sample, see Fig. 4.7.

Energy barrier distribution extracted from AC measurements

The imaginary part of the complex AC susceptibility is specific to the relaxational contribution of the magnetic nanoparticles only, and therefore not hampered by any contributions from paramagnetic or blocked ferromagnetic fraction within the $\mathrm{Fe}_x\mathrm{Pt}_{1-x}$ samples. A typical set of AC-magnetization curves of $\mathrm{Fe}_x\mathrm{Pt}_{1-x}$ nanoparticles is shown in Fig.4.10 for sample E, where at five different excitation frequencies $\omega/(2\pi)$, the temperature dependent real and imaginary parts of the susceptibility ($H_\mathrm{AC} = 2$ Oe) have been recorded. The real parts $\chi'(T,\omega)$ show rather broad maxima just above the ZFC blocking temperature T_b which are shifting with increasing frequency towards higher temperatures. At the same time, the amplitude of the curves are fairly decreasing with increasing frequency. The static ZFC-magnetization curve (dotted black line in the figure) can be considered as a χ'-magnetization recorded at a frequency $1/t_\mathrm{m} = 0.01$ Hz and accordingly exhibits the maximum at the lowest temperature.

The imaginary parts $\chi''(T,\omega)$ have a narrower shape with their maxima at temperatures $T_\mathrm{max}(\omega)$ (marked by arrows in the figure) close to the inflection point of the corresponding $\chi'(T,\omega)$ curve. Also the maximum temperatures $T_\mathrm{max}(\omega)$ are shifting with increasing frequency, while the amplitudes of the curves mainly remain constant.

A straightforward way to extract the mean anisotropy energy is gained by

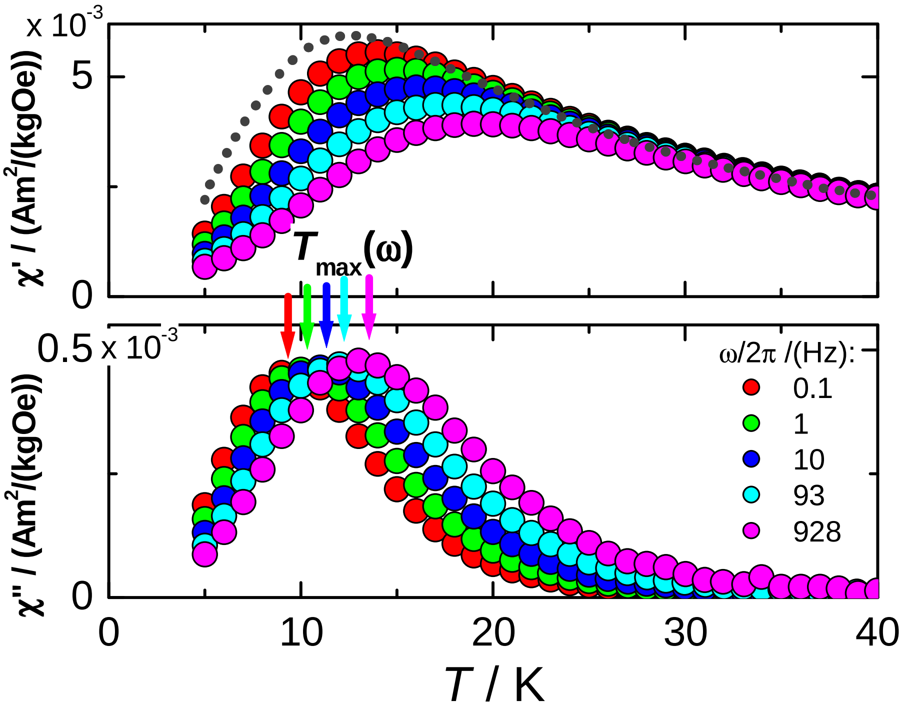

Figure 4.10: Temperature-dependent complex AC-susceptibility $\chi(T,\omega)$ of $\mathrm{Fe}_x\mathrm{Pt}_{1-x}$ nanoparticles sample E measured at five fixed frequencies at a driving amplitude of $H_{\mathrm{AC}} = 2$ Oe. Top panel: Real part $\chi'(T;\omega)$ of the AC-susceptibility (coloured symbols) together with the static ZFC-susceptibility (grey dotted line, see Fig. 4.7). Bottom panel: Imaginary parts $\chi''(T,\omega)$. The arrows mark the temperature $T_{\max}$ at which the maximum of the imaginary part $\max(\chi''(\omega,T_{\max}))$ is reached for the individual frequencies. These temperatures $T_{\max}$ are used for the Arrhenius analysis, as shown in Fig. 4.11.

Arrhenius plots of $\omega/(2\pi)$ versus the inverse of $T_{\max}(\omega)$, as shown in the inset of Fig. 4.11. Then, by fitting of Eq. 2.23 to the data, the mean anisotropy barrier energy $E_{\mathrm{A,m}}$ and the relaxational pre-factor τ_0 have been determined for the $\mathrm{Fe}_x\mathrm{Pt}_{1-x}$ nanoparticles. The resulting mean anisotropy energies show good agreement with the energies determined from ZFC-measurements. Obviously, the values of $\tau_0 = 10^{-14} \ldots 10^{-18}$ s are found to be much smaller than the commonly stated 10^{-9} s to 10^{-12} s for magnetic nanoparticles. Furthermore, τ_0 seems to be correlated to $E_{\mathrm{A,m}}$ for the $\mathrm{Fe}_x\mathrm{Pt}_{1-x}$ nanoparticles, as can be seen in Fig. 4.11. From the analytical expression of the prefactor Eq. 2.16 a τ_0 should decrease to first order like $E_{\mathrm{A}}^{-3/2}$ (dotted grey line), while a much stronger

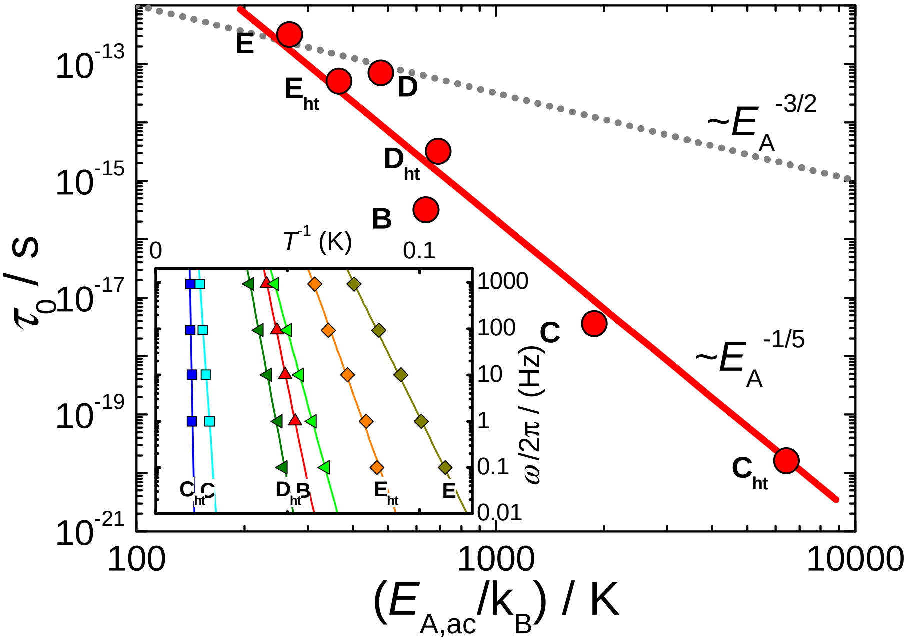

Figure 4.11: Relation between relaxation prefactor τ_0 and anisotropy energy $E_{\mathrm{A,AC}}$ in $\mathrm{Fe}_x\mathrm{Pt}_{1-x}$ nanoparticles obtained by Arrhenius analysis of AC measurements. The red line reflects a $\tau_0 \sim E_{\mathrm{A}}^{-1/5}$ dependence describing the experimental data while the dotted grey line is a expected $\tau_0 \sim E_{\mathrm{A}}^{-3/2}$ relation according to Eq. 2.16. The inset shows Arrhenius plots of the AC-excitation frequency $\omega/2\pi$ versus inverse of maximum temperature $T_{\max}$ of the imaginary susceptibility $\chi''(T)$. The straight lines are fits providing mean energy barrier $E_{\mathrm{A,m}}$ and apparent relaxation prefactor τ_0.

descrease proportional $E_{\mathrm{A}}^{-1/5}$ (straight red line) is found experimentally for the $\mathrm{Fe}_x\mathrm{Pt}_{1-x}$ nanoparticles.

More information about the anisotropy present in $\mathrm{Fe}_x\mathrm{Pt}_{1-x}$ nanoparticles barrier, including the distribution of energy barriers may be achieved by plotting the $\chi''(T,\omega)$ curves versus scaled temperatures $-T\ln(\omega\tau_0)$, for which the curves fuse into a single curve reflecting the energy barrier distribution $E_A/\mathrm{k_B}$, as shown in Fig. 4.12 for $\mathrm{Fe}_x\mathrm{Pt}_{1-x}$ sample E. Here again, all samples show an asymmetric distribution of anisotropy energies with one single maximum, while in sample C, a second distinct maximum is visible. Similarly, by fitting a log-normal function, the mean $\bar{E}_{\mathrm{A}}$ and width σ of the anisotropy energy distribution, together with the scaling factor τ_0 were obtained. The parameters are included in Tab. 4.2.

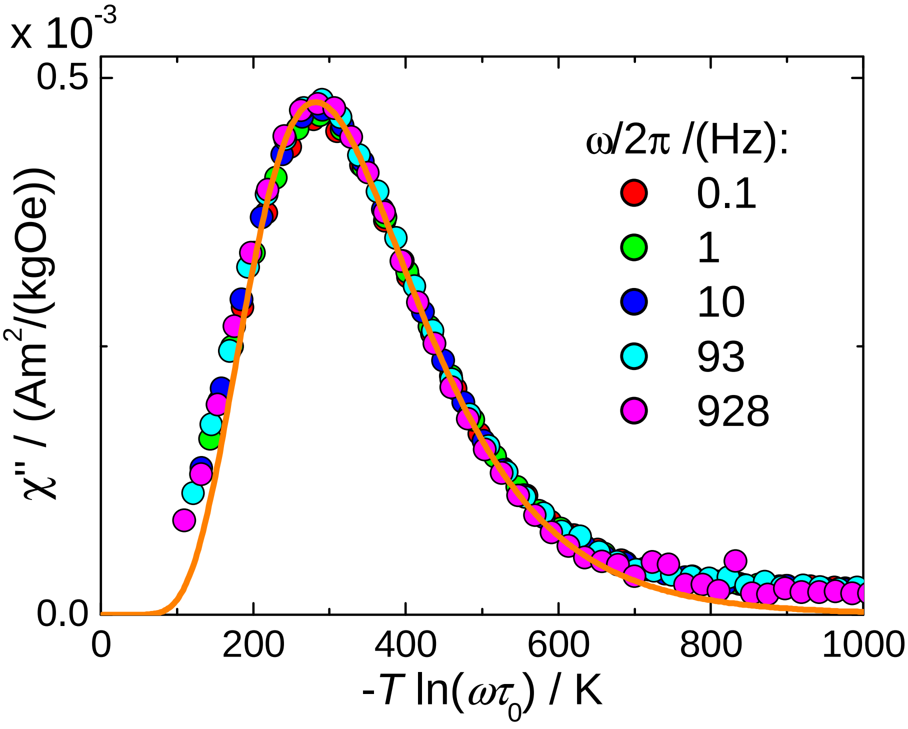

Figure 4.12: Energy barrier distribution of $\mathrm{Fe}_x\mathrm{Pt}_{1-x}$ nanoparticles (sample E) extracted from the temperature dependent imaginary part $\chi''(T)$ of the AC-susceptibility plotted versus scaled temperature $-T\ln(\omega\tau_0)$ with $\tau_0 = 1.6 \cdot 10^{-13}$ s , as shown in Fig. 4.10. By fitting a log-normal distribution (orange straight line) median and width of the energy barrier distribution are obtained.

Obviously, the mean anisotropy energy can be reliably determined from the Arrhenius plots in excellent agreement with the values following from $\chi''(T,\omega)$. The same width $\sigma \approx 0.4$ of the energy distribution is found for most samples, and this for both measurement techniques, ZFC- and AC measurements. Deviations are present for the value of the mean anisotropy energy, where the energy from ZFC-measurement is in most cases less than the value from the corresponding AC-measurement.

The corresponding effective anisotropy constants $K_{\mathrm{eff}} = E_{\mathrm{A}}/V$ of the nanoparticles have been estimated from the mean anisotropy barrier energy and the mean particle volume $V = \pi/6\bar{d}_{\mathrm{p}}$. The resulting K_{eff} in the range $1 \cdot 10^4 \ldots 5 \cdot 10^4$ J/m^3 are found to be one order of magnitude smaller than in ordered FePt particles, where values up to 10^6 J/m^3 have been reported [71].

ID		ZFC		AC		$M(H)$
		$M_{\mathrm{ZFC}}(T)$	$\mathrm{d}C(T)/\mathrm{d}T$	Arrhen.	$\chi''(T(\omega))$	
	$T_{\mathrm{C}}(K)$	$E_{\mathrm{A}}(\mathrm{K})$	$\bar{E}_{\mathrm{A}}(\mathrm{K})$	$\bar{E}_{\mathrm{A}}$ (K)	$\bar{E}_{\mathrm{A}}$ (K)/σ	$M_{\mathrm{S}}(\frac{\mathrm{Am}^2}{\mathrm{kg}})$
	x	$T_{\mathrm{b}}(\mathrm{K})$	σ	τ_0 (s)	τ_0(s) /$C_0(\frac{\mathrm{Am}^2}{\mathrm{kgT}})$	B ($\mathrm{K}^{-3/2}$)
A	300	470	545			7.2
	0.2	17	0.49			$3.7 \cdot 10^{-4}$
B	247	663	580	640	580 / 0.41	11.2
	0.16	24	0.45	$3 \cdot 10^{-16}$	$3 \cdot 10^{-15}$ / 7.1	$2.4 \cdot 10^{-4}$
C	350	553	598		780 / 0.39	12.9
	~0.23	20	0.4		$6 \cdot 10^{-18}$ / 3.7	$1.3 \cdot 10^{-4}$
		1418	1347	1878	1890 / 0.35	
		56	0.3	$4 \cdot 10^{-18}$	$6 \cdot 10^{-18}$ / 6.4	
D	312	553	380	479	480 / 0.37	7.4
	0.21	20	0.42	$7 \cdot 10^{-14}$	$5 \cdot 10^{-14}$ / 4.4	$2.7 \cdot 10^{-4}$
E	156	359	420	318	292 / 0.39	4.9
	0.1	13	0.39	$1 \cdot 10^{-14}$	$3 \cdot 10^{-14}$/ 4.7	$6.2 \cdot 10^{-4}$

Table 4.2: Anisotropy energies E_{A} of $\mathrm{Fe}_x\mathrm{Pt}_{1-x}$ nanoparticles extracted from ZFC-measurements, either from blocking temperature T_{b} or $\mathrm{d}C(T)/\mathrm{d}T$ representation, and from AC-measurements, applying Arrhenius plots or log-normal fits to $\chi''(T(\omega))$ magnetization curves. Note, all energies are given in units of K, but the factor $\mathrm{k}_{\mathrm{B}}^{-1}$ with E_{A} has been suppressed to save space in the column names.

4.4 $\mathrm{Fe}_x\mathrm{Pt}_{1-x}$ nanoparticles at large magnetic fields H=10 kOe

4.4.1 The magnetic moment of $\mathrm{Fe}_x\mathrm{Pt}_{1-x}$ nanoparticles

At large magnetic fields H, the influence of the magnetocrystalline anisotropy on the magnetic behaviour of magnetic nanoparticles becomes negligible, since then $\mu_{\mathrm{p}}H \gg E_{\mathrm{A}}$. Therefore, temperature dependent measurements of the magnetization of $\mathrm{Fe}_x\mathrm{Pt}_{1-x}$ nanoparticles at $H = 10$ kOe were performed to analyse the behaviour of the saturation magnetization $M_{\mathrm{S}}(T = 0)$ or the mean particle moment $\mu_{\mathrm{p}} = M_{\mathrm{S}}V$, as displayed in Fig. 4.13. The magnetization at $H = 10$ kOe is strongly diminishing with increasing temperature, which is attributed to a temperature dependence of the nanoparticle's magnet moment $\mu_\mathrm{p}(T)$. At low temperatures, this behaviour may be adequately described using Bloch's law Eq. 2.12 with $\beta = 3/2$ as for bulk systems. The resulting Bloch coefficients about 10^{-4} K$^{-3/2}$ for the Fe$_x$Pt$_{1-x}$ nanoparticle samples turned out to be much larger than the bulk value [17], $3 \cdot 10^{-6}$ K$^{-3/2}$. Similar large values were also found on Fe nanocrystals [88; 17] and confirmed by Monte Carlo simulations [89]. The Bloch coefficient B is decreasing with the saturation magnetization $M_\mathrm{S}(T = 0)$ as can be seen in the right panel of Fig. 4.13.

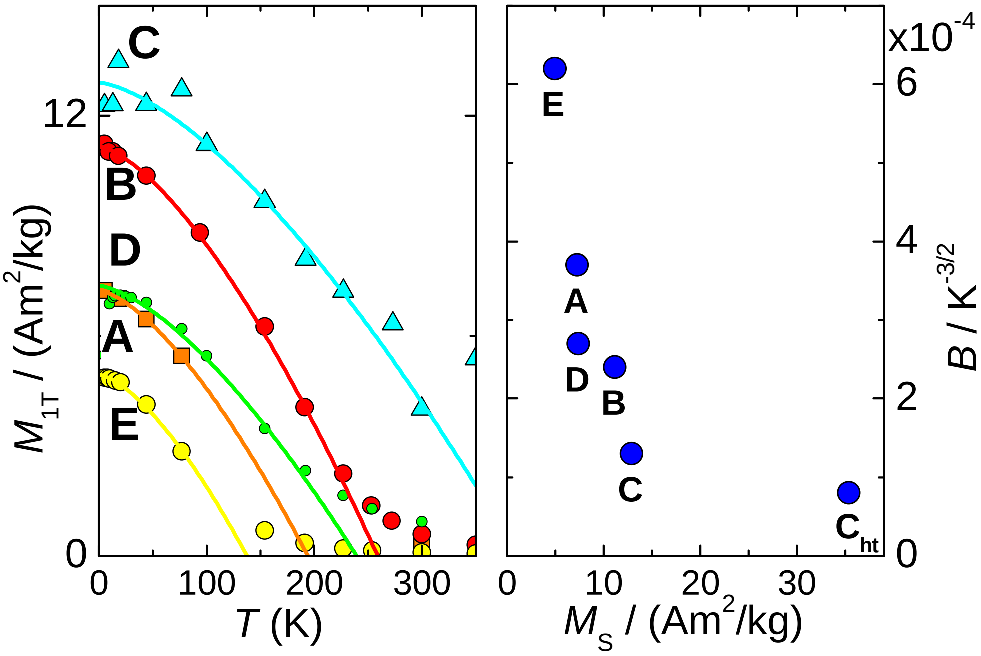

Figure 4.13: Left: Temperature dependent magnetization M_S of Fe$_x$Pt$_{1-x}$ nanoparticles measured at $H = 10$ kOe . The straight lines are fits using Bloch's law, Eq. 2.12, to describe the low temperature behaviour of the particle moment $\mu_\mathrm{p}(T)$. Right: Resulting Bloch coefficient B versus saturation magnetization $M_\mathrm{S}(T = 0)$.

In a same manner, the mean anisotropy energy $\bar{E}_\mathrm{A}$ determined from the AC-measurements of the Fe$_x$Pt$_{1-x}$ nanoparticles appears to be related to the saturation magnetization $M_\mathrm{S}(T = 0)$, as displayed in Fig. 4.14. This behaviour can be roughly approximated by $E_\mathrm{A,m}$ [K]$\approx 61 \cdot M_\mathrm{S}(T = 0)$ [Am^2/kg], as shown by the dotted grey line of the figure.

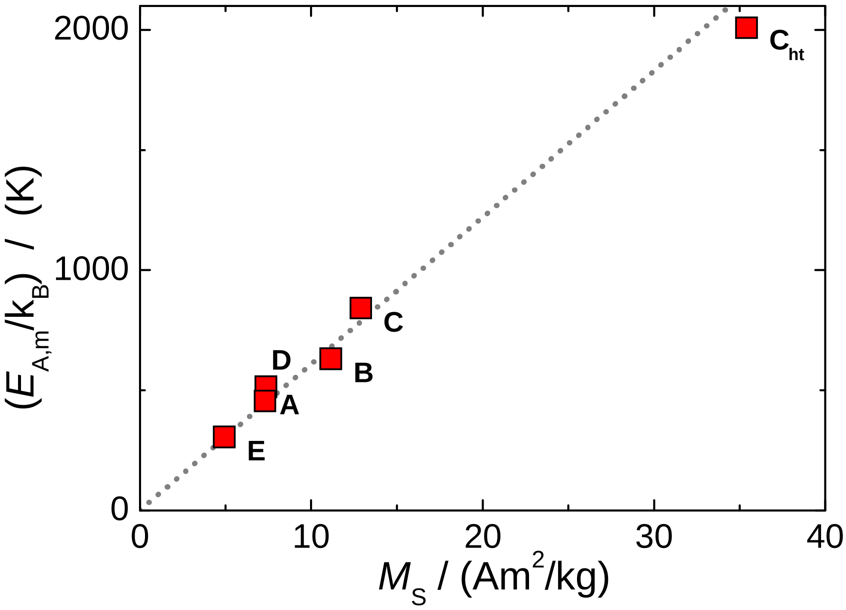

Figure 4.14: Mean anisotropy energy $E_{\mathrm{A,m}}$ determined from AC-measurements versus saturation magnetization M_{S} obtained from high field magnetization measurements. The dotted grey line reflects the linear approximation $E_{\mathrm{A,m}}$ [K]$\approx 61 \cdot M_{\mathrm{S}}$ [Am^2/kg].

From the relation $E_{\mathrm{A}} = K_{\mathrm{eff}}V$, such strong variation of the anisotropy E_{A} would not have been expected for $\mathrm{Fe}_x\mathrm{Pt}_{1-x}$ nanoparticles all having a diameter close to 4 nm, and thus the same volume. Likewise, a considerable variation of the anisotropy constant K over this narrow composition range seems not to be plausible. Therefore, it is not the geometrical size, but also the magnetic order induced by the chemical order, that determines both particle moment μ_{p} (and thereby saturation magnetization $M_{\mathrm{S}}(0) = \mu_{\mathrm{p}}(0)/V$) and anisotropy energy E_{A}. Therefore, it is inferred that the representation $E_{\mathrm{A}}(M_{\mathrm{S}}(0))$ is a suitable indicator of magnetic and chemical order of the $\mathrm{Fe}_x\mathrm{Pt}_{1-x}$ nanoparticles.

4.4.2 The regime of isotropic superparamagnetism

As already observed in the analysis of the ZFC-magnetization in Sec. 4.2, the magnetic moments of the $\mathrm{Fe}_x\mathrm{Pt}_{1-x}$ nanoparticles exhibit a pronounced temperature dependence $\mu_\mathrm{p} = \mu_\mathrm{p}(T)$. Accordingly, this also is apparent in the magnetization isotherms $M(H)$, where a rescaling as $M(H/T)$ is not sufficient to bring the magnetization curves $M(H)$ measured at different temperatures T onto one single curve, as expected from Eq. 2.34. An example for sample B is shown in the left panel of Fig. 4.15. Hence, incorporating a temperature dependence $q(T)$ as a free parameter for rescaling the x-axis, the resulting $M(q(T) \cdot H/T)$ curves could be brought onto one single curve as shown in the right panel of Fig. 4.15. For the other $\mathrm{Fe}_x\mathrm{Pt}_{1-x}$ samples, single curves of similar quality with different $q(T)$-behaviour could be achieved. The remaining splitting of the curves at high magnetic fields was attributed to parasitic paramagnetic and diamagnetic background susceptibilities.

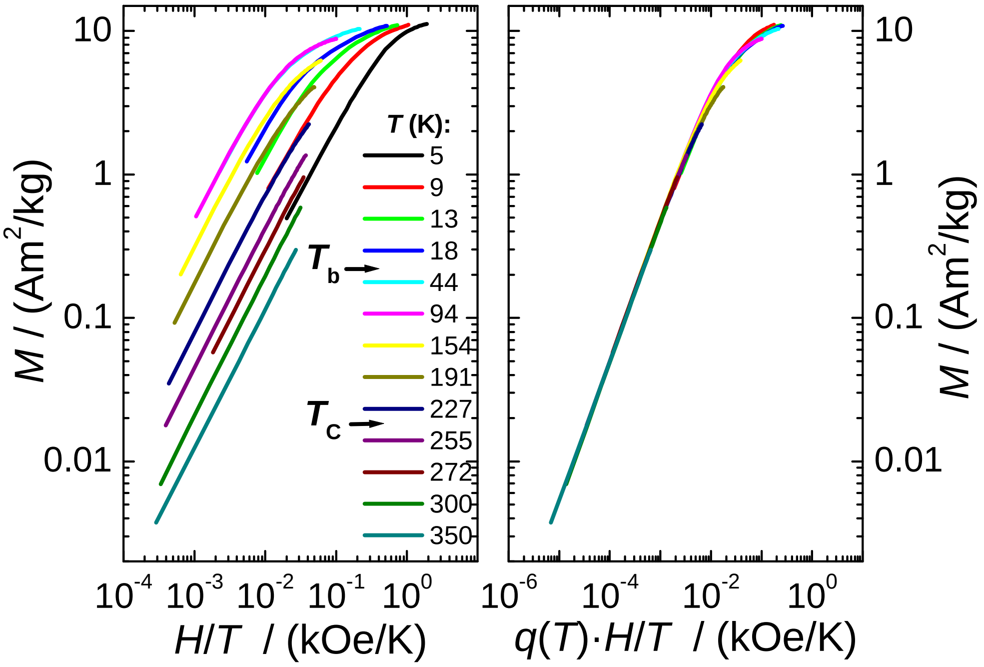

Figure 4.15: Left panel: Magnetization isotherms M as a function of H/T of $\mathrm{Fe}_x\mathrm{Pt}_{1-x}$ nanoparticles (sample B). According to Eq. 2.36 the data should collapse onto one single curve. But clear deviations occur due to the strong temperature dependence of the moment $\mu_\mathrm{p}(T)$. The values of blocking, $T_\mathrm{b} = 24$ K, and Curie temperature, $T_\mathrm{C} = 247$ K have been added to the temperature legend. Right panel: Single curve of magnetization isotherms after rescaling to $M(q(T) \cdot H/T)$ assuming a temperature-dependent moment $\mu_\mathrm{p}(T) = \mu_\mathrm{p}(0)q(T)$.

The resulting normalized temperature dependence $q(T)$ of the magnetic moment is shown on Fiq. 4.16 (coloured symbols), together with the corresponding normalized effective Curie constant as a function of temperature (straight lines) for these samples obtained from ZFC-measurements, see Fig. 4.7.

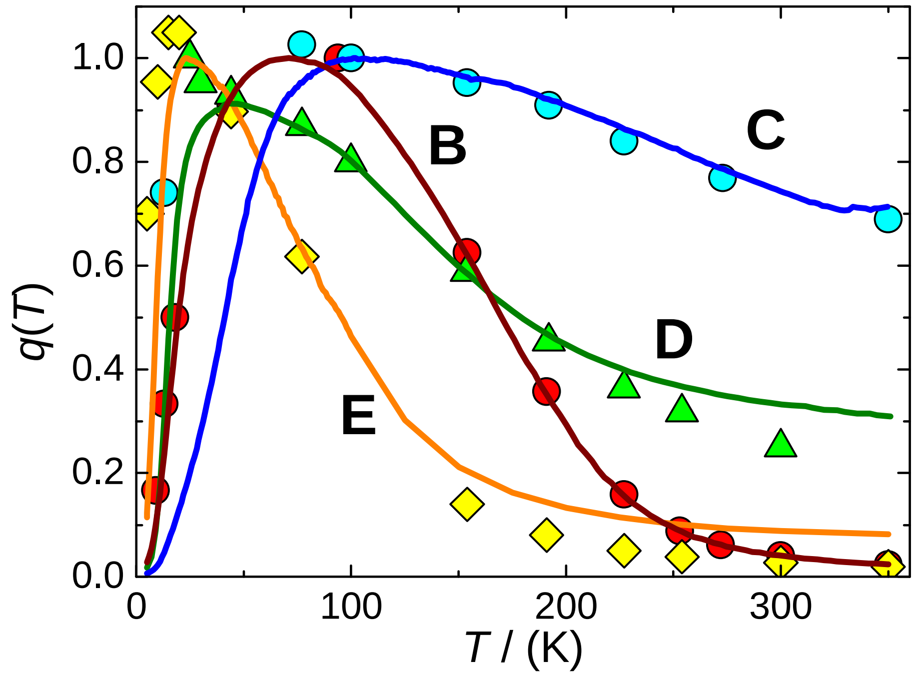

Figure 4.16: Normalized temperature dependent decrease (symbols) of the magnetic moment $q(T) \approx \mu_\mathrm{p}(T)/\mu_\mathrm{p}(T_\mathrm{b})$ obtained by rescaling of the magnetization isotherms, as displayed in Fig. 4.15. The $\mathrm{Fe}_x\mathrm{Pt}_{1-x}$ nanoparticle samples show the same temperature behaviour for $T > T_\mathrm{b}$ as the effective Curie constant extracted from the corresponding ZFC-magnetization (straight lines), see Fig. 4.7.

Clearly, the same temperature behaviour for $T > T_\mathrm{b}$ of the magnetic moment $\mu_\mathrm{p}(T)$ is extracted from magnetization isotherms $M(H)$ measured in magnetic fields up to 10 kOe as well as from ZFC-magnetization which were measured in a small magnetic field of 0.1 kOe. In this regime well above T_b, the magnetic behaviour of the $\mathrm{Fe}_x\mathrm{Pt}_{1-x}$ nanoparticles seems to be dominated by a thermal induced decrease of the coupling (caused by exchange interaction) of the individual atomic moments within each nanoparticle, and not strongly influenced by anisotropy effects.

Finally, to determine the magnetic moment $\mu_\mathrm{p}(0)$ extrapolated to $T = 0$ K, the magnetic moment was determined from a magnetization isotherm $M(H)$ measured at a temperature T slightly above the blocking temperature T_{b}. Therefore, the Langevin-function with a log-normal distribution of moments Eq. 2.36 was used as a model.

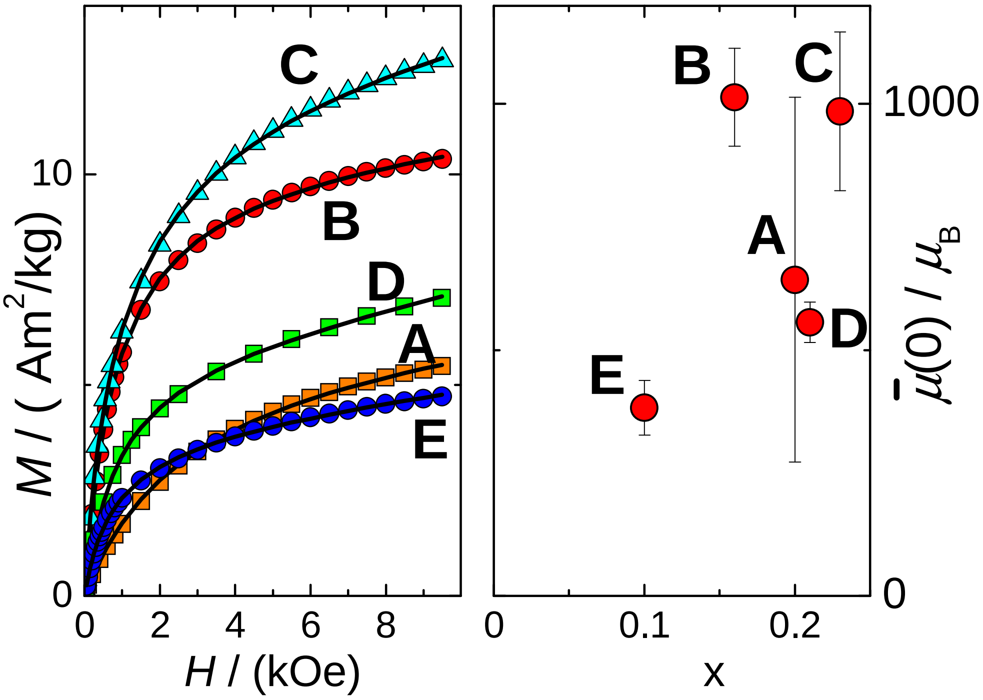

Figure 4.17: Left panel: Magnetization isotherms $M(H)$ (coloured symbols) of $\mathrm{Fe}_x\mathrm{Pt}_{1-x}$ nanoparticles measured at T_m slight above T_{b} (25 K for sample E and D; 44 K for B, 77 K for A and C). The lines are fits using the Eq. 2.36 to obtain mean $\bar{\mu}$ and width σ of a log-normal magnetic moment distribution. Right panel: Mean particle moment $\bar{\mu}(0)$ extracted from $M(H)$ data versus composition of $\mathrm{Fe}_x\mathrm{Pt}_{1-x}$ nanoparticles.

The resulting fits (straight lines) and the $M(H)$ magnetization isotherms for the $\mathrm{Fe}_x\mathrm{Pt}_{1-x}$ samples are displayed in the left panel of Fig. 4.17. The parameters of the fits are collected in Tab. 4.3. Based on the observed Bloch-behaviour of the temperature dependent magnetization $M(T)$ measured at $H = 10$ kOe, see Fig. 4.13, a mean magnetic moment $\bar{\mu}(T = 0)$ was extrapolated from the fitted $\mu_{\mathrm{p}}(T_m)$ by inverting the Bloch relation Eq. 2.12, $\bar{\mu}(0) = \bar{\mu}(T)/(1 - BT_m^{3/2})$, where the individual values for Bloch coefficient B and temperature T_m at which the magnetization isotherm was measured have been utilized.

ID	$\bar{\mu}(0)$	$\mu_\mathrm{p}(T_\mathrm{m})$	σ	T_m	χ_bgd	B
	μ_B	μ_B		K	$\mathrm{Am}^2/(\mathrm{kg}\cdot\mathrm{kOe})$	10^{-4} $\mathrm{K}^{-2/3}$
A	642(370)	307(177)	1.0(2)	77	3(2)	3.70(6)
B	1014(99)	623(61)	0.91(4)	44	4.6(6)	2.40(2)
C	985(161)	427(70)	1.22(4)	77	7.8(9)	1.31(1)
D	556(41)	365(27)	0.88(2)	25	8.9(3)	2.72(8)
E	382(56)	206(39)	1.06(5)	20	5.2(3)	6.20(2)

Table 4.3: Mean magnetic moment $\bar{\mu}(0)$ determined from fits using Eq. 2.36 to magnetization isotherms $M(H)$ of $\mathrm{Fe}_x\mathrm{Pt}_{1-x}$ nanoparticles measured at T_m. The quoted Bloch coefficient was extracted from $M(T, H = 10$ kOe$)$ for extrapolation of $\mu_\mathrm{p}(T_\mathrm{m})$ to $\bar{\mu}(0)$ at $T = 0$ K.

As can be seen from Fig. 4.17, resulting mean magnetic moments $\bar{\mu}(0)$ in the range 400 to 1000 μ_B are found for the $\mathrm{Fe}_x\mathrm{Pt}_{1-x}$ nanoparticle samples, and there seems to be only a weak correlation with composition x. Generally, the particle moment is increasing with increasing content of iron in the nanoparticles, yet the chemical order in the particles has some impact on the resulting magnetic moment $\bar{\mu}(0)$.

Chapter 5

Spin dynamics of $\mathrm{Fe}_x\mathrm{Pt}_{1-x}$ nanoparticles at microwave frequencies

This chapter analyses the dynamic magnetic behaviour of $\mathrm{Fe}_x\mathrm{Pt}_{1-x}$ nanoparticles probed by magnetic resonance spectroscopy at microwave frequencies. This comprises the determination of the g-factor at room temperature in the isotropic range, where anisotropy shows no influence. Further focus is put on the temperature variation of the resonance field H_{res} and peak-to-peak linewidth ΔH_{pp}, for which several models are investigated. Finally, a full line shape analysis is presented based on a Landau-Lifshitz model with complex damping.

5.1 $\mathrm{Fe}_x\mathrm{Pt}_{1-x}$ nanoparticles in the isotropic regime

At temperatures far above the blocking temperature T_{b}, the influence of the anisotropy energy E_{A} on the magnetic behaviour in $\mathrm{Fe}_x\mathrm{Pt}_{1-x}$ magnetic nanoparticles is widely suppressed by the thermal energy $\mathrm{k_B}T$. Therefore, room temperature MRS-spectra have been analysed to reveal three basic parameters characterizing the dynamics of $\mathrm{Fe}_x\mathrm{Pt}_{1-x}$ nanoparticles in the isotropic regime.

Effective g-factor, ratio $\mu_L^{\text{eff}}/\mu_S^{\text{eff}}$ of orbital and spin angular momentum, and damping constant α

The gyromagnetic ratio $\gamma = g_0\mu_{\text{B}}/\hbar$, which is the ratio between magnetic dipole moment and the angular moment of the particle, is determined by the g-factor of the precessing moment. Generally, the determination of the g-factor based on resonance absorption measurements is hampered by large intrinsic magnetic anisotropy fields which, moreover, may be temperature dependent. In ensembles of superparamagnetic nanoparticles well above their blocking temperature, these intrinsic magnetic fields become negligible small due to thermal fluctuations. Therefore, the resonance absorption behaviour of $\text{Fe}_x\text{Pt}_{1-x}$ nanoparticles at room temperature is considered first, to investigate the influence of $\text{Fe}_x\text{Pt}_{1-x}$ composition on g-factor and damping parameter α.

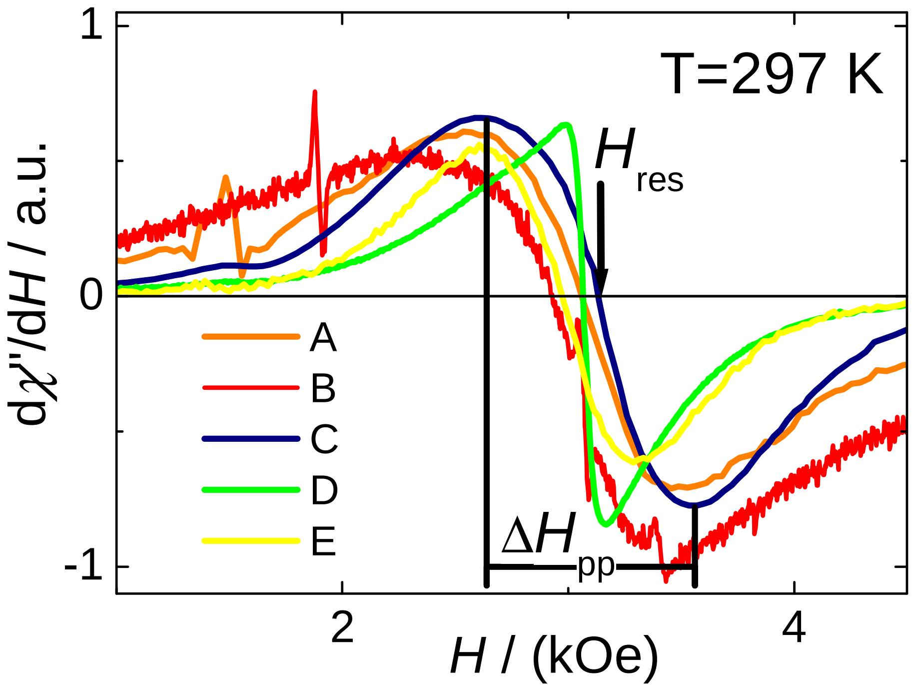

Figure 5.1: MRS-spectra of different $\text{Fe}_x\text{Pt}_{1-x}$ nanoparticle samples recorded at $\omega/(2\pi) = 9.1$ GHz and room temperature ($T = 297$ K). As depicted for sample C the resonance field H_{res} is given by the zero crossing $\text{d}\chi''/\text{d}H = 0$, and the peak-to-peak linewidth ΔH_{pp} by the field distance between absorption maximum and minimum of the derivative. For better comparison, the amplitudes of the MRS-spectra have been normalized in the peak-to-peak amplitude.

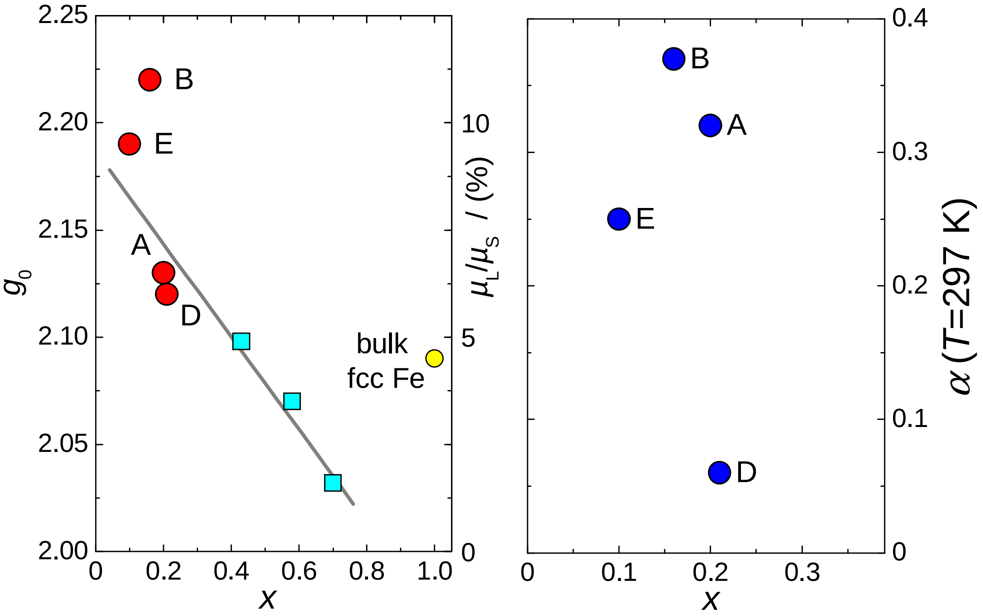

Figure 5.2: Left panel: Composition dependent g-factor determined for $\mathrm{Fe}_x\mathrm{Pt}_{1-x}$ nanoparticles at room temperature. Additionally, g-factors from literature [90] and the g-factor of bulk fcc Fe have been added for ease of comparison. The right scale in the left panel denotes $\mu_\mathrm{L}/\mu_\mathrm{S}$ the ratio between orbital and spin momentum according to Eq. 2.68. Right panel: No correlation was visible between damping constant α and composition in the room temperature MRS-spectra.

In Fig. 5.1, the derivatives of microwave $\mathrm{Fe}_x\mathrm{Pt}_{1-x}$ absorption spectra measured at $\omega/(2\pi)$ =9.1 GHz and room temperature $T = 297$ K are shown. At that temperature, all samples exhibit a main resonance close to $H_\mathrm{res} \approx 3$ kOe, with peak-to-peak line-width ΔH_pp ranging from about 0.2 kOe (sample D) to 1.1 kOe (sample B). The MRS-spectra of samples A, D, E display one or several additional narrow resonances below $H = 2$ kOe with $\Delta H_\mathrm{pp} \approx 50$ Oe. These additional narrow absorption lines will be discussed in Sec. 5.3. From H_res and ΔH_pp of the main resonance the g-factor $g = \hbar\omega/\mu_\mathrm{B}H_\mathrm{res}$ and the damping $\alpha = \Delta H_\mathrm{pp}/H_\mathrm{res}$ were determined and displayed in Fig. 5.2 as a function of composition.

The resulting g-factor of the $\mathrm{Fe}_x\mathrm{Pt}_{1-x}$ nanocrystals is linearly decreasing with Fe content x. Interestingly, this trend found for the $\mathrm{Fe}_x\mathrm{Pt}_{1-x}$ samples agrees well with the behaviour observed in [90] for $x = 0.4 \ldots 0.7$, that g

linearly decreases with increasing x as also indicated by the squares in Fig. 5.2. So it is concluded that, for compositions $x = 0.1 \ldots 0.7$, the isotropic g-factor is determined mainly by the iron content. The large g-factor observed in sample B may be caused by the large line-width already present at room temperature, leading to an asymmetry of the line with a potential shift of the resonance field H_{res} determined as $\mathrm{d}\chi''/\mathrm{d}H(H) = 0$. This could be originating from an inhomogeneous $\mathrm{Fe}_x\mathrm{Pt}_{1-x}$ compositional structure, i. e. iron-rich and platinum-rich areas within the nanoparticles.

From the g-factor, the contributions due to spin and orbital angular momentum can be obtained using the relation Eq. 2.68, $\mu_L/\mu_S = (g-2)/2$ [40]. This ratio is shown as the right y-axis scale in the left panel of Fig. 5.2.

In strongly exchange coupled binary systems such as $\mathrm{Fe}_x\mathrm{Pt}_{1-x}$ with an induced polarization at the Pt site, the effective collective orbital and spin contributions are measured. It turns out that the dominating contribution to the g-factor is the spin moment, as depicted in Fig. 5.2 ($\mu_{\mathrm{L}}/\mu_{\mathrm{S}}$ ratio, right scale), since in cubic crystals the orbital moment is nearly quenched [91] by crystal field effects modifying the electronic states. For all compositions the orbital contribution is found to be below 10%. The coupling between of Fe and (induced) Pt moments has been predicted theoretically and confirmed by experiment to be ferromagnetic in the concentration range $x > 0.3$. From this, the tendency for ferromagnetic order has been found to become more favourable when the chemical disorder is increased. Hence, this composition range can be expanded down to $x \approx 0.1$ for disordered $\mathrm{Fe}_x\mathrm{Pt}_{1-x}$ nanoparticles.

In contrast to the g-value, the damping parameter α displayed no composition dependency. For most samples, a quite large damping constant $0.25 \leq \alpha \leq 0.3$ was found. Only sample D exhibits an exceptional small damping $\alpha = 0.06$.

5.2 Resonance field H_{res} and line-width ΔH_{pp} in Fe$_x$Pt$_{1-x}$ nanoparticles at temperatures $T < 300$ K

The influence of thermal fluctuations acting on the magnetization dynamics can be diminished by lowering the temperature, so the impact of anisotropy and magnetic moment emerges more clearly. Therefore, MRS-spectra of Fe$_x$Pt$_{1-x}$ nanoparticles at lower temperatures have been performed.

5.2.1 Measured MRS-spectra of Fe$_x$Pt$_{1-x}$ nanoparticles

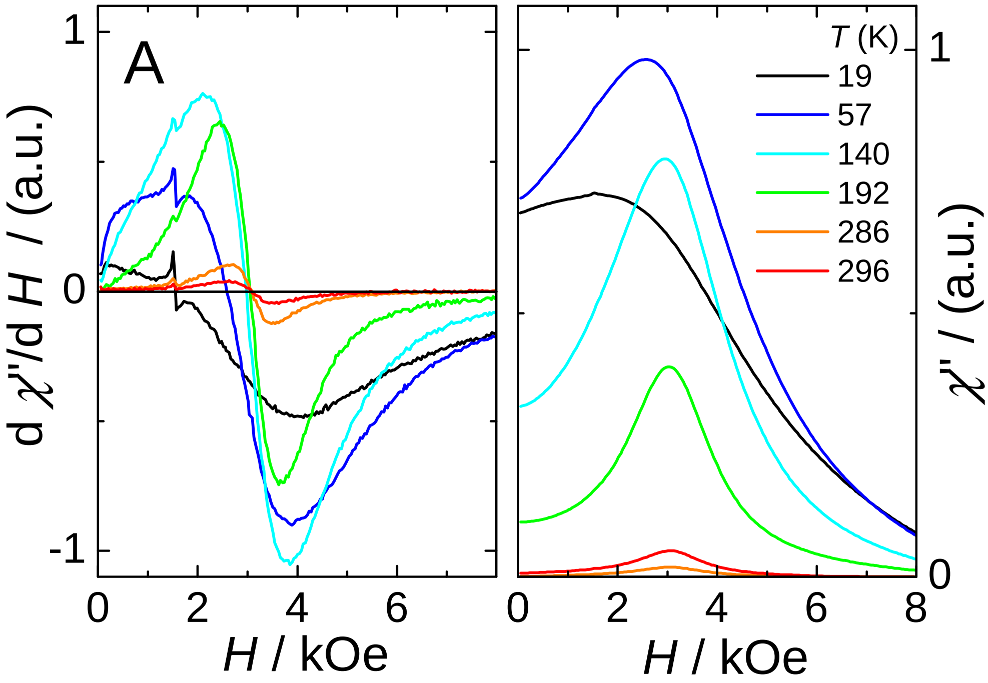

Figure 5.3: Typical temperature dependent MRS-spectra of Fe$_x$Pt$_{1-x}$ (sample A) recorded at 9.1 GHz. With decreasing temperature, the resonance is shifting towards lower fields, while the linewidth is increasing and the line shape is becoming unsymmetrical. Left panel: The derivative $d\chi''/dH$ as recorded by the spectrometer. Note the additional narrow temperature independent resonance at $H \approx 1.5$ kOe on top of the main resonance. Right panel: After numerical integration to obtain the absorption $\chi''(H)$.

As an example, the spectra of sample A at selected lower temperatures down

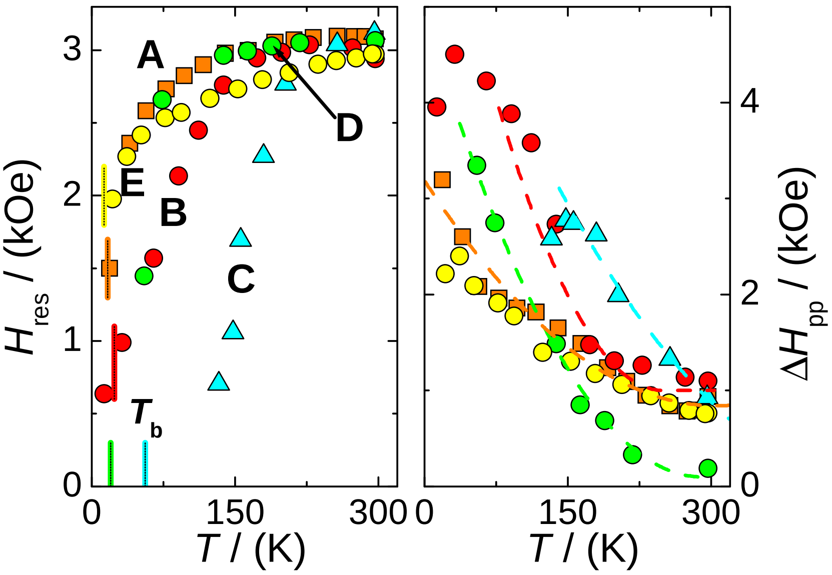

Figure 5.4: Temperature behaviour of Fe_xPt_{1-x} nanoparticles determined for MRS-spectra ($d\chi''/dH$). Left panel: Downward shift of H_{res} with decreasing temperature. The vertical coloured lines mark the individual blocking temperatures T_b determined from the ZFC-magnetization, see Fig. 4.7. Right panel: Increase of line-width ΔH_{pp} with decreasing temperature. This behaviour can be described by a mean-field ansatz similar to Eq. 2.13 $\Delta H_{pp}(T) = \Delta H_{pp}(0)(1 - T/TC)^2$ using the Curie temperatures T_C determined from the ZFC-measurements, see Fig. 4.7, as indicated by the corresponding lines.

to $T = 20$ K are depicted in Fig. 5.3. With decreasing temperature, amplitude and line-width of the resonance are strongly increasing. Furthermore, the resonance field H_{res} is shifting towards lower fields, in some samples (sample C) reaching zero field at about the (static) blocking temperature. At the lowest temperatures, $T \leq T_b$, the spectra show slight hysteretic behaviour (different amplitudes $d\chi''/dH$ for external field sweeping up or down) for fields $H < 1$ kOe. At all higher temperatures the lines are reversible and have a zero amplitude at zero field, which is to say that $d\chi''/dH|_{H=0} = 0$. The rather symmetric line shape at room temperature becomes more and more asymmetric while lowering the temperature, which shows up more pronounced in the spectra after integrating ($\chi''(H)$, right panel of Fig. 5.3).

The additional narrow resonance visible in samples A, B, E, see Fig. 5.1, also increases in amplitude with decreasing temperature. However, position and width of the line remain constant with temperature. The temperature behaviour of this narrow line is investigated in Sec. 5.3.

The resonance field H_{res} and peak-to-peak line-width ΔH_{pp} of the main resonance have been determined from the spectra and are collected in Fig. 5.3. The right panel shows the shift of H_{res} towards lower fields and even zero field (samples D and C) already before approaching the (static) blocking temperature T_{b}. In samples A, B, E the downward shift is much less pronounced so that, even at T_{b}, the resonance field is still larger than 0.5 kOe. For all samples, the line-width ΔH_{pp} is initially increasing with decreasing temperature. Only, if H_{res} is approaching zero field the peak-to-peak line-with is decreasing again to some extent, since the lower peak of $\mathrm{d}\chi''/\mathrm{d}H$ is located at zero field then and the higher peak is approaching zero field, as can be seen in sample B and C. The temperature-dependent growth of ΔH_{pp} in samples A, B, C and D could be adequately described using the model $\Delta H_{\mathrm{pp}}(T) = \Delta H_{\mathrm{pp}}(0)(1-T/T_{\mathrm{C}})^2$ with Curie temperatures T_{C} determined from the ZFC-measurements (see Fig. 4.7) has been used.

5.3 The additional narrow resonance at $g_{\mathrm{eff}} \approx 4$ in $\mathrm{Fe}_x\mathrm{Pt}_{1-x}$ nanoparticles

As can be seen in Fig. 5.3, $\mathrm{Fe}_x\mathrm{Pt}_{1-x}$ samples A, B, and E show a narrow resonance below $H_\omega \leq 2$ kOe in addition to the broad main resonance located at $H_\omega \approx 3$ kOe. Contrary to the main resonance, position and width of the narrow resonance show no temperature variation, while the amplitude is increasing with decreasing temperature. By fitting this narrow resonance line with the derivative of a Lorentz line $\mathrm{d}\chi''(H)/\mathrm{d}H = -16I\,w(H-H_{\mathrm{res}})/(\pi(w^2+4(H-H_{\mathrm{res}})^2)^2)$, position H_{res}, width ΔH_{pp} and amplitude $I(T)$ have been determined as functions of temperature.

The resonances are located at $H_{\mathrm{res}} = 1.552(6), 1.55(2), 1.429(3))$ kOe and have a width $\Delta H = 0.15(4), 0.10(5), 0.11(2))$ kOe for sample A, B, and E over the whole temperature range. From H_{res}, temperature independent g_{eff}-values of 4.5(2) (A) and 4.2(1) for B and E have been determined. This narrow resonance was not observed in samples C and D, which may be caused by a reduced dynamic range of the Lock-in amplifier required for the detection of the larger amplitudes in that samples. So, in these samples, the narrow resonance may be present, despite having been concealed by the main resonance.

A similar resonance has been observed in FMR spectra of of annealed iron-containing borate glass [92] and was attributed to paramagnetic Fe^{3+} impurities. This was supported by the integrated amplitude $I(T)$ of the additional resonance, which has been displayed in Fig. 5.5. After normalizing to the amplitude at $T = 0$, a Curie-like behaviour C/T was observed for the temperature dependence of $I(T)$ of the three samples A,B, and E. The ratio between integrated amplitude of main and additional narrow resonance (at a temperature close to the blocking temperature T_b) allows the rough estimation of less than five per cent for the impurity fraction in the $\mathrm{Fe}_x\mathrm{Pt}_{1-x}$ samples.

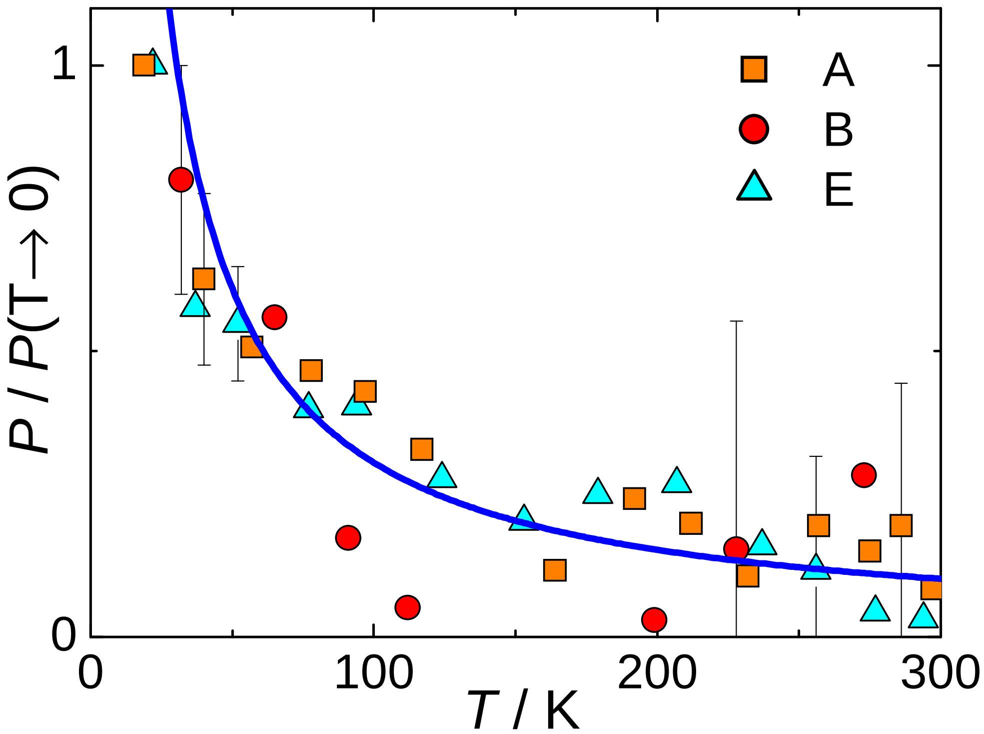

Figure 5.5: Curie-like behaviour of the MRS-amplitude of the additional narrow resonance at $g_\mathrm{eff} \approx 4$ observed in $\mathrm{Fe}_x\mathrm{Pt}_{1-x}$ nanoparticles. The blue line represents a Curie law $C/T = 30.5/T$.

5.4 Models to describe the full line shape of MRS-spectra

5.4.1 Resonance field H_{res} and line-width ΔH_{pp} in the basic Landau-Lifshitz and Gilbert model

The first step towards the description of the experimentally observed temperature variation of resonance field H_{res} and line-width ΔH_{pp} in $\mathrm{Fe}_x\mathrm{Pt}_{1-x}$ nanoparticles was to check by simulations the behaviour of the two basic line shape approaches, the Landau-Lifshitz line shape, Eq. 2.60 and the Gilbert line shape, Eq. 2.61. For these simulations, a fixed value of $H_\omega = 3$ kOe was assumed and the damping parameter α was varied within the range $0.001\ldots1.5$.

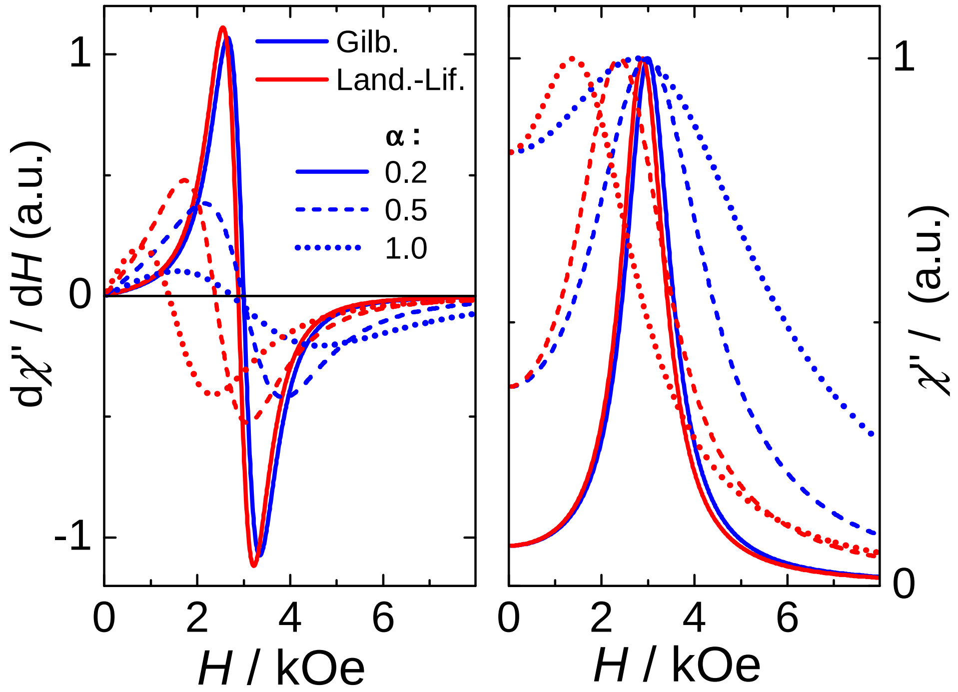

Figure 5.6: Simulated magnetic resonance absorption spectra at $H_\omega = 0.3$ T for three values of the damping parameter $\alpha = 0.2, 0.5$, and 1.0 using the Landau-Lifshitz line shape, Eq. 2.60, (red lines) and the Gilbert line shape, Eq. 2.61, (blue lines). In the left panel, the derivative of the transverse magnetic susceptibility $\mathrm{d}\chi''(H)/\mathrm{d}H$ is shown, while right panel directly displays the susceptibility $\chi''(H)$. Note, the curves have been normalized to their maximum absorption value $\max(\chi''(H))$ for better comparison.

Examples of simulated resonance curves for three different values of α are displayed in Fig. 5.6. For graphical representation, the curves have been normalized to maximum absorption value $\max(\chi''(H))$.

With increasing α, the line-width increases and the resonance field H_{res} is shifted towards lower fields for both line shape types. But the shift is much stronger for the Landau-Lifshitz line shape, while the Gilbert lines are only moderately shifted for quite large values of α. Furthermore, the high field peak position of the resonance in the derivative $\mathrm{d}\chi''(H)/\mathrm{d}H$ of the line is always above H_ω for all values α in the Gilbert model, while it is located below H_ω in the Landau-Lifshitz line shape for larger values of α. This explains the decrease in the ΔH_{pp} while approaching zero field of the resonance field in this line shape, as can be seen in Fig. 5.7, where the H_{res} and ΔH_{pp} resulting from the simulations for both lines shape types are drawn together.

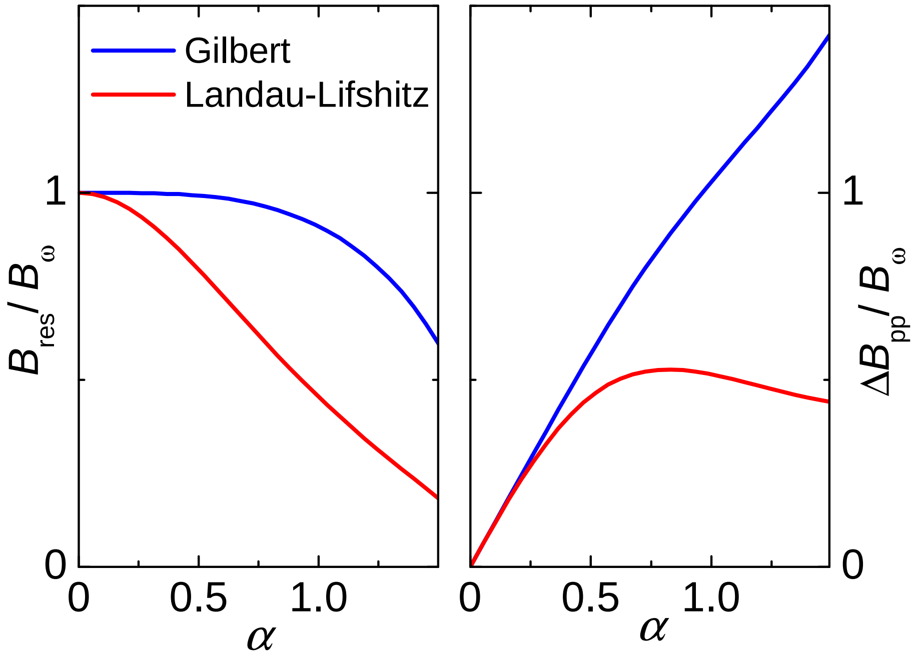

Figure 5.7: Resonance field H_{res} and peak-to-peak linewidth ΔH_{pp} resulting from simulations of Landau-Lifshitz (Eq. 2.60) and Gilbert (2.61) line shape spectra as a function of α.

Both, Landau-Lifshitz and Gilbert model in their basic forms yield only symmetrical lines shapes and are therefore suitable to describe the MRS-spectra at high temperatures, where the observed lines are symmetrical. Furthermore, the strong influence of the damping α on both parameters H_{res} and ΔH_{pp} in the Landau-Lifshitz model has a negative impact compared to the Gilbert line shape. Therefore, more advanced models are taken into account in the following.

5.4.2 Effect of anisotropy on resonance position H_{res} and line-width ΔH_{pp}

In the description of the magnetic resonance spectroscopy the effect of the magnetic anisotropy energy E_{A} is commonly incorporated by the corresponding anisotropy field $H_{\mathrm{A}} = 2E_{\mathrm{A}}/\mu_{\mathrm{p}} = 2K_{\mathrm{eff}}/M_{\mathrm{S}}$.

Introducing anisotropy into the basic Gilbert model

Choosing the basic Gilbert line shape Eq. 2.61, a straightforward approach to include anisotropy in the line shape can be achieved by replacing the external field H by an effective field H_{eff} acting on the precession of the nanoparticle's moment

$$\chi''^{G}(H, H_{\mathrm{A}}) = N_p \mu_p \omega \gamma \alpha \frac{(\gamma H_{\mathrm{eff}})^2 + \omega^2(1+\alpha^2)}{(\gamma H_{\mathrm{eff}})^4 + 2(\omega\gamma H_{\mathrm{eff}})^2(\alpha^2-1) + \omega^4(1+\alpha^2)^2}. \tag{5.1}$$

Here, the effective field is given by the square root of the sum of squared external field H and anisotropy field H_{A}

$$H_{\mathrm{eff}} = \sqrt{H^2 + H_{\mathrm{A}}^2}. \tag{5.2}$$

A simulation of the line shapes $(\mathrm{d}\chi''(H)/\mathrm{d}H)$ for different values of the anisotropy field H_{A} for a small damping, $\alpha = 0.2$, and large damping, $\alpha = 1.0$, is shown in Fig. 5.8. In this approach, the resonance field H_{res} is shifting towards $H = 0$ and the line-width ΔH_{pp} is increasing with the anisotropy field H_{A}. However, an absorption different from zero at zero external field $\mathrm{d}\chi''(H \to 0)/\mathrm{d}H > 0$ is not observed in the experimental MRS-spectra, so this simple way to introduce the anisotropy seems not to be appropriate.

Effect of anisotropy on resonance field H_{res} and line-width ΔH_{pp} determined by energy minimization

The starting point is the energy functional Eq. 2.39 incorporating magnetocrystalline anisotropy and Zeeman field energy, see 2.1.6, which in reduced field

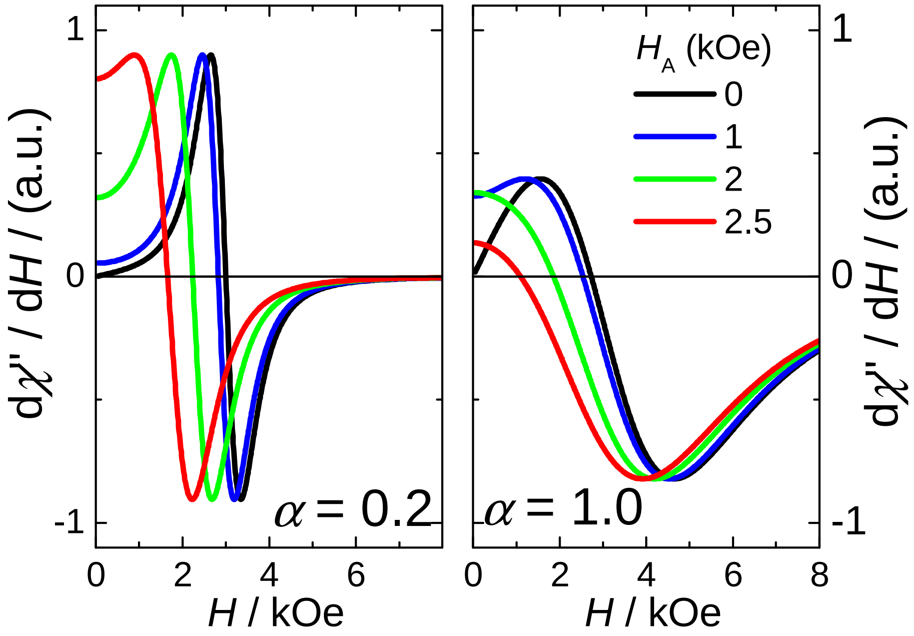

Figure 5.8: Simulation of MRS-spectra at $H_\omega = 3$ kOe for different values of the anisotropy field H_A introduced by an effective field ansatz into the basic Gilbert line shape model according to Eq. 5.1 for small damping $\alpha = 0.2$, left panel and large damping $\alpha = 1.0$, right panel.

units $h = \mu_\mathrm{p} H / 2E_\mathrm{A} = H/H_\mathrm{A}$ may be written as

$$E = -\cos^2(\theta) - 2h\cos(\psi - \theta), \tag{5.3}$$

where θ is the angle between moment μ_p and anisotropy field H_A and ψ between external field H and H_A, as depicted in Fig. 5.9. The resulting equilibrium angle θ_0 of the magnetic moment μ_p in the reduced field h is determined by taking the first derivative of eq. 5.3:

$$\frac{\mathrm{d}}{d\theta}\Big[-\cos^2(\theta) - 2h\cos(\psi - \theta)\Big]_{\theta=\theta_0} = 0. \tag{5.4}$$

Then, the reduced resonance frequency $\Omega = H_\omega/H_\mathrm{A}$ of the precession of the magnetic moment is given by [93; 42]

$$\begin{aligned}\Omega(\psi, h) \equiv \frac{H_\omega}{H_\mathrm{A}} \quad &= \quad \Big[\Big(\cos^2\theta_0(\psi,h) + h\cos(\psi - \theta_0(\psi,h)\Big) \\ &\quad \times \left(\cos 2\theta_0(\psi,h) + h\cos(\psi - \theta_0(\psi,h))\right]^{1/2}. \end{aligned} \tag{5.5}$$

In Fig. 5.10, $\Omega(\psi, h)$ is plotted as a function of h for a series of angles ψ. For $\psi = 0$ (external field parallel to easy axis), the equilibrium angle is $\theta_0 = 0$

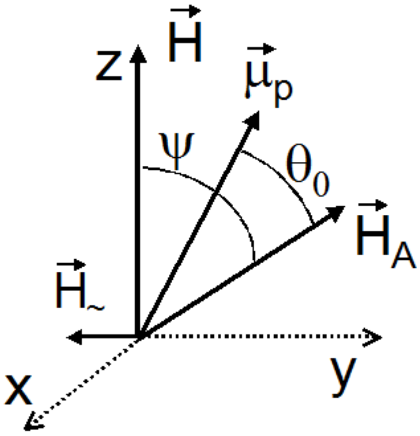

Figure 5.9: Coordinate system defining the angles θ_0 (equilibrium angle between particle moment μ_{p} and the anisotropy field $H_{\mathrm{A}} = 2E_{\mathrm{A}}/\mu_{\mathrm{p}}$ directed along the particle's easy axis) and ψ (angle between external field and easy axis of the particle).

and, according to eq. 5.5, resonance occurs at $1 + h$. For h approaching zero, $\theta_0 \simeq 0$ for all ψ, with a resulting resonance $\Omega = 1$. For $\psi = 90°$ (external field perpendicular to easy axis), θ_0 is shifting from 0° for $h = 0$ to 90° for $h = 1$, with a resulting resonance $\Omega = 0$. Upon further increasing h, the angle θ remains at 90°, so that $\Omega \sim h$ for $h \ll 1$.

Experimentally, resonance absorption is observed sweeping the external field H at a fixed frequency ω. Thus, at a given anisotropy field H_{A} the intersection of the horizontal line $\omega/(\gamma H_{\mathrm{A}}) = \mathrm{const}$ with an individual resonance curve $\Omega(\theta_0(\psi, h))$ determines the corresponding resonance fields $h_r(\psi, \omega/(\gamma H))$. The resulting macroscopic resonance field obtained after averaging numerically over all angles ψ of the external field, $\bar{h}_r = \int \mathrm{d}\sin(\psi) h_r(\psi, \omega)$, is shown in Fig. 5.10 (blue curve). Starting from $\Omega = 1$, for $h = 0$ it asymptotically approaches $\Omega = \gamma h$ for $h \gg 1$.

Already in Eq. 5.1 of this section, the influence of the anisotropy was incorporated phenomenologically by an effective anisotropy field, see Eq. 5.2, so here in a similar way the resonance field is extended $H_\omega \equiv (H_{\mathrm{res}}^2 + H_{\mathrm{A}}^2)^{0.5}$, so that the resonance field can be modelled as

$$H_{\mathrm{res}} = \sqrt{H_\omega^2 - H_{\mathrm{A}}^2} = \frac{\omega}{\gamma}\left(1 - \left(\frac{\gamma H_{\mathrm{A}}}{\omega}\right)^2\right)^{0.5}. \qquad (5.6)$$

Figure 5.11 shows the averaging results in the inverse representation, i.e. the

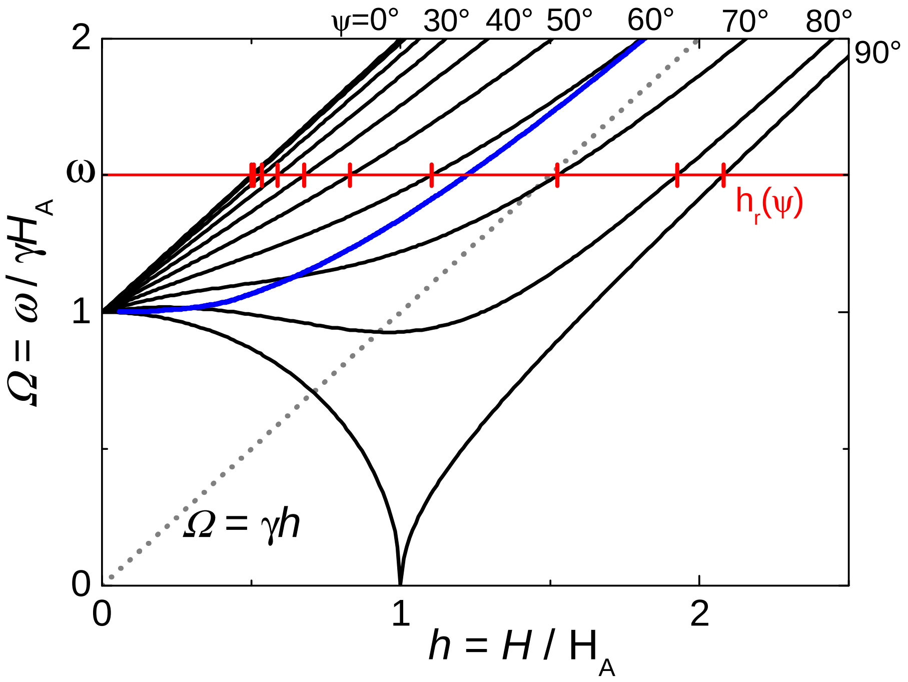

Figure 5.10: Individual normalized resonance fields Ω as a function of the anisotropy field $H_{\mathrm{A}} = 2E_{\mathrm{A}}/\mu_{\mathrm{p}}$ obtained using Eq. 5.5 taking the equilibrium angle θ_0 (by minimization of Eq. 5.3) for individual angles ψ between external field H and easy axis.

averaged resonance field $\gamma\bar{h}_r/\omega$ as a function of Ω^{-1} (grey circles) together with the curve according to Eq. 5.6 (red dotted line). A marked deviation is observed between data and model curve. But by lowering in Eq. 5.6 the exponent 0.5 down to 0.36(1), a nearly perfect agreement between data and model curve is achieved (blue line in Fig. 5.11):

$$H_{\mathrm{res}} = \frac{\omega}{\gamma}\left(1 - \left(\frac{\gamma H_{\mathrm{A}}}{\omega}\right)^2\right)^{0.36} . \qquad (5.7)$$

Inverting Eq. 5.7, the anisotropy field H_{A} may be calculated from a given resonance field H_r for this phenomenological approach, as shown in the inset of Fig. 5.11:

$$H_{\mathrm{A}} = \frac{\omega}{\gamma}\left(1 - \left(\frac{\gamma H_{\mathrm{res}}}{\omega}\right)^{2.78}\right)^{0.5} . \qquad (5.8)$$

Furthermore, the peak-to-peak linewidth may be estimated in this approach by

$$\Delta H = \left[\int \cos\psi \, \mathrm{d}\psi (\omega/\gamma - H_{\mathrm{res}}(\psi))^2\right]^{1/2} . \qquad (5.9)$$

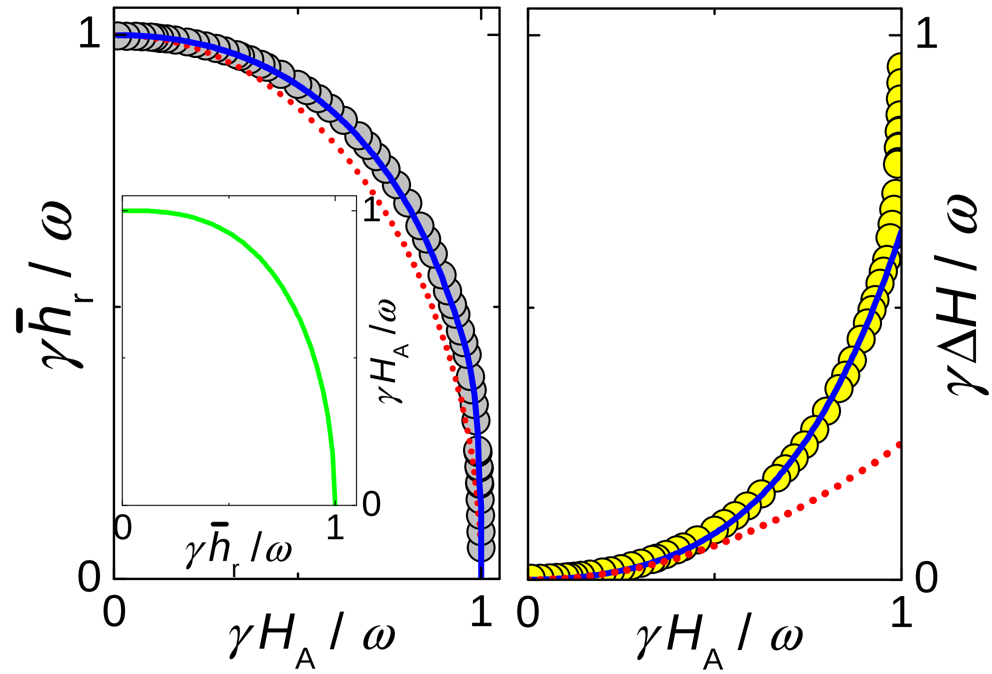

Figure 5.11: Left panel: Averaged resonance field normalized to ω/γ as a function of the anisotropy field H_A in units of ω/γ. The blue curve is the phenomenological approximation Eq. 5.7, the red curve shows the relation Eq. 5.6. The green curve in the inset of the figure shows the inverted relation Eq. 5.8 used to determine H_res from H_A. Right panel: The line-width ΔH normalized to ω/γ as determined from Eq. 5.9 and approximated numerically by $\Delta \approx 0.25H_\mathrm{A}^2$, red line or valid up with higher accuracy by $\Delta H \approx 0.24H_\mathrm{A}^2 + 0.40H_\mathrm{A}^4$, blue line.

For low anisotropy values the line-width can be approximated by $\Delta H \approx 0.25H_\mathrm{A}^2$. A more sophisticated approximation describing the line-width behaviour up to $\gamma H_\mathrm{A}/\omega < 0.95$ is given by $\Delta H \approx 0.24(1)H_\mathrm{A}^2 + 0.40(1)H_\mathrm{A}^4$.

Employing Eq. 5.8, the anisotropy field H_A can be extracted from the resonance position H_res and the individual H_ω determined in Sec.5.2 from the experimental MRS-spectra. The resulting variation of the anisotropy field with temperature $H_\mathrm{A}(T)$ extracted from $H_\mathrm{res}(T)$ for $\mathrm{Fe}_x\mathrm{Pt}_{1-x}$ nanoparticles is depicted in Fig.5.12. An obvious drawback of the analysis is that the maximum possible anisotropy field $H_\mathrm{A} = H_\omega \approx 3$ kOe is reached at lower temperatures for all samples. Interestingly, the line-width $\Delta H(T)$ calculated from Eq. 5.9 (using $H_\mathrm{A}(H_\mathrm{res}(T))$ according to Eq. 5.8) shows a good agreement with the

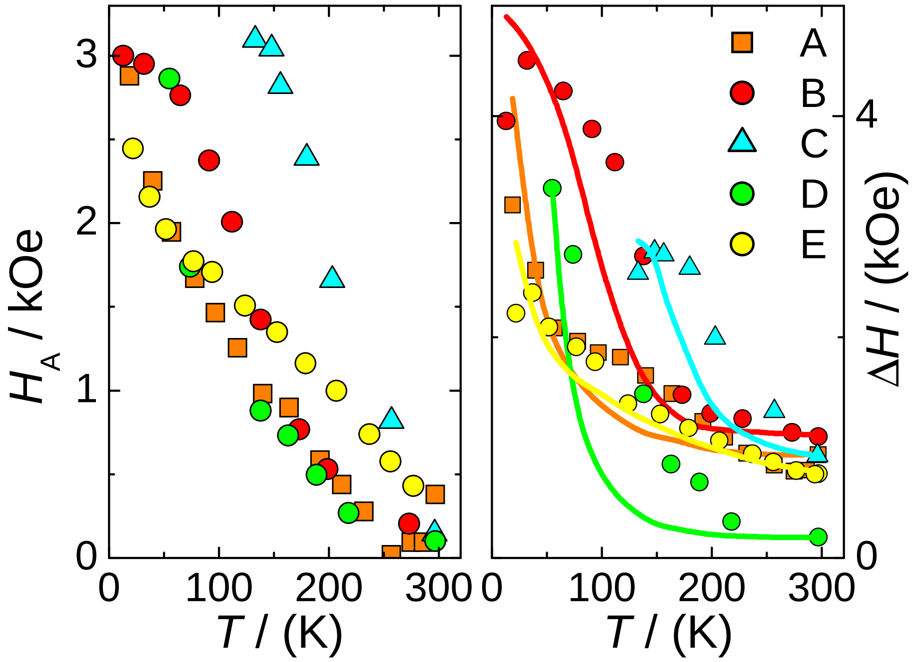

Figure 5.12: Left panel: Temperature dependent anisotropy field $H_{\mathrm{A}}(T)$ of $\mathrm{Fe}_x\mathrm{Pt}_{1-x}$ nanoparticles determined from the resonance field H_{res} using Eq. 5.8. Right Panel: Temperature behaviour calculated from $H_{\mathrm{A}}(T)$ according to Eq. 5.9(lines) together with measured peak-to-peak line-width in $\mathrm{Fe}_x\mathrm{Pt}_{1-x}$ nanoparticles.

measured ΔH_{pp} at lower temperatures, while at mid temperatures the line-width is underestimated. Here, the corresponding value for T_{C} determined from ZFC-measurements and the room temperature value for ΔH_{pp} have been used for the $\mathrm{Fe}_x\mathrm{Pt}_{1-x}$ samples.

5.4.3 MRS line shapes derived from magnetic free energy minimization including anisotropy

An alternative approach to include the effects of magnetocrystalline and shape anisotropy into the MRS-line shape behaviour has been given by Netzelmann [94]. There, the line shape of a ferromagnetic grain is calculated from minimization of the free energy including magnetocrystalline and shape anisotropy terms equivalent to the terms Eq. 2.5 - 2.7. His special ansatz was specialized to uniaxial anisotropy represented by an anisotropy field $\vec{H}_{\mathrm{A}}$ oriented at angles (θ, ϕ) with respect to the external DC field $\vec{H}$ (parallel to z-direction) and the microwave field. Then, the equilibrium orientation (ϑ_0, φ_0) of the moment $\vec{\mu}_p$ is obtained by minimization of the magnetic free energy

$$F(\theta, \phi, \vartheta, \varphi) = -\mu_p[\cos\vartheta + \frac{H}{H_\mathrm{A}}(\sin\vartheta \sin\theta - \cos(\varphi - \phi) + \cos\theta\cos\vartheta)^2]. \quad (5.10)$$

After averaging over the angle ϕ, the transverse susceptibility of a particle with orientation θ is given by

$$\chi^L_{xx}(\theta, H) = \frac{\gamma\mu_p}{2}\frac{(F_{\vartheta_0\vartheta_0} + F_{\varphi_0\varphi_0}/\tan^2\vartheta_0)(1+\alpha^2) - i\alpha\mu_p\omega(1+\cos^2\vartheta_0)}{(1+\alpha^2)(\gamma H_\mathrm{eff})^2 - \omega^2 - i\alpha\omega\gamma\Delta H}, \quad (5.11)$$

where the effective field $H^2_\mathrm{eff} = (F_{\vartheta_0\vartheta_0}F_{\varphi_0\varphi_0} - F^2_{\vartheta_0\varphi_0}/(\mu_p \sin\vartheta_0)^2)$ and $\Delta H = (F_{\vartheta_0\vartheta_0} + F_{\varphi_0\varphi_0}/\sin^2\vartheta_0)/\mu_p$ are given by the second derivatives of F at the equilibrium orientation of $\vec{\mu}_p$. For randomly distributed N_p independent particles per gram one has

$$\chi^L_{xx}(H) = \int_0^{\pi/2} d(\cos\theta)\chi^L_{xx}(\theta, H). \quad (5.12)$$

Simulations of the resulting line shape for different values of the anisotropy field H_A based on this approach are shown in Fig. 5.13. A striking feature in the model curves is the finite value of $\mathrm{d}\chi''_{xx}/\mathrm{d}H$ at H=0, which is in contradiction to the experimental observation. From Eq. 5.11 it follows that $\chi''_{xx}(H \to 0, \theta) \sim H_\mathrm{A}H/\omega^2$, which remains finite even after averaging over all orientations θ, as in Eq. 5.12.

But since MRS-line shape of superparamagnetic and non-ferromagnetic nanoparticles are considered, thermal fluctuations must be taken into into account. The presence of thermal fluctuations leads to a reduction of the anisotropy field [95], and can be modelled as

$$H_\mathrm{A}(z) = H_\mathrm{A}[1/\mathcal{L}(z) - 3/z], \quad (5.13)$$

which for $z = (H/H_\mathrm{T}) \ll 1$ implies that $H_\mathrm{A}(z) = H_\mathrm{A}z/5$, and thus $\chi''_{xx}(H \to 0) \sim H^2$. Here, the thermal fluctuation field H_T is defined as

$$H_\mathrm{T} \equiv \frac{\mathrm{k_B}T}{\mu_\mathrm{p}(T)}, \quad (5.14)$$

and $\mathcal{L}(z)$ is the Langevin function. Then, Eq. 5.13 inserted into Eq. 5.10 was employed to calculate the model MRS-spectra, taking into account the effect of thermal fluctuations of superparamagnetic nanoparticles on the anisotropy field. As depicted by the dotted lines in Fig. 5.13, a thermal fluctuation field $H_\mathrm{T} = 0.1$ kOe already leads to a vanishing susceptibility of the resonance at zero field and a distinct reduction of the line intensity for anisotropy fields $H_\mathrm{A} > 1$ kOe.

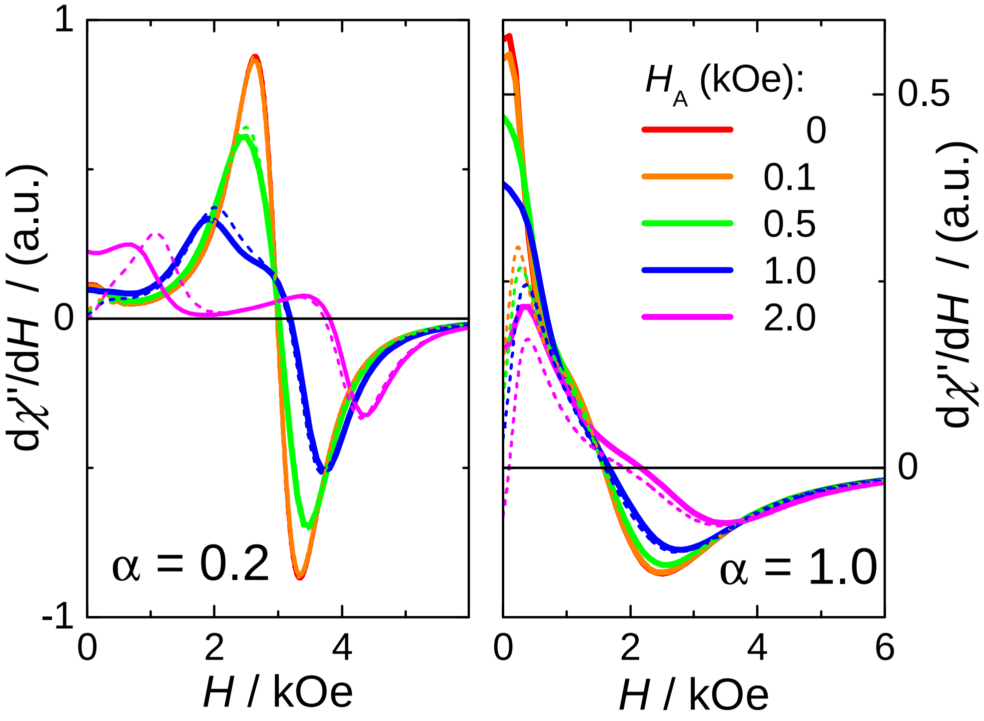

Figure 5.13: Model MRS-spectra using the anisotropic line shape model according to Eq. 5.12 for $H_\omega = 0.3$ kOe and different values of H_A for $\alpha = 0.2$ left panel and $\alpha = 1.0$ (right panel). The straight lines represent model curves without thermal fluctuations, and the dotted lines taking thermal fluctuations into account, assuming a thermal fluctuation field of$H_\mathrm{T} = 0.1$ kOe.

Any attempts to account for the downward-shift in the resonance field H_res by introducing a (uniaxial) magnetocrystalline anisotropy failed, since low values of the anisotropy field H_A had no effect on H_res due to orientational averaging. Larger anisotropy fields H_A could provide a sufficient shift of H_res, but produced severe distortions of the calculated line shape.

Furthermore, the strong dependency of this approach on the temperature dependent particle moment μ_p effecting the thermal fluctuation field H_T at the expense of numerical implementation (the summation over θ can not be written in closed form in a fitting routine) are however appreciable reasons to consider a more simple approach as presented in the following section.

5.5 Full line shape description of the measured MRS-spectra

5.5.1 Landau-Lifshitz model with complex damping

As already seen in Sec. 5.4.1, the effect of the damping parameter α on resonance field H_{res} and line-width ΔH_{pp} is more pronounced in the Landau-Lifshitz model than compared to the Gilbert model. To yield a more appropriate model suitable for a full line shape analysis of the measured MRS-spectra of the $\mathrm{Fe}_x\mathrm{Pt}_{1-x}$ nanoparticles, the Landau-Lifshitz model with a temperature-dependent complex damping was introduced:

$$\hat{\alpha}(T) = \alpha(T) - \mathrm{i}\beta(T). \tag{5.15}$$

The approach of complex damping has already been used to describe the domain wall dynamics in ferromagnetic EuO [96].According to Eq. 2.51, Sec. 2.2.1, this formally corresponds to a negative g-shift

$$g(T) = g_0 - \beta(T) g_0. \tag{5.16}$$

Combining Eq. 5.15 and Eq. 5.16 with Eq. 2.60, the dynamic susceptibility with complex damping is given by

$$\chi''(H) = \frac{N_{\mathrm{p}}\mu_p H_\omega \alpha g_p}{2}\left(\frac{1}{(\alpha H_\omega)^2 + (H_\omega - g_p H)^2} + \frac{1}{(\alpha H_\omega)^2 + (H_\omega + g_p H)^2}\right). \tag{5.17}$$

5.5.2 Temperature variation of the complex damping parameter $\hat{\alpha}(T)$

With this approach, the MRS-spectra line shapes could be described over the full temperature range with high accordance, as shown in Fig. 5.14.

From fitting the model Eq. 5.17 to the experimental MRS-spectra the temperature dependences of the two damping parameter $\alpha(T)$ and $\Delta g(T)/g_0$ have been determined, as shown for sample A in Fig. 5.15.

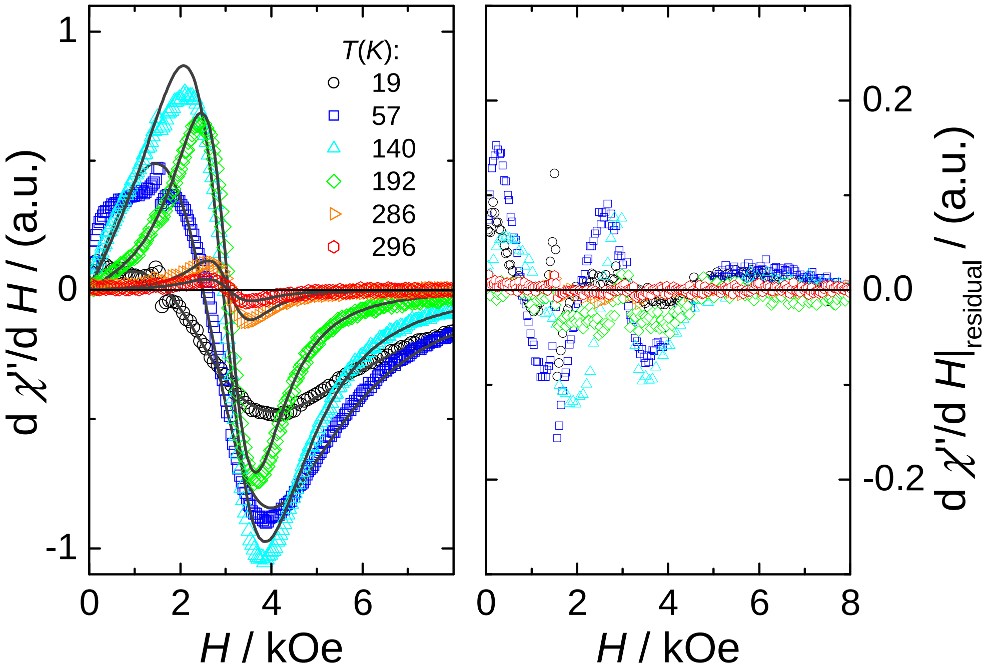

Figure 5.14: Full line shape analysis using the complex Gilbert model Eq. 5.17 for temperature dependent MRS-spectra of $\mathrm{Fe}_x\mathrm{Pt}_{1-x}$ nanoparticle sample A. Shown are recorded derivative $\mathrm{d}\chi''/\mathrm{d}H$ together with the fitted curve (left panel) and the residuum (difference data-fit values, right panel) for several selected temperatures, the corresponding fit parameters for $\alpha(T)$ and $\Delta g(T)/g_0$ as a function of temperature are displayed in Fig. 5.15.

Except for sample C, all other $\mathrm{Fe}_x\mathrm{Pt}_{1-x}$ samples show a very similar temperature behaviour of the complex component of the damping, $\Delta g/g_0$.

A physical justification for the complex damping would be rather speculative, especially since a general theory of magnetization is not yet available. The similarity of the complex damping behaviour implicates a relation with intrinsic effects, since no influence of the moment distribution μ_p, structural disorder or composition are noticeable.

The temperature variation of both components of the complex damping obey the same power law as the magnetic moments $\mu_\mathrm{p}(T) = \mu(0)q(T)$, which implies that

$$\hat{\alpha}(T) = (\alpha - i\beta)q(T) + \alpha_0. \tag{5.18}$$

Also, it was observed that the intensity I of the MRS-spectra roughly shows the same temperature dependence as the moments $I(T) \sim \mu_\mathrm{p}(T)$. From this,

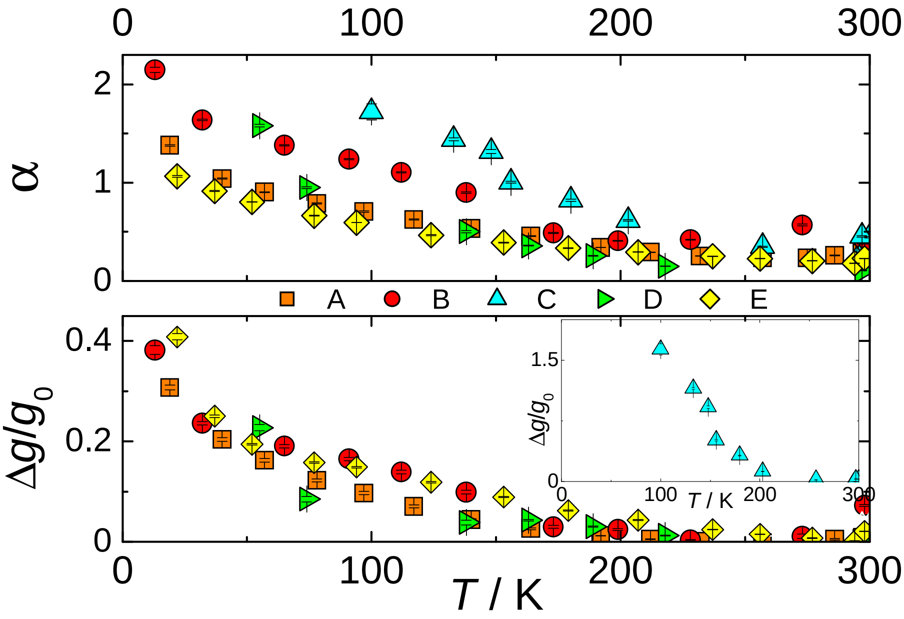

Figure 5.15: Complex damping parameters α (top panel) and $\Delta g/g_0$ (bottom panel), obtained by fitting the temperature dependent MRS-spectra using the landau-Lifshitz model with complex damping Eq. 5.17.

it can be concluded that superparamagnetic fluctuations do not have a large influence, as otherwise a decrease of the intensity $I(T) \sim \mu_p(T)/T$ would have been expected.

The striking feature observed in the MRS-spectra of the $\mathrm{Fe}_x\mathrm{Pt}_{1-x}$ nanoparticles are the large magnitudes and the temperature variation of both components, $\alpha(T)$ and $\Delta g(T)$ of the complex damping. It has been suggested that this is caused by the scattering of a q=0-magnon by an electron/hole excitation [97], well established for bulk ferromagnets [98]. But deeper quantitative conclusions require more detailed information on the electronic and magnetic structure of the $\mathrm{Fe}_x\mathrm{Pt}_{1-x}$ nanoparticles.

Chapter 6

Summary and conlusions

This work focussed on the structural and magnetic characterization of disordered platinum-rich Fe_xPt_{1-x} nanoparticles, which were prepared following a wet-chemical organometalic nanoparticle synthesis by thermal decomposition in the presence of stabilizing oleic acid. Structure and morphology of the nanoparticles were characterized by TEM and XRD. SQUID-susceptometry and magnetic resonance spectroscopy (MRS) were employed for determination of the quasi-static and dynamic magnetic parameters.

The main results, which have been obtained for the Fe_xPt_{1-x} nanoparticles, can be summarized as follows:

The samples consist of spherical nanocrystalline particles with a narrow log-normal shaped distribution of particle sizes at a mean diameter of about 4 nm. A platinum-rich composition of the Fe_xPt_{1-x} nanoparticles in the range $x = 0.1 \ldots 0.25$ was derived from the lattice constant a_0 and confirmed by analysis of the Curie temperature T_C found in ZFC magnetization measurments. Chemical ordering of the Fe_xPt_{1-x} nanoparticles was not observed and could not be induced by annealing treatment.

Both, ZFC- and AC-magnetization reveal a log-normal energy barrier distribution with mean anisotropy energies E_A/k_B in the range 300 K to 600 K. An unexpected relation $\tau_0 \sim E_A^{-1/5}$ between the relaxational pre-factor τ_0 and mean anisotropy energy E_A has been found experimentally. A second magnetic phase at a higher anisotropy energy $E_A/k_B \approx 1900$ K is observed in one sample, indicating the formation of different magnetic phases in Fe_xPt_{1-x} nanoparticles.

The magnetic moment μ_p of the $\mathrm{Fe}_x\mathrm{Pt}_{1-x}$ nanoparticles shows a distinct temperature dependence following Bloch's law $\mu_\mathrm{p}(T) \sim 1 - BT^\beta$, with a exponent $\beta = 3/2$ typical for bulk systems, while the resulting coefficients B are much larger than the bulk value, a phenomenon observed in other nanoparticle systems.

From the magnetization isotherms $M(H,T)$, the same temperature behaviour $q(T)$ of the magnetic moment $\mu_\mathrm{p} = \mu_\mathrm{p}(0)q(T)$ has been derived than extracted from the effective Curie constant as determined from ZFC-measurements at $H = 0.1$ kOe. The magnetic moment $\mu_\mathrm{p}(T = 0)$ was obtained by extrapolation of the magnetic moment $\mu_\mathrm{p}(T_\mathrm{m})$ measured at a temperature T_m close above the blocking temperature. Hereby, a log-normal size distribution of the particles was taken into account and the observed Bloch behaviour of the magnetic moment was used for the extrapolation. The resulting moments in the range 500 μ_B to 1000 μ_B only show a weak correlation with the composition x of the $\mathrm{Fe}_x\mathrm{Pt}_{1-x}$ nanoparticles.

Furthermore, the anisotropy energy in the $\mathrm{Fe}_x\mathrm{Pt}_{1-x}$ nanoparticles was found to increase linearly with the saturation magnetization $M_\mathrm{S}(T = 0)$. It is assumed that this can be used to assess the magnetic order induced by the chemical order independent of the composition of the $\mathrm{Fe}_x\mathrm{Pt}_{1-x}$ nanoparticles.

The isotropic g-factor of the $\mathrm{Fe}_x\mathrm{Pt}_{1-x}$ nanoparticles determined from room-temperature MRS-measurements at 9 GHz are decreasing linearly with increasing iron content x, and confirm this trend reported in literature for $\mathrm{Fe}_x\mathrm{Pt}_{1-x}$ nanoparticles with $x = 0.4 \ldots 0.7$. It turns out that the dominating contribution to the g-factor arises from the spin moment, while the orbital moment contribution is below 10% for all samples. From the line-width of the MRS-spectra, quite large damping constants α in the range $0.2 \ldots 0.4$ are found for most of the samples, which are independent of the composition of the $\mathrm{Fe}_x\mathrm{Pt}_{1-x}$ nanoparticles. One sample (D) exhibits a very small line width with corresponding $\alpha = 0.06$.

From temperature dependent MRS-measurements, the strong shift of the resonance field H_res towards smaller fields and an increase in line-width ΔH_pp with decreasing temperature are observed. The analysis of the basic phenomenological Landau-Lifshitz and Gilbert line shapes are insufficient for an adequate description of the measured spectra, especially at low temperatures, where broad and asymmetric lines are recorded.

To improve the description of the line shapes, the anisotropy was incorporated into the Gilbert model. To this end, the effect of the anisotropy field $H_{\mathrm{A}} = 2E_{\mathrm{A}}/\mu_{\mathrm{p}}$ on resonance field and line-width was simulated for two different approaches. An analytical expression was derived to determine the anisotropy field H_{A} from the resonance position H_{res}. From this the temperature dependency of the anisotropy $H_{\mathrm{A}}(T)$ was estimated. As a cross check the line-width $\Delta H(T)$ calculated from $H_{\mathrm{A}}(T)$ agrees reasonably well with the measured line-width ΔH_{pp} of the MRS-spectra.

Since these models did not describe the full line shape, especially the observed asymmetry of the MRS-spectry at low temperatures, sophisticated line shape models have been investigated. The resulting line shape based on the minimization of the free energy including magnetic anisotropy could not provide a convincing match with the observed line shapes. One striking feature here was the finite absorption at zero field, which was not observed experimentally.

Finally, using the model of Landau-Lifshitz, line shape with complex damping allowed for a very good description of the measured MRS-spectra. With only three free parameters, stable fits of this model to the experimental data were achieved. The resulting temperature behaviour of the complex damping parameter $\Delta g/g_0$ was found to be the same for all $\mathrm{Fe}_x\mathrm{Pt}_{1-x}$ samples except sample C. More variation was observed in the real part $\alpha(T)$. A similar approach has been suggested and applied for the description of the domain wall dynamics in ferromagnetic EuO; in any case the underlying physics deserves further detailed investigations.

The additional temperature-independent narrow resonance observed in some $\mathrm{Fe}_x\mathrm{Pt}_{1-x}$ nanoparticles with an effective g-factor $g_{\mathrm{eff}} \approx 4$ was attributed to paramagnetic Fe^{3+} impurities. This was supported by the same Curie-like behaviour of the amplitude of the narrow line.

Magnetic susceptibility measurements are indispensable to determine quasi-static properties of magnetic nanoparticles. In combination with magnetic resonance spectroscopy, which is an excellent technique for analysing the dynamics magnetic nanoparticles directly using the electronic moments as local probes. It could be shown, that this allows the investigation of the influence of order and compositional effects on the resulting magnetic properties of transition metal nanoparticles, mainly expressed by the complex behaviour of anisotropy and magnetic moment.

Bibliography

[1] K.E. Drexler. *Nanosystems: Molecular Machinery, Manufacturing and Computation*. Wiley interscience publication, 1992.

[2] K. E. Drexler. Molecular engineering: An approach to the development of general capabilities for molecular manipulation. *Proc. Natl. Acad. Sci.*, 78(9):5275–5278, 1981.

[3] Thomson Reuters. Web of Science. `http://thomsonreuters.com/thomson-reuters-web-of-science/`, 2014. [Online; accessed 10-August-2014].

[4] S. Sun, C. B. Murray, D. Weller, L. Folks, and A. Moser. Monodisperse FePt nanoparticles and ferromagnetic FePt nanocrystal superlattices. *Science*, 287(5460):1989–1992, 2000.

[5] B. Stahl, J. Ellrich, R. Theissmann, M. Ghafari, S. Bhattacharya, H. Hahn, N. S. Gajbhiye, D. Kramer, R. N. Viswanath, J. Weissmueller, and H. Gleiter. Electronic properties of 4-nm FePt particles. *Phys. Rev. B*, 19(67):014422–1–12, 2003.

[6] D. Weller, A. Moser, l. Folks, M. E. Best, W. Lee, M. F. Toney, M. Schwickert, J. U. Thiele, and M. Doerner. High K_u materials approach to 100 Gbits/in^2. *IEEE Trans. Magn.*, 36(1):10–15, 2000.

[7] M. Farle. Ferromagnetic resonance of ultrathin metallic layers. *Rep. Prog. Phys.*, 61(7):755–826, 1998.

[8] J. A. Osborn. Demagnetizing factors of the general ellipsoid. *Phys. Rev.*, 67(11+12):351–357, 1945.

[9] E. C. Stoner and E. P. Wohlfarth. A mechanism of magnetic hysteresis in heterogeneous alloys. *Philos. Trans. London Ser. A*, 240(826):599–642, 2003.

[10] L. Néel. Théorie du traînage magnêtique des ferromagnêtiques en grains fins avec applications aux terres cuites. *Ann. Geophys. (C.N.R.S.)*, 5: 99–136, 1949.

[11] W. F. Jr. Brown. Relaxational behavior of fine magnetic particles. *J. Appl. Phys.*, 30:130 S–132 S, 1959.

[12] W. F. Brown. Thermal fluctuations of a single-domain particle. *Phys. Rev.*, 130(5):1677–1686, 1963.

[13] M. Farle. Critical size and nucleation field of ideal ferromagnetic particles. *Phys. Rev. B*, 106(3):446–455, 1957.

[14] N. Kikuchi, S. Okamoto, and O. Kitakami. The critical size between single domain and multidomain in $L1_0$-FePt particles. *J. Appl. Phys*, 103: 07D511–1–3, 2008.

[15] M. Watanabe, T. Nakayama, K. Watanabe, T. Hirayama, and A. Tonomura. Microstructure and magnetic properties of high-coercive Fe-Pt alloy thin films. *Mater. Trans. JIM*, 37(3):489–493, 1996.

[16] B. D. Cullity. *Introduction to Magnetic Materials.* Addison-Wesley, New York, 1972.

[17] D. Zhang, K. J. Klabunde, and C. M. Sorensen. Magnetization temperature dependence in iron nanoparticles. *Phys. Rev. B*, 58(21):14167–14170, 1998.

[18] M. D. Kuz'min. Shape of temperature dependence of spontaneous magnetization of ferromagnets: Quantitative analysis. *Phys. Rev. Lett.*, 94 (10):107204–1–4, 2005.

[19] Z. Q. Qiu, J. Pearson, and S. D. Bader. Asymmetry of the spin reorientation transition in ultrathin Fe films and wedges grown on Ag(100). *Phys. Rev. Lett.*, 70(7):1006–1009, 1993.

[20] F. Huang, M. T. Kief, G. J. Mankey, and R. F. Willis. Magnetism in the few-monolayers limit: A surface magneto-optic Kerr-effect study of the magnetic behavior of ultrathin films of Co, Ni, and Co-Ni alloys on Cu(100) and Cu(111). *Phys. Rev. B*, 49(6):3962–3971, 1994.

[21] B. Sadeh, M. Doi, T. Shimizu, and M. J. Matsui. Dependence of the Curie temperatures on the diameter of Fe_3O_4 ultra-fine particles. *J. Magn. Soc. Jpn.*, 24:511–514, 2000.

[22] E. P. Wohlfarth. The temperature dependence of the magnetic susceptibility of spin glasses. *Phys. Lett. A*, 70(5-6):489–491, 1979.

[23] M. F. Hansen and S. Mørup. Estimation of blocking temperatures from ZFC/FC curves. *J. Magn. Magn. Mater.*, 203:214–216, 1999.

[24] R. W. Chantrell, M. El-Hilo, and O'Grady K. Competition between ferromagnetism and antiferromagnetism in FePt. *IEEE Trans. Magn.*, 27: 3570–3578, 1991.

[25] F. Tournus and E. Bonet. Magnetic susceptibility curves of a nanoparticle assembly II. simulation and analysis of ZFC/FC curves in the case of a magnetic anisotropy energy distribution. *J. Magn. Magn. Mater.*, 323(9): 1118–1127, 2011.

[26] F. Vernay, Z. Sabsabi, and H. Kachkachi. ac susceptibility of an assembly of nanomagnets: Combined effects of surface anisotropy and dipolar interactions. *Phys. Rev. B*, 90:094416–1–10, 2014.

[27] M. F. Shliomis and V. I. Stepanov. Frequency dependence and long time relaxation of the susceptibility of the magnetic fluids. *J. Magn. Magn. Mater.*, 122:176–181, 1993.

[28] P. Svedlindh, T. Jonsson, and J. L. Garcia-Palacios. Intra-potential-well contribution to the AC susceptibility of a noninteracting nano-sized magnetic particle system. *J. Magn. Magn. Mater.*, 169:323, 1997.

[29] J. L. Garcia-Palacios. On the statics and dynamics of magnetoanisotropic nanoparticles. *Adv. Chem. Phys.*, 112:1–445, 2000.

[30] V. V. Shcherbakova. Magnetic susceptibility of an ensemble of superparamagnetic grains. *Izvestiya Earth Phys.*, 14:308, 1978.

[31] Yu. L. Raikher and V. I. Stepanov. The effect of thermal fluctuations on the FMR line shape in dispersed ferromagnets. *Sov. Phys. JETP*, 75(4): 764–771, 1992.

[32] Yu. L. Raikher and V. I. Stepanov. Ferromagnetic resonance in a suspension of single-domain particles. *Phys. Rev. B*, 50(9):6250–6259, 1994.

[33] L. D. Landau and E. M. Lifshitz. On the theory of the dispersion of magnetic permeability in ferromagnetic bodies. *Phys. Z. Sowjetunion*, 8: 153, 1935. reprinted: Ukr. J. Phys. 53(V):14-22, 2008.

[34] T. L. Gilbert. A Lagrangian formulation of the gyromagnetic equation of the magnetization field. *Phys. Rev.*, 100:1243, 1955.

[35] C. E. Patton. *Magnetic oxides*, volume 2, page 586. Wiley, New York, 1975.

[36] G. V. Skrotskii and L. V. Kurbartov. *Ferromagnetic Resonance*, chapter Phenomenological Theory of Ferromagnetic Resonance. Pergamon Press, 1966.

[37] J. Smit and H. G. Beljers. Ferromagnetic resonance absorption in a highly anisotropic crystal. *Philips Res. Rep.*, 10:113–130, 1955.

[38] L. Baselgia, M. Warden, F. Waldner, S. L. Hutton, J. E. Drumheller, Y. Q. He, P. E. Wigen, and M. Marysko. Derivation of the resonance frequency from the free energy of ferromagnets. *Phys. Rev. B*, 38(4): 2237–2242, 1988.

[39] V. Kambersky. On the Landau-Lifshitz relaxation in ferromagnetic materials. *Can. J. Phys.*, 48(24):2906–2911, 1970.

[40] Ch. Kittel. On the gyromagnetic ratio and spectroscopic splitting factor of ferromagnetic substances. *Phys. Rev.*, 76:743, 1949.

[41] J. H. van Vleck. Concerning the theory of resonance absorption. *Ann. Phys.*, 78:266, 1950.

[42] Ch. Kittel. On the theory of ferromagnetic resonance absorption. *Phys. Rev.*, 73:155, 1948.

[43] E. Isaac and G. Tammann. Über die Legierungen des Eisens mit Platin. *Z. Anorg. Chemie*, 55(1):63–71, 1907.

[44] A. Kussmann, M. Auwarter, and G. v. Rittberg. Die Eisen-Platin-Invare und ihre Ausdehnungs-Anomalien. *Ann. Phys.*, 4:174–182, 1948.

[45] A. Kussmann and G. v. Rittberg. Untersuchung über die Umwandlungen im System Platin Eisen. *Z. Metallk.*, 41(12):470–477, 1950.

[46] A. Kussmann and G. Gräfin v. Rittberg. Über magnetische Eigenschaften von Platin-Eisen Legierungen II. *Ann. Phys.*, 442(3-4):173–181, 1950.

[47] Y. F. Xu, M. L. Yan, and D. J. Sellmyer. FePt nanocluster films for high-density magnetic recording. *J. Nanosci. Nanotechnol.*, 7(1):206–224, 2007.

[48] J. A. Christodoulides, M. J. Bonder, Y. Huang, Y. Zhang, S. Stoyanov, G. C. Hadjipanayis, A. Simopoulos, and D. Weller. Intrinsic and hysteresis properties of FePt nanoparticles. *Phys. Rev. B*, 68:054428–1–7, 2003.

[49] Y. Tsunoda, D. Tsuchiya, and Y. Higashiyama. Crossover of spin correlations in $\mathrm{Pt}_{100-X}\mathrm{Fe}_X$ ($16 \leq x \leq 25$) alloys. *J. Phys. Soc. Japan*, 72(3): 713–717, 2003.

[50] G. E. Bacon and J. Crangle. Chemical and magnetic order in Platinum-rich Pt+Fe alloys. *Proc. R. Soc. A*, 272(1350):387–405, 1963.

[51] J. Crangle and W. R. Scott. Dilute ferromagnetic alloys. *J. Appl. Phys.*, 36(3):921–928, 1965.

[52] E. F. Wassermann. New developments on the Invar-Effect. *Phys. Scripta*, T25:209–219, 1989.

[53] L. Graf and A. Kussmann. Equilibrium diagram and magnetic properties of Pt-Fe alloys. *Physik Z.*, 36:544–551, 1935.

[54] V. L. Sedov. *Antiferromagnetism of γ-Fe, The Invar Problem.* (in Russian) Nauka, Moscow, 1987.

[55] B. Rellinghaus, S. Stappert, M. Acet, and E. F. Wassermann. Magnetic properties of FePt nanoparticles. *J. Magn. Magn. Mater.*, 266(12):142–154, 2003.

[56] Y.K. Takahashi, K. Hono, T. Shima, and K. Takanashi. Microstructure and magnetic properties of FePt thin films epitaxially grown on MgO(001) substrates. *J. Magn. Magn. Mater.*, 267(2):248–255, 2003.

[57] N. H. Luong, V. V. Hiep, D. M. Hong, N. Chau, N. D. Linh, M. Kurisu, D. T. K. Anh, and G. Nakamoto. High-coercivity FePt sputtered films. *J. Magn. Magn. Mater.*, 290-291:559–561, 2005.

[58] Ch. Kittel. *Einfühung in die Festkörperphysik*, page 43. R.Oldenbourg Verlag 8. Aufl., 1989.

[59] H. Lipson, D. Schoenburg, and G. V. Stupart. The relation between atomic arrangement and coercivity in an alloy of iron and platinum. *J. Inst. Metals*, 67:333–340, 1941.

[60] A. Menshikov, T. Tarnóczi, and E. Krén. Magnetic structure of ordered FePt and Fe_3Pt alloys. *Fiz. Met. Metalloved.*, 38:505, 1974.

[61] H. Okamoto. *Phase Diagrams of Binary Iron Alloys*, page 43. Materials Information Soc., Materials Park, Ohio, 1993.

[62] C.B. Rong, Li Y., and J. P. Liu. Curie temperatures of annealed FePt nanoparticle systems. *J. Appl. Phys.*, 101(9):09K505–09K505–3, 2007.

[63] D. Palaith, C. W. Kimball, R. S. Preston, and J. Crangle. Magnetic behavior of the Pt+Fe system near Pt_3Fe. *Phys. Rev.*, 178(2):795–799, 1969.

[64] S. Maat, O. Hellwig, G. Zeltzer, Eric E. Fullerton, G. J. Mankey, M. L. Crow, and J. L. Robertson. Antiferromagnetic structure of $FePt_3$ films studied by neutron scattering. *Phys. Rev. B*, 63(13):134426–1–7, 2001.

[65] H. M. Song, W. S. Kim, Y. B. Lee, J. H. Hong, H. G. Lee, and N. H. Hur. Chemically ordered $FePt_3$ nanoparticles synthesized by a bimetallic precursor and their magnetic transitions. *J. Mater. Chem.*, 19(22):3677, 2009.

[66] J. Crangle and J.A. Shaw. The range of stability of the superlattice Pt_3Fe. *Phil. Mag*, 7:207, 1962.

[67] J. Crangle. Some magnetic properties of platinum-rich Pt-Fe alloys. *J. Phys. Radium*, 20(2-3):435–437, 1959.

[68] S. Takahashi and Y. Umakoshi. The influence of plastic deformation on the antiferromagnetic ordering in a chemically ordered $FePt_3$ alloy. *J. Phys. F: Met. Phys.*, 18(11):L257–L261, 1988.

[69] V. G. Pynko, A. S. Komalov, and L. V. Ivaeva. Influence of atomic order on magnetic properties of Fe-Pd and Fe-Pt films. *Phys. Stat. Sol. (A)*, 63:127–129, 1981.

[70] O. A. Ivanov, L. V. Solina, V. A. Demshina, and L.M. Magat. Determination of the anisotropy constant and saturation magnetisation, and magnetic properties of powders of an iron-platinum alloy. *Fiz. metal. metalloved.*, 35:92–97, 1973.

[71] T. Shima, K. Takanashi, Y. K. Takahashi, and K. Hono. Coercivity exceeding 100 kOe in epitaxially grown FePt sputtered films. *Appl. Phys. Lett.*, 85(13):2571–2573, 2004.

[72] P.T.L. Minh, N.P. Thuy, N.D. Van, and N.T.N. Chan. Structure and magnetic properties of thin FePt alloy films. *J. Magn. Magn. Mater.*, 239 (1-3):335–337, 2002.

[73] C. H. Lai, C. H. Yang, and C. C. Chiang. Ion-irradiation-induced direct ordering of $L1_0$ FePt phase. *Appl. Phys. Lett.*, 83(22):4550–4552, 2003.

[74] M. Fallot. The alloys of iron with metals of the platinum family. *Ann. Phys.*, 10:291–332, 1938.

[75] G. Morel, G. Gavoille, M. Foos, C. Frantz, and J. Hubsch. Interpretation of the anomalous Curie constant in Fe_3Pt Invar alloys. *J. Magn. Magn. Mater.*, 15-18:1193–1194, 1980.

[76] Elena V. Shevchenko. *Monodisperse magnetic alloy nanocrystals and their superstructures.* PhD thesis, Institut für Physikalische Chemie,

Universität Hamburg, Von-Melle-Park 3, 20146 Hamburg, 2003. URL `http://ediss.sub.uni-hamburg.de/volltexte/2003/1038`.

[77] C. B. Murray, S. Sun, W. Gaschler, H. Doyle, T. A. Betley, and C. R. Kagan. Colloidal synthesis of nanocrystals and nanocrystal superlattices. *IBM J.Res. Dev.*, 45(1):47–56, 2001.

[78] M. Baumann. *Übergang von stabiler zu marginal stabiler Supraleitung im Hochtemperatursupraleiter* $YBa_2Cu_3O_{7-d}$. PhD thesis, Fachbereich Physik der Universität Hamburg, Jungiusstraße 9 , 20144 Hamburg, 1998.

[79] S. Anders, M. F. Toney, T. Thomson, J.U. Thiele, B. D. Terris, S. Sun, and C. B. Murray. X-ray studies of magnetic nanoparticle assemblies. *J. Apll. Phys.*, 93(10):7343–7345, 2003.

[80] J. Lyubina, O. Isnard, O. Gutfleisch, K. H. Müller, and L. Schultz. Ordering of nanocrystalline Fe-Pt alloys studied by in situ neutron powder diffraction. *J. Appl. Phys.*, 100(9):094308–094308–9, 2006.

[81] C. Antoniak, M. Spasova, A. Trunova, K. Fauth, F. Wilhelm, A. Rogalev, J. Minar, H. Ebert, M. Farle, and H. Wende. Inhomogeneous alloying in FePt nanoparticles as a reason for reduced magnetic moments. *J. Phys.: Condens. Matter*, 21(33):336002, 2009.

[82] W.B. Pearson. *A Handbook of Lattice Spacings and Structures in Metals and Alloys.* Oxford: Pergamon, 1958. p 634.

[83] B. Predel. *The Landolt-Börnstein database*, volume 5e of *Springer Materials*, chapter Fe-Pt: (Iron-Platinum). Springer, 1995.

[84] K. M. Hyie and I. I. Yaacob. Phase transition of iron-platinum nanoparticles prepared in water-in-oil microemulsions. *AIP Conf. Proc.*, 1136: 156–160, 2009.

[85] R. Segnan. Experimental investigation on exchange interaction in Platinum-Iron alloys. *Phys. Rev.*, 160(2):404–408, 1967.

[86] A. Z. Menshikov, Yu. A. Dorofeev, V.A. Kazanzev, and S.K. Sidorov. Influence of the pressure on the exchange interaction in disordered iron-platinum alloys. *Fiz. Met. Metalloved.*, 38:505, 1974.

[87] L. I. Vinokurova, I. N. Nikolayev, Ye. V. Mel'nikov, I. K. Adis'yevich, and Yu. B. Reutov. Antiferromagnetic transformations in Iron-Platinum alloys studied by the mossbauer effect. *Phys. Met. Metallogr.*, 28(6):1098, 1996.

[88] G. Xiao and C. L. Chien. Temperature dependence of spontaneous magnetization of ultrafine Fe particles in Fe-SiO_2 granular solids. *J. Appl. Phys.*, 61:3308, 1987.

[89] P. V. Hendriksen, S. Linderoth, and P. A Lindgard. Finite-size modifications of the magnetic properties of clusters. *Phys. Rev. B*, 48:7259–7273, 1993.

[90] M. Ulmeanu, C. Antoniak, U. Wiedwald, M. Farle, Z. Frait, and S. Sun. Composition-dependent ratio of orbital-to-spin magnetic moment in structurally disordered Fe_xPt_{1-x} nanoparticles. *Phys. Rev. B*, 69(5):054417, 2004.

[91] G.Y. Guo and H. Ebert. First-principles study of the magnetic hyperfine field in Fe and Co multilayers. *Phys. Rev. B*, 53:2492, 1996.

[92] R. Berger, J. Kliava, J.C. Bissey, and V. Baietto. Superparamagnetic resonance of annealed iron-containing borate glass. *J. Phys.: Condens. Matter*, 10:85598572, 1998.

[93] Ch. Kittel. Interpretation of anomalous larmor frequencies in ferromagnetic resonance experiment. *Phys. Rev.*, 71:270, 1947.

[94] U. Netzelmann. Ferromagnetic resonance of particulate magnetic resonance tapes. *Phys. Rev. B*, 68(4):1800–1807, 1990.

[95] R.S. de Biasi and T.C. Devezas. Anisotropy field of small magnetic particles as measured by resonance. *J. Appl. Phys.*, 49(4):2466–2469, 1978.

[96] A. Flosdorff, F. Görlitz, and J. Kötzler. Temperature and field dependence of domain wall dynamics up to the Curie point of EuO. *J. Appl. Phys.*, 79(8):6054–6056, 1996.

[97] J. Kötzler, D. Görlitz, and F. Wiekhorst. Strong spin-orbit-induced Gilbert damping and g-shift in iron-platinum nanoparticles. *Phys. Rev. B*, 76:104404–1–8, 2007.

[98] B. Heinrich. *Ultrathin Magnetic Structures III*, page 143. Springer Verlag, Berlin, Heidelberg, New York, 2005.

[99] Quantum Design. Application Notes: Reference Samples. `http://www.qdusa.com/sitedocs/appNotes/mpms/1041-001.pdf`, 2014. [Online; accessed 13-August-2014].

Chapter 7

Acknowledgements

I would like to express my sincere gratitude to the following persons:

- Prof. Dr. K. Nielsch for providing me the opportunity to finalize my work and the support and discussions during the completion of this work.
- Dr. D. Görlitz for his generous guidance, constant encouragements, endless patience and valuable support throughout the whole course of my study.
- Prof. Dr. J. Kötzler for a very interesting research topic, for providing excellent experimental facilities and for many fruitful discussions.
- Special appreciation goes to Dipl. Ing. R. Meißner for his technical and constructional support and many conducive discussions.
- I want to thank Dr. E. Shevchenko and Prof. Dr. H. Weller for preparing the Fe_xPt_{1-x} nanoparticles with these very interesting magnetic properties, together with the many useful discussions concerning the chemistry of magnetic nanoparticles.
- Another special thanks goes to Dipl.-Ing. A. Kornowski for excellent (HR)TEM images.
- I would like to take this opportunity to thank all the members of the group K for their friendship and support throughout my time at Hamburg university.

- I would like to thank all my family and personal friends for their help, understanding, support and nice company.

Appendix A

Some important magnetic units and physical constants

In table (A) important magnetic units and constants in the SI and CGS system are summarized

name	symbol	SI	CGS	conversion (SI→CGS)
magnetic moment	m	$\mathrm{A\cdot m^2}$	emu	10^3
magnetic field (strength)	H	$\frac{\mathrm{A}}{\mathrm{m}}$	Oe	$\frac{4\pi}{10^3}$
magnetic flux density	B	T	G	10^{-4}
volume magnetization	M	$\frac{\mathrm{A}}{\mathrm{m}}$	$\frac{\mathrm{emu}}{\mathrm{cm^3}}$	10^{-3}
mass magnetization	M	$\frac{\mathrm{A\cdot m^2}}{\mathrm{kg}}$	$\frac{\mathrm{emu}}{\mathrm{g}}$	1
mass susceptibility	χ	$\frac{\mathrm{m^3}}{\mathrm{kg}}$	$\frac{\mathrm{emu}}{\mathrm{g\cdot Oe}}$	$\frac{10^3}{4\pi}$
volume susceptibility	χ	-	$\frac{\mathrm{emu}}{\mathrm{cm^3 \cdot Oe}}$	$\frac{1}{4\pi}$
anisotropy constant	K	$\frac{\mathrm{J}}{\mathrm{m^3}}$	$\frac{\mathrm{erg}}{\mathrm{cm^3}}$	0.1

Table A.1: Important magnetic quantities and their conversion from SI to units. Used unit abbreviations are electromagnetic unit (emu), Tesla (T), Gauss (G), Oersted (Oe). $1\ \mathrm{J} = 10^{-7}\ \mathrm{kg\cdot m^2 \cdot\ s^2} = 10^{-7}$ erg. The magnetic moment often is expressed in units of Bohr-magneton μ_B as $1\ \mathrm{Am^2} = 1.078 \cdot 10^{23} \mu_B$ (1 emu=$1.078 \cdot 10^{20} \mu_B$).

name	symbol	value	unit
permeability of vacuum	μ_0	$4\pi \cdot 10^{-7}$	$\frac{\mathrm{V \cdot s}}{\mathrm{A \cdot m}} = \frac{\mathrm{m \cdot kg}}{\mathrm{s^2 \cdot A^2}}$
Bohr magneton	$\mu_\mathrm{B} = \frac{e\hbar}{2m_\mathrm{e}}$	9.2740110^{-24}	$\frac{\mathrm{J}}{\mathrm{T}} = \mathrm{A} \cdot \mathrm{m}^2$
Boltzmann constant	$\mathrm{k_B}$	1.380710^{-23}	$\frac{\mathrm{J}}{\mathrm{K}} = \frac{\mathrm{m^2 \cdot kg}}{\mathrm{s^2 \cdot K^2}}$
vacuum speed of light	c	299792458	$\frac{\mathrm{m}}{\mathrm{s}}$
Planck constant	$\hbar = \frac{h}{2\pi}$	$1.05459\ 10^{-34}$	J·s
electron charge	e	$1.6022\ 10^{-19}$	C
electron mass	$\mathrm{m_e}$	$9.1094\ 10^{-31}$	kg
electron magnetic moment	μ_e	$9.28477\ 10^{-24}$	$\frac{\mathrm{J}}{\mathrm{T}}$
Landé g-factor of free electron	$\mathrm{g}_e = \frac{2\mu_\mathrm{e}}{\mu_\mathrm{B}}$	2.0023193	
gyromagnetic ratio of free electron*	$\gamma_\mathrm{e} = \frac{g\mu_\mathrm{B}}{\hbar} = \frac{ge}{2m_\mathrm{e}c}$		$\frac{\mathrm{Hz}}{\mathrm{T}}$

Table A.2: Fundamental magnetic constants in SI units

$^*\gamma = \frac{\mu}{L}$, μ magnetic moment, L angular momentum

Appendix B

The log-normal distribution

Two equivalent notations of the log-normal distribution are found in literature, the widely used $P(x)$ with median $\tilde{x}$ and width σ

$$P(x) = \frac{1}{\sqrt{2\pi}\sigma x} \exp\left(-\frac{(\ln x - \ln \tilde{x})^2}{2\sigma^2}\right) = \frac{1}{\sqrt{2\pi}\sigma x} \exp\left(-\frac{(\ln \frac{x}{\tilde{x}})^2}{2\sigma^2}\right) \tag{B.1}$$

and a notation $P(y)$ with reduced argument $y \equiv x/\tilde{x}$

$$P(y) = \frac{1}{\sqrt{2\pi}\sigma y} \exp\left(-\frac{\ln^2 y}{2\sigma^2}\right) \tag{B.2}$$

Both distributions are normalized to unity $\int_0^\infty P(x)\mathrm{d}x = \int_0^\infty P(y)\mathrm{d}y \equiv 1$. And the corresponding mean values are given by (assuming $\sigma > 0$)

$$\bar{x} = \int_0^\infty xP(x)\mathrm{d}x = \tilde{x}\exp(\sigma^2/2) \tag{B.3}$$

and

$$\bar{y} = \int_0^\infty yP(y)\mathrm{d}y = \exp(\sigma^2/2) \tag{B.4}$$

Equation (B.2) transforms into the first one eq.(B.1) by substitution $y \equiv x/\tilde{x}$ and rescaling of y-axis $y \to y \cdot \tilde{x}$ and amplitude $P(y) \to P(y)/\tilde{x}$, so that both distributions coincide. When using eq.(B.2) to describe a magnetization curve, the equivalent to eq.(2.36) reads as

$$M(H,T) = N_\mathrm{p}\tilde{\mu} \int_0^\infty y\, P(y) \left(\coth\left(\frac{y\tilde{\mu}\,\mu_0 H}{\mathrm{k_B}T}\right) - \frac{\mathrm{k_B}T}{y\tilde{\mu}\,\mu_0 H}\right) \mathrm{d}y + \chi_\mathrm{bgd} H \tag{B.5}$$

B.1 Relation between mean, median and maximum of the log-normal distribution

Besides the median x_{md} as a basic parameter to characterize a log-normal distribution $P(x)$ eq.(B.1) often the mean x_0 or the maximum $x_{\max}$ are stated which are related to each other by

$$x_{\max} = x_{\mathrm{md}} \exp(-\sigma^2) \tag{B.6}$$
$$x_0 = x_{\mathrm{md}} \exp(\sigma^2/2) = x_{\max} \exp(3\sigma^2/2) \tag{B.7}$$

As shown in fig. B.1 for $\sigma \to 0$ the three parameter coincide, while for $\sigma > 0$ the mean value lies above and the maximum below the median value.

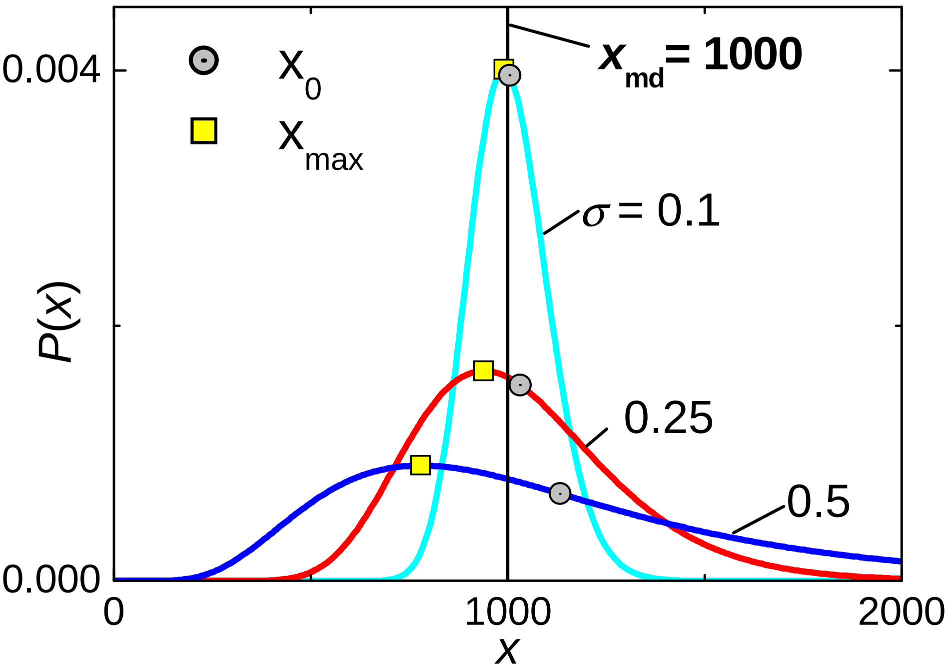

Figure B.1: Log-normal distributions with median $x_{\mathrm{md}} = 1000$ and increasing widths $\sigma = 0.1, 0.25, 0.5$. The squares mark the corresponding maxima, the circles the corresponding mean values.

B.2 Relations between diameter and volume log-normal distribution

We define the log-normal distribution of diameters $P(D)$ with median diameter $\tilde{D}$ and width σ according to eq. B.1

$$P(D) = \frac{1}{\sqrt{2\pi}\sigma_D D} \exp\left(-\frac{(\ln D - \ln \tilde{D})^2}{2\sigma_D^2}\right) \tag{B.8}$$

and accordingly the log-normal distribution of volumes $P(V)$ with median volume $\tilde{V}$ and width σ_V

$$P(V) = \frac{1}{\sqrt{2\pi}\sigma_V V} \exp\left(-\frac{(\ln V - \ln \tilde{V})^2}{2\sigma_V^2}\right) \tag{B.9}$$

Then the mean diameter $\bar{D}$ is given by

$$\bar{D} = \int_0^\infty D P(D) \mathrm{d}D = \tilde{D} \exp\left(\frac{\sigma_D^2}{2}\right) \tag{B.10}$$

And the mean volume $\bar{V}$is defined in the same way

$$\bar{V} = \int_0^\infty V P(V) \mathrm{d}V = \tilde{V} \exp\left(\frac{\sigma_V^2}{2}\right) \tag{B.11}$$

The mean volume can also be calculated using the diameter log-normal distribution as

$$\begin{aligned} \bar{V} &= \int_0^\infty \frac{\pi D^3}{6} P(D) \mathrm{d}D = \frac{\pi \tilde{D}^3}{6} \exp\left(\frac{9\sigma_D^2}{2}\right) && \text{(B.12)} \\ &= \frac{\pi}{6}\left(\tilde{D} \exp\left(\frac{\sigma_D^2}{2}\right)\right)^3 \exp(3\sigma_D^2) \\ &= \frac{\pi}{6} \bar{D}^3 \exp(3\sigma_D^2) && \text{(B.13)} \end{aligned}$$

where relation eq. B.10 between mean and median has been used. Comparing right-hand side of eq. B.12 with B.11 we see that formally $\tilde{V} = \pi\tilde{D}^3/6$ and $\sigma_V = 3\sigma_D$. In other words, the median values are directly related, while the mean values are influenced by the distribution width.

B.3 Logarithmic sampling

For the modelling of log-normal distribution the logarithmically sampling of an interval $[x_\mathrm{b}, ..., x_\mathrm{e}]$ by N sampling points is often usedful. This can be achieved by

$$x_{\log}(i) = x_\mathrm{b}^{\frac{N-i}{N-1}} x_\mathrm{e}^{\frac{i-1}{N-1}}, \quad i = 1, ..., N \tag{B.14}$$

Appendix C

Relation between atomic and weight percentages in binary alloys

In literature both, atomic percentage at% and weight percentage wt% are denoted for description of the composition of binary alloys. The conversion between atomic percentage at% and weight percentage wt% of a component in a binary system A-B is given by

$$\text{wt\% A} = \frac{\text{at\% A} \cdot m_a(\text{A})}{(\text{at\% A} \cdot m_a(\text{A})) + (\text{at\% B} \cdot m_a(\text{B}))} \cdot 100 \tag{C.1}$$

and

$$\text{at\% A} = \frac{\text{wt\% A}/m_a(\text{A})}{(\text{wt\% A}/m_a(\text{A})) + (\text{wt\% B}/m_a(\text{B}))} \cdot 100 \tag{C.2}$$

where $\mathrm{m}_a(\mathrm{X})$ is the atomic mass of component X.

Appendix D

Experimental details

D.1 Field calibration of the SQUID magnetometer

Moving a sample stepwise through the pick-up coil, a voltage proportional to the magnetic field created by the sample's magnetic moment is induced and detected as SQUID response $h(z)$ (inset of Fig. D.1). By fitting to the data the response curve (idealized point dipole moving through a 2nd order gradiometer with radius $R = 1$ cm and distance $A = 1.5$ cm between the coils)

$$\begin{aligned} h(z) &= A_0 + A_1 \left[\frac{R}{(R^2 + ((z - z_0) - A)^2)^{3/2}} - \frac{2R}{((R^2 + (z - z_0)^2)^{3/2}} \right. \\ &+ \left. \frac{R}{(R^2 + ((z - z_0) + A)^2)^{3/2}} \right], \end{aligned} \tag{D.1}$$

the amplitude A_1 is determined. By means of a cylindric Palladium reference sample ($m = 0.2756$ g) the amplitude A_1 is calibrated to obtain an absolute magnetic moment. At regular intervals the moment calibration of the device was verified by comparison of the paramagnetic susceptibility of the reference sample measured at T=300 K with the nominal susceptibility of $5.23 \cdot 10^{-6}$ Am^2/kg [99], as shown in Fig. D.1.

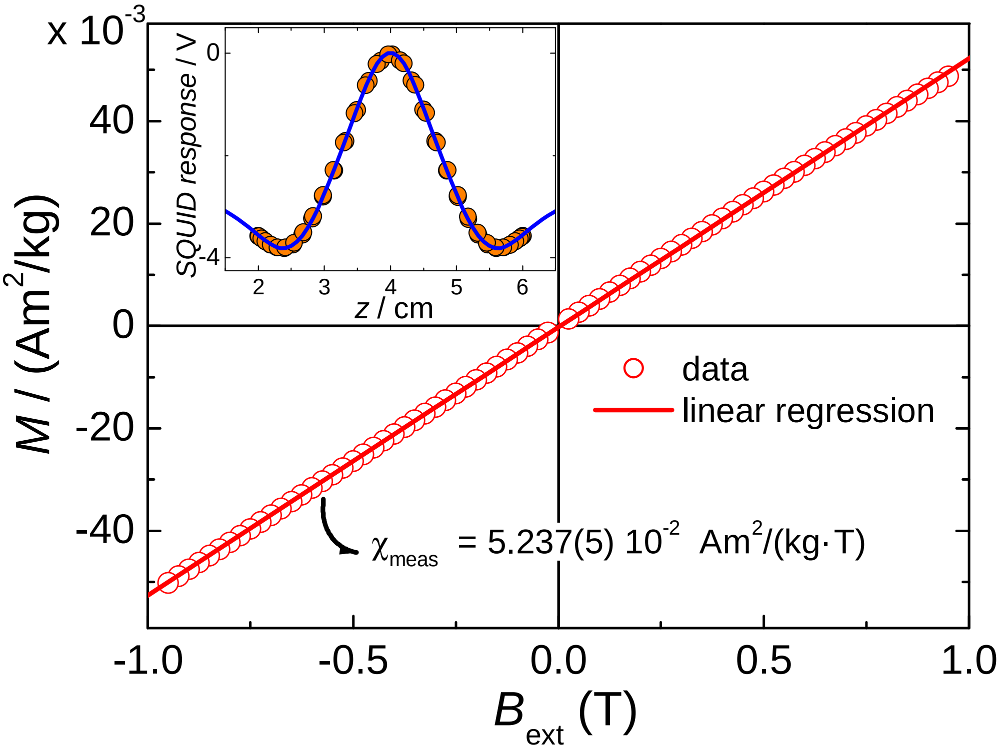

Figure D.1: Magnetic moment calibration check of the SQUID-magnetometer by a field sweep at $T = 300$ K of the Pd reference cylinder (m=0.2756 g). The determined susceptibility $\chi_{\mathrm{meas}} = 5.237(5) \cdot 10^{-2}$ Am^2/(kg·T) nicely matches the nominal value $\chi_{\mathrm{nom}} = 5.23 \cdot 10^{-6}$ Am^2/(kg·T). The inset shows a single SQUID response curve of the reference sample measured at $B = 1$ T, together with the fitted model curve Eq. D.1.

Publications

with the subject area $\mathbf{Fe}_x\mathbf{Pt}_{1-x}$ –nanoparticles

E. Shevchenko, D. Talapin, A. Kornowski, F. Wiekhorst, J. Kötzler, M. Haase, A. Rogach, H. Weller. Colloidal crystals of monodisperse FePt nanoparticles grown by a three-layer technique of controlled oversaturation. *Adv. Mater.* 14:287-290, 2002.

F. Wiekhorst, E. Shevchenko, H. Weller, J. Kötzler. Anisotropic superparamagnetism of monodispersive cobalt-platinum nanocrystals. *Phys. Rev. B* 67:224416-1-11, 2003.

F. Wiekhorst, E. Shevchenko, H. Weller, J. Kötzler. Temperature-dependent anisotropy effects on FMR and magnetization of $FePt_2$ and $CoPt_3$ nanocrystals. *J. Magn. Magn. Mater.* 272-276:1559-1560, 2004.

J. Kötzler, D. Görlitz, F. Wiekhorst. Strong spin-orbit-induced Gilbert damping and g-shift in iron-platinum nanoparticles. *Phys. Rev. B* 76:104404-1-8, 2007.

further relevant publications

2014

M. Liebl, F. Wiekhorst, U. Steinhoff, J. Haueisen, L. Trahms. Quantitative imaging of magnetic nanoparticles by magnetorelaxometry with multiple excitation coils. *Phys. Med. Biol.* 59(21):6607-6620, 2014.

J. Nowak, F. Wiekhorst, L. Trahms, S. Odenbach. The influence of hydrodynamic diameter and core composition on the magnetoviscous effect of biocompatible ferrofluids, *J. Phys. Cond. Matter* 26(17):176004, 2014.

A. Coene, G. Crevecoeur, M. Liebl, F. Wiekhorst, L. Dupré, U. Steinhoff. Uncertainty of reconstructions of spatially distributed magnetic nanoparticles under realistic noise conditions, *J. Appl. Phys.* 115:17BN509, 2014.

2013

C. Harms, A. L. Datwyler, F. Wiekhorst, L. Trahms, R. Lindquist, E. Schellenberger, S. Müller, G. Schütz, F. Roohi, A. Ide, M. Füchtemeier, K. Gertz, G. Kronenberg, U. Harms, M. Endres, U. Dirnagl, T. D. Farr. Certain types of iron oxide nanoparticles are not suited to passively target inflammatory cells that infiltrate the brain in response to stroke. *JCBFM* 33(5):e1-e9, 2013.

R. Tietze, S. Lyer, S. Dürr, T. Struffert, T. Engelhorn, M. Schwarz, E. Eckert, T. Göen, S. Vasylyev, W. Peukert, F. Wiekhorst, L. Trahms, A. Dörfler, C. Alexiou. Efficient drug-delivery using magnetic nanoparticles - biodistribution and therapeutic effects in tumour bearing rabbits. *Nanomedicine* 9(7):961-971, 2013.

Ch. Knopke, F. Wiekhorst, D. Eberbeck, I. Gemeinhardt, M. Ebert, J. Schnorr, S. Wagner, M. Taupitz, L. Trahms. Quantification of magnetic nanoparticle uptake in cells by temperature dependent magnetorelaxometry. *IEEE Trans. Mag.* 49:421-424, 2013.

N. Löwa, F. Wiekhorst, I. Gemeinhardt, M. Ebert, J. Schnorr, S. Wagner, M. Taupitz, L. Trahms. Cellular uptake of magnetic nanoparticles quantified by magnetic particle spectroscopy. *IEEE Trans. Mag.* 49:275-278, 2013.

F. Wiekhorst, U. Steinhoff, M. Bär, L. Trahms, W. Haberkorn. Quantification and localization of extended nanoparticle distributions in tissue using multipole expansion. *Biomed. Tech.* 58:1-2 dx.doi.org/10.1515/bmt-2013-4345, 2013.

2012

F. Wiekhorst, U. Steinhoff, D. Eberbeck, L. Trahms. Magnetorelaxometry assisting biomedical applications of magnetic nanoparticles. P*harmaceut. Res.* 29(5):1189-1202, 2012.

R. Eichardt, D. Baumgarten, B. Petkovic, F. Wiekhorst, L. Trahms, J. Haueisen. Adapting source grid parameters to improve the condition of the magnetostatic linear inverse problem of estimating nanoparticle distributions. *MBEC* 50(10): 1081-1089, 2012.

G. Hasenpusch, J. Geiger, K. Wagner, O. Mykhaylyk, F. Wiekhorst, L. Trahms, A. Heidsieck, B. Gleich, C. Bergemann, M. K. Aneja, C. Rudolph.

Magnetized aerosols comprising superparamagnetic iron oxide nanoparticles improve targeted drug and gene delivery to the lung. *Pharmaceut. Res.* 29(5):1308-1318, 2012.

F. Wiekhorst, M. Liebl, U. Steinhoff, L. Trahms, S. Lyer, S. Dürr, C. Alexiou. Magnetorelaxometry for in-vivo quantification of magnetic nanoparticle distributions after magnetic drug targeting in a rabbit carcinoma model. *Proc. in Phys.* 140:301-305, 2012.

F. Wiekhorst, W. Haberkorn, U. Steinhoff, S. Lyer, C. Alexiou, M. Bär, L. Trahms. Principal moments of a multipole expansion to quantify the magnetic nanoparticle distributions in arteries. *Biomed. Tech.* 57(1):751-754, 2012.

Ch. Knopke, F. Wiekhorst, I. Gemeinhardt, M. Ebert, J. Schnorr, M. Taupitz, L. Trahms. Quantification of small magnetic nanoparticle characteristics by temperature dependent magnetorelaxometry. *Biomed. Tech.* 57(1):84, 2012.

N. Löwa, D. Eberbeck, U. Steinhoff, F. Wiekhorst, L. Trahms. Potential of improving MPI performance by magnetic separation. *Proc. in Phys.* 140:73-78, 2012.

U. Steinhoff, M. Liebl, M. Bauer, F. Wiekhorst, L. Trahms, D. Baumgarten, J. Haueisen. Spatially resolved measurement of Magnetic Nanoparticles using inhomogeneous excitation fields in the linear susceptibility range (<1 mT). *Proc. in Phys.* 140:295-300, 2012.

2011

M. Kettering, H. Richter, F. Wiekhorst, S. Bremer-Streck, L. Trahms, W. A. Kaiser, I. Hilger. Minimal-invasive magnetic heating of tumors does not alter intra-tumoral nanoparticle accumulation, allowing for repeated therapy sessions: an in vivo study in mice. *Nanotechnology* 22(50):7, 2011.

F. Wiekhorst, I. Gemeinhardt, J. Schnorr, M. Taupitz, L. Trahms. Cellular uptake of magnetic nanoparticles quantified by non-linear AC susceptometry. *Biomed. Tech.* ISSN 0939-4990, 2011.

D. Eberbeck, F. Wiekhorst, S. Wagner, L. Trahms. How the size distribution of magnetic nanoparticles determines their magnetic particle imaging performance. *Appl. Phys. Lett.* 98(18):182502-1-182502-2, 2011.

F. Wiekhorst, U. Steinhoff, M. Liebl, P. Zirpel, K. Schwarz, S. Lyer, C.

Alexiou, L. Trahms. In-vivo determination of magnetic nanoparticle content after magnetic drug targeting. *Biomed. Tech.* ISSN 0939-4990, 2011.

F. Wiekhorst, D. Baumgarten, W. Haberkorn, U. Steinhoff, J. Haueisen, M. Bär, L. Trahms. Reconstruction of magnetic nanoparticle distributions in organs by magnetic multipole expansion. *Biomed. Tech.* ISSN 0939-4990, 2011.

2010

S. Knappe, T. Sander-Thömmes, O. Kosch, F. Wiekhorst, J. Kitching, L. Trahms. Cross-validation of microfabricated atomic magnetometers with superconducting quantum interference devices for biomagnetic applications. *Appl. Phys. Lett.* 97(13):133703-1-133703, 2010.

F. Wiekhorst, D. Baumgarten, W. Haberkorn, U. Steinhoff, J. Haueisen, M. Bär, L. Trahms. Quantitative imaging of magnetic nanoparticle distributions in organs by a combined multipole-multiple dipoles approach. *Front. Neurosci. Biomag* 2010 doi: 10.3389/conf.fnins.2010.06.00388, 2010.

D. Eberbeck, F. Wiekhorst, L. Trahms. Evidence of aggregates of magnetic nanoparticles in suspensions which determine the magnetisation behavior, Magnetic Nanoparticles: Particle Science, Imaging Technology, and Clinical Applications *Proc. IWMPI* 66-72, 2010.

H. Rahn, S. Lyer, R. Tietze, H. Richter, C. Alexiou, D. Eberbeck, F. Wiekhorst, L. Trahms, F. Beckmann, S. Odenbach. SRμCT and MRX analyses of ferrofluid accumulation in bovine arteries: A step further in the understanding of Magnetic Drug Targeting. *Physics Procedia* 9:258-261, 2010.

H. Richter, M. Kettering, F. Wiekhorst, U. Steinhoff, I. Hilger, L. Trahms. Magnetorelaxometry for localization and quantification of magnetic nanoparticles for thermal ablation studies. *Phys. Med. Biol.* 55(3):623-633, 2010.

2009

D. Eberbeck, F. Wiekhorst, U. Steinhoff, L. Trahms. Quantification of biomolecule agglutination by magnetorelaxometry. *Appl. Phys. Lett.* 95(21): 213701-1-3, 2009.

H. Richter, F. Wiekhorst, K. Schwarz, S. Lyer, R. Tietze, C. Alexiou, L. Trahms. Magnetorelaxometric quantification of magnetic nanoparticles in an artery model after ex vivo magnetic drug targeting. *Phys. Med. Biol.*

54(18):N417-424, 2009.

F. Wiekhorst, U. Steinhoff, W. Haberkorn, G. Lindner, M. Bär, L. Trahms. Localization of a magnetic nanoparticle spot from features of the magnetic field pattern and comparison to a magnetic dipole fit. *IFMBE proceedings* 22(7):2347-2351, 2009.

F. Wiekhorst, D. Baumgarten, W. Haberkorn, U. Steinhoff, J. Haueisen, M. Bär, L. Trahms. A physical phantom modeling extended magnetic nanoparticle distributions in biological systems. *IFMBE proceedings* 25(7):293-296, 2009.

D. Eberbeck, F. Wiekhorst, U. Steinhoff, K. O. Schwarz, A. Kummrow, M. Kammel, J. Neukammer, L. Trahms. Specific binding of magnetic nanoparticle probes to platelets in whole blood detected by magnetorelaxometry. *J. Magn. Magn. Mater.* 321(10):1617-1620, 2009.

C. Seliger, R. Jurgons, F. Wiekhorst, D. Eberbeck, L. Trahms, H. Iro, C. Alexiou. In vitro investigation of the behaviour of magnetic particles by a circulating artery model. *J. Magn. Magn. Mater.* 311(1):358-362, 2009.

R. Tietze, R. Jurgons, S. Lyer, E. Schreiber, F. Wiekhorst, D. Eberbeck, H. Richter, U. Steinhoff, L. Trahms, C. Alexiou. Quantification of drug-loaded magnetic nanoparticles in rabbit liver and tumor after in vivo administration. *J. Magn. Magn. Mater.* 321(10):1465-1468, 2009.

2008

F. Wiekhorst, U. Steinhoff, D. Eberbeck, K. Schwarz, H. Richter, R. Renner, M. Roessner, C. Rudolph, L. Trahms. Quantification of magnetic nanoparticle concentration in pig lung tissue after magnetic aerosol drug targeting by magnetorelaxometry. *IFMBE Proceedings* 22:2326-2329, 2008.

F. Wiekhorst, U. Steinhoff, W. Haberkorn, G. Lindner, M. Bär, L. Trahms. Localization of a magnetic nanoparticle spot from features of the magnetic field pattern and comparison to a magnetic dipole fit. *IFMBE Proceedings* 22:2347-2351, 2008.

D. Eberbeck, A. P. Astalan, K. Petersson, F. Wiekhorst, C. Bergemann, C. Johansson, U. Steinhoff, H. Richter, A. Krozer, L. Trahms. AC susceptometry and magnetorelaxometry for magnetic nanoparticle based biomolecule detection. *IFMBE Proceedings* 22:2317-2321, 2008.

D. Baumgarten, M. Liehr, F. Wiekhorst, U. Steinhoff, P. Münster, P. Miethe, L. Trahms, J. Haueisen. Magnetic nanoparticle imaging by means of minimum norm estimates from remanence measurements. *Med. Biol. Eng. Comput.* 46:1177-1185, 2008.

D. Eberbeck, C. Bergemann, F. Wiekhorst, U. Steinhoff, L. Trahms. Quantification of specific bindings of biomolecules by magnetorelaxometry. *J. Nanobiotech.* 6:4:1-12, 2008.

2007

F. Wiekhorst, D. Eberbeck, U. Steinhoff, D. Gutkelch, L. Trahms. Schlussbericht zum Teilvorhaben "SQUID-basierte Magnetrelaxometrie an magnetischen Nanopartikeln für die medizinische Diagnostik" (FKZ 13N8535) im BMBF-Verbundvorhaben "Nanomagnetomedizin", 62 Seiten, URL: edok01.tib.uni-hannover.de/edoks/e01fb08/576714585.pdf, 2007.

F. Wiekhorst, U. Steinhoff, D. Eberbeck, R. Jurgons, C. Seliger, C. Alexiou, L. Trahms. Magnetorelaxometric quantification of nanoparticle content in biological tissue using a multichannel vector magnetometer. *Biomed. Tech.* 52:1569047463.pdf, 2007.

F. Wiekhorst, U. Steinhoff, R. Fischer, D. Gutkelch, F. Ruede, R. Ackermann, M. Bader, Th. Schurig, L. Trahms , H. Koch. Characterization of a standalone SQUID-system with integrated superconducting shield for magnetocardiography of mice. *Biomed. Tech.* 52:1569047617.pdf, 2007.

P. Dames, B. Gleich, A. Flemmer, K. Hajek, N. Seidl, F. Wiekhorst, D. Eberbeck, I. Bittmann, Ch. Bergemann, Th. Weyh, L. Trahms, J. Rosenecker, C. Rudolph. Targeted delivery of magnetic aerosol droplets to the lung. *Nature Nanotech.* 2:495 - 499, 2007.

C. Seliger, R. Jurgons, F. Wiekhorst, D. Eberbeck, L. Trahms, H. Iro, C. Alexiou. In vitro investigation of the behaviour of magnetic particles by a circulating artery model. *J. Magn. Magn. Mater.* 311:358 - 362, 2007.

R. Ackermann, F. Wiekhorst, A. Beck, D. Gutkelch, F. Ruede, A. Schnabel, U. Steinhoff, D. Drung, J. Beyer, C. Aßmann, L. Trahms, H. Koch, Th. Schurig, R. Fischer, M. Bader, H. Ogata, H. Kado. Multichannel SQUID system with integrated magnetic shielding for magnetocardiography of mice. *IEEE Trans. Appl. Supercond.* 17:827-830, 2007.

2006

F. Wiekhorst, D. Eberbeck, U. Steinhoff, R. Jurgons, C. Seliger, C. Alexiou, L. Trahms. Quantification of magnetic nanoparticles in tissue demonstrated by magnetorelaxometry tomography. *Biomed. Tech.* 2006.

F. Wiekhorst, C. Seliger, R. Jurgons, U. Steinhoff, D. Eberbeck, L. Trahms, C. Alexiou. Quantification of magnetic nanoparticles by magnetorelaxometry and comparison to histology after magnetic drug targeting. *J. Nanosci. Nanotech.* 6:3222-3225, 2006.

D. Eberbeck, F. Wiekhorst, U. Steinhoff, L. Trahms. Aggregation behaviour of magnetic nanoparticle suspensions investigated by magnetorelaxometry. *J. Phys.: Condens. Matter* 18:S2829-2846, 2006.

F. Wiekhorst, D. Eberbeck, U. Steinhoff, R. Jurgons, C. Seliger, C. Alexiou, L. Trahms. Quantification of magnetic nanoparticles in tissue demonstrated by magnetorelaxometry tomography. *Rec. Dev. in Ferrofluid Res.*, EUROMECH 470, 2006

2005

D. Eberbeck, Ch. Bergemann, F. Wiekhorst, G. Glöckl. Quantification of aggregates of magnetic nanoparticles in different suspension media by magnetorelaxometry. *Magnetohydrodynamics* 41:305-316, 2005.

U. Steinhoff, A. Link, F. Wiekhorst, M. Bader, S. Knappe-Grüneberg, R. Ackermann. Complex narrow band-pass filters for QRS detection in contactless magnetocardiograms of small animals. *Comput. in Cardiology* 32:467-470, 2005.

U. Steinhoff, C. Wilhelm, F. Wiekhorst, S. Y. Lee, R. Ackermann, M. Bader, Th. Schurig. Contactless magnetocardiographic characterization of knock-out mice. *Folia Cardiologica* 12D:396-398, 2005.

F. Wiekhorst, R. Jurgons, D. Eberbeck, T. Sander, U. Steinhoff, S. Hartwig, C. Alexiou, L. Trahms. SQUID system with integrated superconducting shield for monitoring of drug targeting with magnetic nanoparticles in animals. *Biomed. Tech.* 50(1):609-610, 2005.

S. Bauer, R. Weber dos Santos, U. Steinhoff, F. Wiekhorst, R. Ackermann, Th. Schurig, L. Trahms, M. Bär, H. Koch. Bidomain modelling of electrical activity of the mouse heart supports the design of a specialized magnetocardiographic device. *Biomed. Tech.* 50(1):171-172, 2005.

<2005

F. Wiekhorst. Konzeption der technischen und organisatorischen Grundlagen der Sicherheits- und Authentifizierungsmodule für eine verteilt betriebene Qualitätskontrolle, interner Bericht, Hamburg, 2002.

F. Wiekhorst, J. Kötzler, V. V. Matveev, I. V. Pleshakov, V. I. Chizhik. NMR in nanocomposites of cobalt in SiO_2 matrices Trends in Magnetism - EASTMAG, St. Petersburg, Russland, 2001.

M. W. Pieper, F. Wiekhorst, T. Wolf. Characterization of localized hole states in $Pr_{1+x}Ba_{2-x}Cu_3O_{6+y}$ by nuclear magnetic resonance. *Phys. Rev. B* 62: 1392-1407, 2000.

M. W. Pieper, K. Nehrke, F. Wiekhorst, T. Wolf. The Magnetic State of Cu in the CuO_2-Bilayers of $PrBa_2Cu_3O_{6+x}$: An NMR investigation. *J. Low. Temp. Phys.* 105:431-436, 1996.

patents:

D. Eberbeck, U. Steinhoff, F. Wiekhorst. Verfahren zum quantitativen Nachweis von Analyten in flüssigem Medium, Patent:10 2008 013 997.1, 2008.